The Effects of Three-Dimensional Shaping with Applied Magnetic Perturbations on Pedestal Stability

By

Tyler Brett Cote

A dissertation submitted in partial fulfillment of

the requirements for the degree of

Doctor of Philosophy

(Nuclear Engineering and Engineering Physics)

at the

UNIVERSITY OF WISCONSIN-MADISON

2020

Date of final oral examination: 12/16/2020

The dissertation is approved by the following members of the Final Oral Committee:

Chris C. Hegna, Professor, Nuclear Engineering and Engineering Physics
Carl R. Sovinec, Professor, Nuclear Engineering and Engineering Physics
Oliver Schmitz, Professor, Nuclear Engineering and Engineering Physics
Paul W. Terry, Professor, Physics
John S. Sarff, Professor, Physics

Abstract

Recent experimental observations have found toroidally localized MHD instabilities in the plasma edge during operation with applied magnetic perturbations on ASDEX Upgrade in H-mode with low collisionality. Large edge plasma displacements are induced by a stable kink response to the 3D magnetic perturbations. This kink response results in localized changes of geometric quantities, which in turn leads to the localization of MHD instabilities in the plasma edge. Infinite-n ideal MHD ballooning theory is shown to predict the existence of these instabilities, as well as the observed toroidal localization. Utilizing 3D VMEC equilibria, the local geometric parameters determining ideal stability, include the local magnetic shear, normal curvature, and geodesic curvature, are calculated for experimentally relevant conditions. It is found that these shaping parameters have significant levels of 3D variation, with the local magnetic shear being the dominant factor behind changes in the local geometry. This behavior leads to a significant decrease in the stabilizing line-bending energy for certain field lines, resulting in the localization of the ballooning instability. Furthermore, it is observed that a finite amount of magnetic perturbation (and subsequent edge perturbation) is necessary to modify the local geometry and excite the localized instability, leading to a threshold behavior.

Additional experimental evidence suggests that this mechanism for destabilizing localized ballooning modes may have consequences for ELM stability during applied magnetic perturbations. The new PB3D code provides a framework for studying peeling-ballooning instabilities utilizing 3D VMEC equilibria, but still requires significant testing and development. Axisymmetric benchmark exercises show PB3D fails to replicate the results of other MHD codes for experimentally relevant 2D equilibria. Errors in the current-peeling response implementation are identified as a possible source of these discrepancies, which future work will look to correct.

Acknowledgements

This dissertation is the culmination of over 8 years of work involving a number of people from all around the world. It has been an honor and a privilege to work with the caliber of scientists and researchers that I have throughout this project. First and foremost, I would like to thank my thesis advisor Chris Hegna for all of the support and guidance he has given me over the years. My success in graduate school would not have been possible without his flexibility and dedication as my advisor.

Of all the people who contributed to this work over the years, none had a larger impact on this research and on me than Matthias Willensdorfer and Toon Weyens. Matthias consistently helped me with everything related to the experimental side of this work, including me in experimental design and operations, teaching me about different diagnostics, and constantly encouraging and supporting me. Toon has spent countless hours working during his free time to help with PB3D code development, testing, and bug fixing. I would like to wholeheartedly thank them for all the work that they have done and the invaluable friendships that we have built.

Finally, I would like to thank my family and friends for all of their support over the years. From my office mates in ERB510 to my various housemates over the years, whether it was Thursday night wings at Jordan's or late-night study sessions, you all are what made my time in Wisconsin memorable. You are all truly wonderful people and incredible friends.

Contents

List of Figures

List of Tables

Chapter 1

Introduction

1.1 Problem Overview

Avoidance, mitigation, or complete suppression of edge localized modes (ELMs) is paramount to the success of future fusion devices in which harmful transient heat loads to the plasma-facing materials must be avoided. One prominent method for achieving ELM mitigation [1] or suppression [2, 3] in tokamaks is the application of non-axisymmetric magnetic perturbations (MPs). However, the exact role of these magnetic perturbations in ELM control is not fully understood, and identification of the underlying physical mechanisms is an active area of research.

There are several open theories describing how the magnetic perturbations might affect the edge plasma stability and transport and the role they play in ELM mitigation and suppression. For ELM mitigation, possible mechanisms for transport and stability changes include deformation of the plasma shape and ballooning stability[4]; change in the edge rotation shear, which can affect peeling-ballooning stability[5]; toroidal periodicity, which can result in 3D localization of ballooning modes[6]; and the formation of lobe structures at the X-point enhancing the effects of the bad curvature region[7]. Similarly, leading theories for ELM suppression include magnetic island formation and overlap at the pedestal top restrict its height[8]; stochastic fields produced near the X-point lead to higher edge transport[9];

plasma response to the 3D fields that changes the stability and transport properties[6]; and magnetic flutter driven transport near rational surfaces[10]. A combination of these mechanisms — or new mechanisms not yet discovered — may be necessary to completely describe the ELM control schemes.

This thesis primarily concerns itself with the effects of the 3D magnetic geometry created by the plasma response to the MPs and subsequent changes in plasma stability. Studies at ASDEX Upgrade [11, 12], MAST [11], and DIII-D [13] have shown that ELM suppression and mitigation are optimized when the poloidal mode spectrum of the externally applied MPs excite stable kink modes at the edge which are strongly amplified by the plasma response [5]. This stable kink response causes 3D displacement of the plasma boundary and associated 3D deformations of the flux surfaces in the pedestal region, which evidence suggests can play a key role in edge turbulent transport [6] and ELM stability [7, 14].

Furthermore, recent experiments at ASDEX-Upgrade found the stable ideal kink mode dominates the edge plasma response for ELM mitigated discharges with low collisionality ($\nu^* < 0.4$) [15, 16]. Novel experimental diagnostic techniques were utilized to create a more complete 3D characterization of these plasma discharges than typically achieved, resulting in the observation of an unexpected toroidally localized instability prior to the ELM crashes[4, 16]. However, the mechanism behind the 3D localization of the MHD instabilities is not understood. Investigations into this mechanism may provide insight into the role of the 3D geometry in ELM control.

1.2 Research Goals and Approach

The overarching goal for this thesis is to better understand the effects of the magnetic perturbation induced 3D geometry on the stability of the plasma pedestal. The ASDEX Upgrade experimental results discussed in the previous section provide a solid launching point for

this investigation. Developing a better understanding of the experimentally observed localized instabilities will provide valuable insight into the interplay between the 3D magnetic geometry and plasma stability.

Based on this, the primary goals of this thesis are as follows:

1. Characterize the localized MHD instabilities observed on ASDEX Upgrade.
2. Identify the physical mechanism behind the localization of these instabilities.
3. Evaluate the role this mechanism plays (if any) in ELM mitigation and suppression.

In order to complete these goals, work was done in collaboration with the AUG team. Ongoing experimental work will be performed by ASDEX team members, complimented by a theory and computational driven approach of this thesis. Specifically, this thesis will make use of ideal MHD theory — particularly infinite-n ballooning theory — to study the stability of 3D tokamak discharges, develop and utilize numerical tools necessary for studying the effects of the 3D geometry on plasma stability, and compare the theory and computational results with relevant experimental observations.

Furthermore, it is desirable to investigate if the physical mechanisms developed for these localized instabilities apply more generally to peeling-ballooning modes and ELMs. In order to properly study this, a new numerical analysis tool — PB3D — is currently being developed. The final aspects of this thesis are concerned with the development and testing of this new code.

1.3 Document Layout

The remainder of this work focuses on addressing the role of 3D magnetic geometry on plasma stability, and is organized as follows. The first half of the thesis covers the necessary background material for this project. Chapter 2 provides an in depth overview of relevant fusion concepts, particularly focusing on ELMs and ELM control. This will serve as a more

general background and motivation to the work in this thesis. Chapters 3 and 4 concern the necessary theory and computational tools used in this thesis, respectively. The theory discussion focuses primarily on the ideal MHD model, with discussions of both the infinite-n ballooning theory and linear peeling-ballooning theory utilized in this work. A number of numerical tools are also discussed. These include the PyBalloon code, which was developed as a part of this thesis, as well as an introduction into the ongoing development of the PB3D code.

Chapter 5 addresses the majority of the work performed for this thesis, focusing on the theory and computational analysis of the helically localized ballooning instabilities observed in the ASDEX Upgrade experiments. This includes a review of the experimental procedure and results during which the modes were first observed. After that, section 5.2 presents the results of the ballooning analysis using the PyBalloon code, and proposes a mechanism for the localized destabilization of ballooning modes in the presence of 3D magnetic perturbations. Chapter 6 addresses efforts to further develop and evaluate the new PB3D code. This thesis primarily concerns the implementation of the vacuum perturbation boundary condition necessary for studying peeling instabilities, as well as initial benchmarking of the updated PB3D code against other codes for both simplistic and experimentally relevant equilibria. Finally, chapter 7 provides a summary of the work.

References

[1]Y. Liang et al., "Active control of type-I edge-localized modes with n=1 perturbation fields in the JET tokamak", Phys. Rev. Lett. **98**, 10.1103/PhysRevLett.98.265004 (2007).

[2]T. E. Evans et al., "Suppression of Large Edge-Localized Modes in High-Confinement", Phys. Rev. Lett. **92**, 235003 (2004).

[3]T. E. Evans et al., "Edge stability and transport control with resonant magnetic perturbations in collisionless tokamak plasmas", Nat. Phys. **2**, 419–423 (2006).

[4]M. Willensdorfer et al., "Field-Line Localized Destabilization of Ballooning Modes in Three-Dimensional Tokamaks", Phys. Rev. Lett. **119**, 10.1103/PhysRevLett.119.085002 (2017).

[5]Y. Liu, A. Kirk, Y. Gribov, M. P. Gryaznevich, T. C. Hender, and E. Nardon, "Modelling of plasma response to resonant magnetic perturbation fields in MAST and ITER", Nucl. Fusion **51**, 83002–83015 (2011).

[6]T. M. Bird and C. C. Hegna, "A model for microinstability destabilization and enhanced transport in the presence of shielded 3D magnetic perturbations", Nucl. Fusion **53**, 10.1088/0029-5515/53/1/013004 (2013).

[7]I. T. Chapman, A. Kirk, S. Saarelma, J. R. Harrison, and R. Scannell, "Towards understanding ELM mitigation: The effect of axisymmetric lobe structures near the X-point on ELM stability", Nucl. Fusion **52**, 10.1088/0029-5515/52/12/123006 (2012).

[8]R. Nazikian et al., "Pedestal bifurcation and resonant field penetration at the threshold of edge-localized mode suppression in the DIII-d tokamak", Phys. Rev. Lett. **114**, 10.1103/PhysRevLett.114.105002 (2015).

[9]O. Schmitz et al., "Aspects of three dimensional transport for ELM control experiments in ITER-similar shape plasmas at low collisionality in DIII-D", Plasma Phys. Control. Fusion **50**, 124029 (2008).

[10]J. D. Callen, C. C. Hegna, and A. J. Cole, "Magnetic-flutter-induced pedestal plasma transport", Nucl. Fusion **53**, 10.1088/0029-5515/53/11/113015 (2013).

[11]A. Kirk et al., "Effect of resonant magnetic perturbations on low collisionality discharges in MAST and a comparison with ASDEX Upgrade", Nucl. Fusion **55**, 043011 (2015).

[12]W. Suttrop et al., "Experimental conditions for suppressing Edge Localised Modes by magnetic perturbations in ASDEX Upgrade", 45th EPS Conf. Plasma Physics, EPS 2018 **2018-July**, 25–28 (2018).

[13]C. Paz-Soldan et al., "Observation of a multimode plasma response and its relationship to density pumpout and edge-localized mode suppression", Phys. Rev. Lett. **114**, 10.1103/PhysRevLett.114.105001 (2015).

[14]C. C. Hegna, "Effects of a weakly 3-d equilibrium on ideal magnetohydrodynamic instabilities", Physics of Plasmas **21**, 072502 (2014).

[15]M. Willensdorfer et al., "Plasma response measurements of external magnetic perturbations using electron cyclotron emission and comparisons to 3D ideal MHD equilibrium", Plasma Phys. Control. Fusion **58**, 10.1088/0741-3335/58/11/114004 (2016).

[16]M. Willensdorfer et al., "Three dimensional boundary displacement due to stable ideal kink modes excited by external n = 2 magnetic perturbations", Nucl. Fusion **57**, 10.1088/1741-4326/aa7f4c (2017).

Chapter 2

Background and Motivation

2.1 Fusion Energy

For the better part of a century, scientists have pursued the prospect of nuclear fusion as a clean, near-limitless energy source, hoping to harness its potential to fuel the world for millennia to come. From the initial design of magnetic confinement fusion devices in the 1950s to the groundbreaking physics and engineering of the upcoming ITER Tokamak, the scientific community has made significant progress towards a fusion device capable of energy production. However, there are still numerous hurdles to overcome before a fusion-fueled world becomes are reality.

In first-generation fusion reactors, a deuterium-tritium plasma is heated to high enough energies to maximize the fusion cross-section, such that the fusion reaction

$$ {}^{2}_{1}\mathrm{H} + {}^{3}_{1}\mathrm{H} \rightarrow {}^{4}_{2}\mathrm{He}[3.5MeV] + {}^{1}_{0}\mathrm{n}[14.1MeV] \tag{2.1} $$

frequently occurs. The primary job of a magnetic confinement fusion device is to maintain this plasma of sufficiently high energy for a long enough time that a surplus of energy is produced. This can be quantified in terms of the plasma density n, temperature T, and energy confinement time τ_E. It is necessary for a fusion reactor to achieve ignition, the point where the fusion process produces enough energy to become self-sustaining without external input

power, by satisfying the Lawson criteria

$$nT\tau_E > 5 \times 10^{21} \text{ m}^{-3} \text{ s keV} \tag{2.2}$$

in order to be a viable energy source[1]. The temperatures, densities, and confinement times necessary to satisfy this criteria have all been individually obtained, but have yet to be achieved simultaneously. The ITER Tokamak currently under construction is designed to be the first controlled fusion device to reach—and exceed—break-even, the point where fusion power is equal to the input power, marking a major milestone toward fusion energy.

Plasma stability plays a pivotal role in maintaining strong confinement such that the Lawson criteria can be achieved. The strongest instabilities typically occur when pressure or current gradients within the plasma exceed a critical value, and are best described by the magnetohydrodynamic (MHD) model[2]. These MHD instabilities can result in a large loss of confined particles and energy and set a number of hard limits on n, T, and τ_E. Empirically, the density n cannot exceed the "Greenwald limit", given by

$$n < n_G = \frac{I_p}{\pi a^2} \tag{2.3}$$

where I_p is the plasma current and a is the minor radius[3]. If the plasma density exceeds this limit, a major disruption occurs, resulting in the complete loss of confinement, potentially damaging the plasma-facing surfaces[2]. In addition the Greenwald limit, the Troyon beta limit[4] and the Kruskal-Shafranov current limit[5] place hard boundaries on the operational parameter space for tokamak devices.

Understanding and avoiding these MHD instabilities remains a critical area of research within the fusion community. The work in this thesis relates primarily to one instability—the edge localized mode[6]—which will be discussed in detail in chapter 2.5.

2.2 Plasma Confinement

There are a number of different magnetic confinement configurations, each with an associated set of confinement and stability properties that characterize the plasma and define the operational limits of the device. These devices make use of the same basic principle: charged particles orbit magnetic field lines, limiting their motion primarily to the direction parallel to the field. By configuring the magnetic field into a torus, as in figure 2.1, the magnetic field lines create a closed system that confines the plasma.

Unfortunately, in a purely toroidal device, the curvature of the magnetic field couples with the radial gradient in the magnetic field to cause the particles to drift perpendicular to the field until they eventually collide with the walls of the torus [1]. To avoid this problem, a poloidal magnetic field is introduced such that the magnetic field lines wind helically around the torus, as seen in figure 2.2. As particles traverse along the field lines of the axisymmetric torus, they spend time on both the inboard and outboard sides of the torus, such that both inward and outward drifting occurs resulting in a partial cancellation of the drift effects and significant increase to the confinement time of the particles[7].

2.2.1 Figures of Merit

It is useful to establish the terminology and figures of merit commonly used in magnetic confinement research, as they will frequently be referenced throughout this thesis. This section is meant to be a non-comprehensive overview of these concepts, and more information can be found in References [1, 2].

Magnetic Flux Surfaces:

While typical confinement devices are three-dimensional in structure, its is common for the magnetic configuration to be symmetric in the toroidal direction. When these axisymmetric plasmas are in equilibrium, the magnetic field lines form nested toroidal surfaces, as seen in

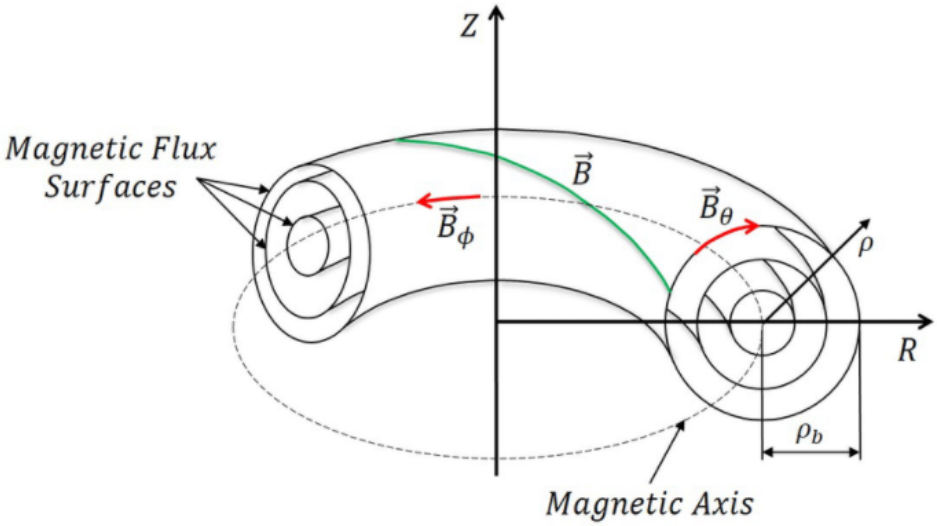

FIGURE 2.1: Schematic of a toroidal magnetic confinement scheme, including magnetic field, axis and flux surfaces. [9]

figure 2.1. It is convenient to define these surfaces in terms of a magnetic flux function, ψ, given as the flux contained within each magnetic surface[8]

$$\psi = \frac{\psi_p}{2\pi} \equiv \frac{1}{2\pi} \int \mathbf{B} \cdot d\mathbf{S}_p \tag{2.4}$$

which is also constant on that surface, such that

$$\mathbf{B} \cdot \nabla \psi = 0. \tag{2.5}$$

For equilibrium to exist, the magnetic force must balance with the force from the plasma pressure, such that

$$\mathbf{j} \times \mathbf{B} = \nabla p \tag{2.6}$$

where $\mathbf{j}$ is the current density, $\mathbf{B}$ is the magnetic field, and p is the plasma pressure. From this equation, it is clear that $\mathbf{B} \cdot \nabla p = 0$ and $\mathbf{j} \cdot \nabla p = 0$, implying that plasma pressure is also a flux function (i.e. $p = p(\psi)$), and that both the magnetic field lines and the current lines lie along the flux surface.

Conventionally, the magnetic flux function ψ is chosen to be the poloidal magnetic flux ψ_p in tokamak literature and the toroidal magnetic flux ψ_t for stellorators. It is worth noting that non-axisymmetric devices can also contain magnetic flux surfaces, though the existence of these surfaces is not guaranteed.

Safety Factor:

As mentioned in section 2.2, a purely toroidal magnetic field cannon confine charged particles, so a poloidal field is added such that the field lines helically wind around the device. The safety factor, q, gives a measure of how helical the magnetic field lines are on a given flux surface, making it a good marker for plasma stability. Generally, larger values of q result in increased stability.

The safety factor of a magnetic field line in defined as

$$q = \frac{1}{2\pi} \oint \frac{1}{R} \frac{B_t}{B_p} \mathrm{d}s \tag{2.7}$$

where B_t and B_p are the toroidal and poloidal magnetic field strengths of the field line, respectively, and the integral is carried out over a single poloidal circuit around the flux surface. Alternatively, the safety factor can be defined as

$$q = \frac{\mathrm{d}\psi_t}{\mathrm{d}\psi_p} \tag{2.8}$$

the rate of change of the toroidal flux with respect to the poloidal flux. It is often easiest to think of the q in terms of magnetic field line tracing: as one follows a field line around the torus, the safety factor is the number of toroidal transits that occur in one poloidal transit.

In tokamaks, the safety factor is strongly dependent on the plasma current profile, with typical values of $q \gtrsim 1$ in the core to $q = 2 - 8$ at the plasma edge.

Plasma Beta:

The plasma β is the ratio of the plasma pressure to the magnetic pressure, giving the efficiency of plasma confinement by the magnetic field. Assuming a pressure

$$\langle p \rangle = \frac{1}{V_p} \int p \, d\mathbf{r}, \tag{2.9}$$

averaged over the plasma volume V_p, plasma β is given as

$$\beta = \frac{2\mu_0 \langle p \rangle}{B^2}. \tag{2.10}$$

which is the ratio of the thermal pressure of the plasma to the magnetic pressure necessary to contain the plasma. It is useful to define the magnetic field for simple geometries in terms of

the toroidal (B_t) and poloidal (B_p) fields

$$B^2 = B_t^2 + B_p^2 = B_0^2 + \left(\frac{\mu_0 I}{2\pi a}\right)^2 \frac{2}{1+\kappa^2} \tag{2.11}$$

where B_0 is the vacuum toroidal field at the magnetic axis, I is the total toroidal plasma current, a is the minor radius, and κ is the plasma elongation (defined in figure 2.3). This allows β to be split into toroidal and poloidal components as well

$$\begin{aligned} \beta_t &= \frac{2\mu_0 \langle p \rangle}{B_0^2} \\ \beta_p &= \frac{4\pi^2 a^2 (1+\kappa^2) \langle p \rangle}{\mu_o I^2} \end{aligned} \tag{2.12}$$

such that

$$\frac{1}{\beta} = \frac{1}{\beta_t} + \frac{1}{\beta_p} \tag{2.13}$$

indicating that the efficiency of the magnetic confinement scheme is limited by the smaller of the two β_i.

2.2.2 Tokamaks

The tokamak is an axisymmetric plasma confinement device in which the principle magnetic field is in the toroidal direction (i.e. $B_p/B_t \ll 1$). This large toroidal field is generated by a set of toroidal field coils, as seen in figure 2.2. The poloidal field in a tokamak is primarily produced by passing a large toroidal current though the plasma. Most tokamaks use a large, central solenoid to generate this toroidal current, resulting in the lifetime of the plasma discharge often being limited by how long the solenoid current can be maintained.

External poloidal magnetic field coils are utilized to control the shape and vertical positioning of the plasma, and play an important role in plasma performance and stability. Modern tokamaks typically make use of the "D-shape" plasma (as seen in figure 2.3), in which the plasma has been elongated vertically from the circular shape and triangularity is added. This

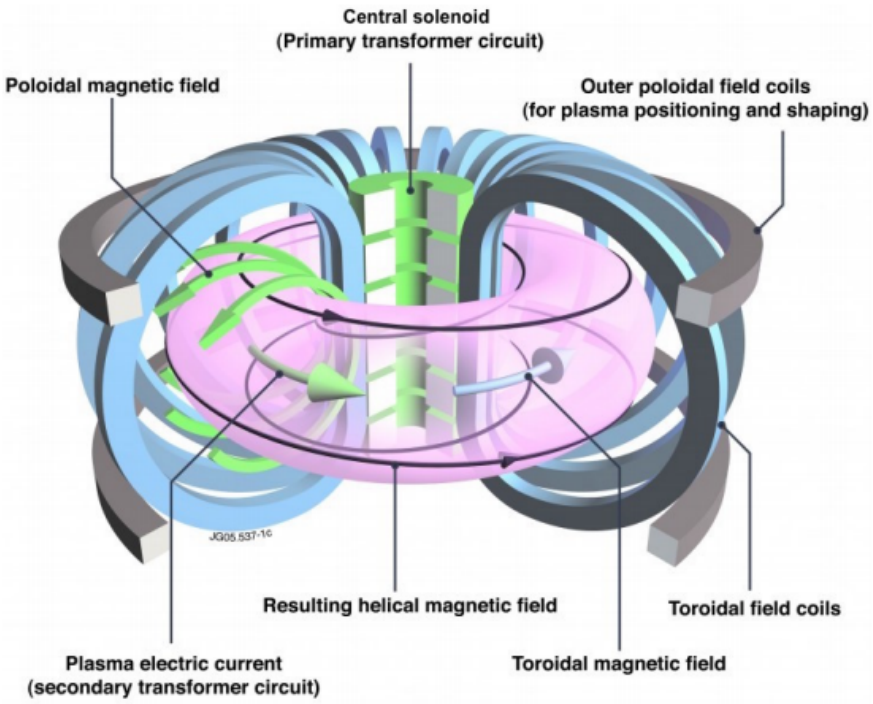

FIGURE 2.2: Schematic diagram of a tokamak including the major magnetic field and current elements. [10]

Machine	ITER	SPARC	JET	DIII-D	AUG	EAST	KSTAR	NSTX-U	MAST-U
R_0 [m]	6.20	1.85	2.96	1.66	1.65	1.70	1.80	0.93	0.85
a [m]	2.00	0.57	0.95	0.67	0.50	0.40	0.50	0.57	0.65
ϵ	0.32	0.31	0.32	0.40	0.30	0.24	0.28	0.61	0.76
B_0 [T]	5.3	12.2	4.0	2.2	3.9	5.0	3.5	1.0	0.8
I_p [MA]	15.0	8.7	6.0	3.0	1.4	0.5	2.0	2.0	2.0

TABLE 2.1: Comparison of machine size and peak operating parameters for select tokamaks, including the major radius R_0, minor radius a, inverce aspect ratio ϵ, and maximum toroidal magnetic field B_0 and plasma current I_p at the magnetic axis. [11–13]

.

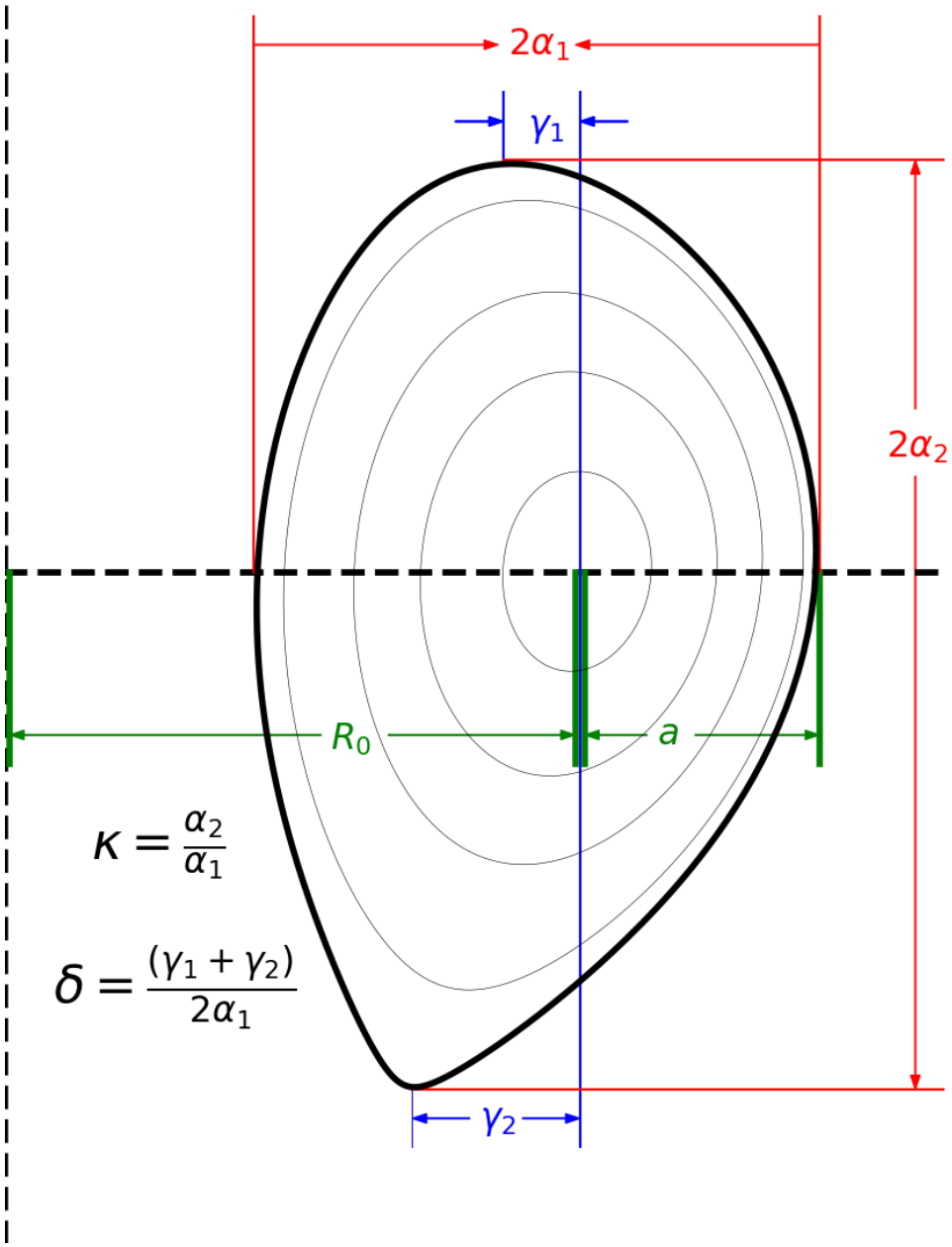

FIGURE 2.3: Poloidal cross section of a shaped tokamak discharge with major radius R_0 and minor radius a. The factors α_i and γ_i are used to determine the triagularity δ and elongation κ.

plasma shape is characterized by the aspect ratio A, elongation κ, and triangularity δ, given by[1]

$$A = \varepsilon^{-1} = \frac{R_0}{a} \qquad \kappa = \frac{\alpha_1}{\alpha_2} \qquad \delta = \frac{\gamma_1 + \gamma_2}{2\alpha_1} \tag{2.14}$$

respectively, where R_0 is the major radius, a is the minor radius, and the factors α_i, γ_i are defined in figure 2.3.

The direction in the plasma pressure gradient, ∇p, relative to the magnetic field line curvature, $\kappa = \hat{b} \cdot \nabla \hat{b}$, plays a critical role in determining plasma stability. In tokamaks, the outboard side consists of "bad" curvature ($\kappa \cdot \nabla p > 0$), making it prone to instabilities that can negatively impact confinement[2]. Conversely, the inboard side has "good" curvature leading to increased stability. The D-shaped plasma results in particles spending more time in good curvature region, minimizing the negative effects of the curvature.

Errors in magnetic field coil alignment can break the axisymmetry of the magnetic field configuration, potentially leading to instabilities and termination of the discharge[2]. To account for this, many tokamaks have 3D "saddle coils", which can apply non-axisymmetric perturbations to counteract these error fields. In some cases, 3D saddle coils are used to intentionally perturb the plasma, breaking the axisymmetry in the plasma edge and altering the behavior of edge localized instabilities. This 3D shaping of the plasma boundary is important to the research in this dissertation, and will be discussed at length in section 2.9.

Tokamaks are widely considered the leading candidate for the first generation of fusion reactors. Table 2.1 shows a number of currently active and upcoming research tokamaks, covering a wide range of sizes and operational parameters. More conventional tokamaks like DIII-D and AUG look to study a wide range of physics problems and are the workhorses of fusion research currently. Important engineering problems are also being addressed, but tend to be more unique to specific machines. For example, JET is the only active tokamak using D-T fuel and EAST is specifically designed for long pulse discharges.

Spherical tokamaks like MAST-U, NSTX-U, and PEGASUS-III are characterized by their small aspect ratios (relative to conventional tokamaks), and have a number of physics and

engineering benefits over conventional tokamaks. Most notable is that small aspect ratio devices are able to achieve significantly higher plasma β compared to conventional tokamaks. One large challenge for spherical tokamaks is the limits to the size of the central solenoid used for igniting the plasma and providing toroidal current. To get around this, non-solenoidal methods for plasma start-up and current drive are a major area of research for these devices.

Next generation fusion experiments like ITER and SPARC are expected to be completed in the mid-to-late 2020s. These devices are designed to operate in the "burning" plasma regime, such that the fusion power generated is greater than the input power, and alpha particles from the fusion reactions become the primary source for plasma heating. The majority of current fusion research is in support of these next generation devices to better predict and understand the physics and engineering challenges they may face.

Another class of confinement devices, the three-dimensional stellerators, offers a number of advantages and challenges relative to tokamaks. While the work in this thesis is primarily related to tokamak discharges, it deals largely with 3D geometric effects on plasma stability which may have applications for stellerator physics as well.

2.3 Ideal MHD Theory

The ideal magnetohydrodynamics (MHD) model presents a single-fluid description for the long-wavelength, low-frequency, macroscopic equilibrium and stability properties of a plasma, and is one of the simplest models for fusion plasmas[2]. MHD theory has been proven useful in describing some of the largest and most virulent plasma instabilities, making it a useful tool for defining the operational boundaries—critical values of plasma density, q, β, etc.—for a given magnetic configuration.

Despite ideal MHD being one of the simplest models, its equations are still highly nonlinear and complex, such that analysis using the full model can still be difficult. To get around this, it is typical to assume the plasma is at or near an equilibrium and linearize the ideal

MHD equations, only considering the effects of small deviations from this initial state. This linear MHD model provides the basis for a wide range of analytic and numerical theory, including the peeling and ballooning theories used in this work. These models are useful for determining the general stability properties of a wide range of plasma, but do lack information on the plasma dynamics themselves. Regardless, linear ideal MHD theory has proven to be an invaluable tool for studying fusion plasmas, and provides the basis for the analysis in this thesis. A detailed discussion of the ideal MHD model can be found in chapter 3.

It is important to note that ideal MHD is not universally valid, and does not describe a number of experimentally observed dynamics. There are a variety of physical phenomena important to fusion plasmas not addressed by the ideal MHD model, including [2]

- resonant particle effects
- finite Larmor radius effects
- classical and anomalous transport
- plasma-wall interactions
- resistive instabilities
- magnetic islands and stochasticity
- fast ion dynamics
- RF heating and current drive.

More complex models, such as extended MHD or the gyrokinetic model, are required (often in combination) to more accurately describe the wide variety of phenomena found in fusion plasmas.

2.4 The Transients Challenge

One of the greatest obstacles to next generation fusion devices, including ITER, is large-scale transient events[14]. The most dangerous of these phenomena are Disruptions[15] and Edge Localized Modes (ELMs)[6]. The causes of these events vary, but they are both characterized by their potential to rapidly release large amounts of stored energy, potentially damaging the confinement vessel or terminating the plasma discharge. In general, transient events are tied to magnetohydrodynamic (MHD) instabilities, often exhibiting fast nonlinear growth in short time-spans relative to other plasma phenomena.

The most extreme transient event is a disruption, in which confinement of the plasma is lost and the stored energy is released into the walls of the confinement vessel, potentially causing significant damage[15]. In general, most disruptions are caused by long-wavelength MHD instabilities[16], but there are a number of plasma phenomena that can result in a disruption, including ideal MHD kink modes and neoclassical tearing modes (NTMs)[17]. There are also external factors, such as power supply failures or a flake of wall material falling into the plasma, that can perturb the plasma leading to a disruption event[17].

The primary source of thermal energy loss in a disruption is through conduction to the vessel wall along magnetic field lines that are poorly confined due to a loss in toroidal symmetry or through radiation from impurities in the core of the discharge. This "thermal quench" can occur on the order of milliseconds in modern devices[16]. As the plasma rapidly cools, its resistivity rises significantly resulting in a decay of the plasma current, or "current quench", over tens to hundreds of milliseconds. The thermal quench, especially in the conductive loss case, can lead to localized heating and subsequent melting of plasma facing materials, while the current quench can generate large electromagnetic forces on the vacuum vessel. Disruption events can also produce relativistic runaway electrons[18–20]. In modern large tokamaks, 50-60% of the initial plasma current can be converted to these runaway electrons via Coulomb avalanche multiplication, creating a population of high energy electrons which subsequently

collide with the vessel walls[14, 21]. These effects are already damaging in current fusion experiments and could prove detrimental to ITER, in which predictions show current conversion to runaways could reach as high as 70%[14].

Edge localized modes are less volatile than disruptions, with typical large ELMs expelling around 10 percent of the plasma stored energy (as opposed to 100 percent for major disruptions)[6]. However, ELMs are cyclic in nature. Stored energy in the edge increases as edge plasma pressure gradients and current build up, followed by a sudden instability releasing the energy, after which the pressure gradients and current are reduced and can start to climb again. While single ELM events are small, ELM oscillations occurring hundreds of times per second in current devices, with cumulative effects creating problems for plasma and wall materials[6]. For ITER, energy loss from uncontrolled ELMs is predicted to exceed 30 MJ, with ELMS occurring multiple times a second[22]. Based on this, ELMs on ITER need to be largely mitigated or avoided completely.

The solution to the transients problem as discussed in disruption literature comes down to three key topics — prediction, avoidance, and mitigation — with parallel ideas being applied for edge localized modes[14]. Understanding the physics behind various transient events is paramount to any kind of transient control scheme, as physics models can be used to predict when and where these events occur. Avoidance of transient events is done through large scale control schemes, navigating the plasma through a parameter space where it remains stable to transient events. In the event that the ELMs or disruption are not properly avoided, mitigation of the effects is essential to the longevity of the machine. Mitigation can occur at a number of levels, from changing the size or frequency of the events, to increasing the system's resilience to the heat loads and currents generated.

2.5 Edge Localized Modes

In 1982, a new regime of plasma operation was discovered on the Axisymmetric Divertor Experiment (ASDEX)[23]. This new high confinement regime, H-mode, has shown to provide roughly a factor of 2 improvement in energy confinement time relative to the previous low confinement regime, L-mode[24]. The H-mode's most notable feature is the formation of a large transport barrier at the very edge of the plasma. The transport barrier is a narrow region of rapidly increasing thermal pressure and minimized thermal and particle transport perpendicular to the magnetic field[25]. This acts to "lift" the pressure and temperature profiles up from their L-mode values, and is thus referred to as the plasma pedestal. The significant increase in core plasma density and temperature observed in H-mode provided a regime in which fusion energy production becomes economically feasible[26].

However, there are concerns surrounding H-mode that the plasma confinement is actually too strong. With such low perpendicular particle transport in the edge, impurities in the core of the plasma can accumulate, increasing radiation losses from high-Z impurities and core fuel depletion[27]. A solution to this problem inherently exists in H-mode plasmas: the edge localized mode. The edge plasma pedestal leads to a steady increase in the edge pressure until an ideal MHD pressure limit is hit, triggering a peeling-ballooning instability[28]. The instability results in a rapid loss of confinement on the order of 10 percent of the total stored energy, as well as a collapse in the edge transport barrier, thus removing the drive for instability. Once the instability has stopped, a recovery period begins to rebuild the pedestal until it again reaches the stability limits and triggers another ELM. The cyclic nature of ELMS acts to pump impurities from the core plasma, limiting impurity accumulation and associated problems[6]. While this natural cleaning comes at the cost of stored energy, the confinement gains from H-mode operation far exceed the losses from ELMs.

Unfortunately, the presence of ELMs in H-mode operation is not without its drawbacks. In modern experiments, ELMs can release up to 1 MJ of plasma stored energy to the walls

per ELM[29]. This results in large transient heat loads to plasma facing surfaces, damaging the walls and introducing excessive core impurity injection and radiation. Projections to ITER and beyond predict large ELMs of 30-50 MJ per burst[22], causing irreparable damage to the first wall through melting and ablation, drastically lowering the lifetime of these components. As such, the minimization of the harmful effects of ELMs is paramount to the success of future fusion facilities.

There are currently a number of proposed solutions to mitigate or fully suppress ELMs in H-mode confined plasmas. For ELM mitigation, the general approach is to induce smaller, more frequent ELMs which release a fraction of the stored energy per ELM compared to the unmitigated or natural ELMs. One method for mitigating ELMs is pellet pacing[30, 31], where small fuel pellets are shot into the edge plasma, rapidly increasing the local density and triggering an ELM. The ELMs produced by pellet pacing will be relatively small, provided the pellet injection rate is greater than the natural ELM frequency. A secondary ELM mitigation is the application of 3D magnetic perturbations to the plasma edge[31–36]. These magnetic perturbations and the role they play in pedestal stability is the primary focus of this thesis, and will be further discussed in future sections.

In addition to minimizing the impact of ELMs for H-mode operation, new, alternative ELM-free confinement regimes are being investigated to address these issues. The first of these regimes is the ELM-suppressed regime, in which resonant magnetic perturbations are used to completely eliminate the ELMs in an H-mode plasma[31, 35, 37–40]. Similar to ELM mitigation, these ELM suppressed regimes are accessed using 3D magnetic perturbations, though the underlying mechanism appears to be different. In addition to active ELM suppression, there are a number of operational regimes that are naturally ELM free, such as QH-mode[41], I-mode[42], and EDA H-mode[43]. These regimes are characterized by enhanced steady-state transport in the plasma edge such that sufficient energy is released to avoid the onset of ELMs.

2.6 Phenomenological Description of ELMS

In order to better understand the edge localized mode, it is necessary to develop classifications for the different types of ELM phenomena. In order to do so, we can look at a large number of experiments that have observed a variety of ELM events. Studying these different experimental results has led to a general classification of the major ELM types[6], based on the occurrence of a magnetic precursor and the dependence of the ELM frequency on the energy flux through the separatrix, P_{sep}. Based on this, Ref.[6] defines three major types of edge localized events: Type I ELMs, Type III ELMs, and dithering cycles. This description ignores the type II ELMs, as they had not yet been well diagnosed.

For type I ELMs, the rate at which ELMs occur, ν_{ELM}, increases with the energy flux through the separatrix (i.e. $d\nu_{ELM}/dP_{sep} > 0$). Additionally, there is no clear coherent magnetic precursor for type I ELMs, though there are indications of precursor T_e osculations, and existence of a magnetic precursor has not been ruled out[6]. Type III ELMs differ in that the ELM repetition frequency decreases with flux across the separatrix (i.e. $d\nu_{ELM}/dP_{sep} < 0$). There is also an observed magnetic precursor oscillation of intermediate toroidal mode number located close to the plasma for type III ELMs, particularly on the low-field side of the discharge. Physically, both the type I and type III ELMs are MHD events lasting on the order of 1 ms, with high levels of magnetic fluctuations during the ELM crashes. Type III ELMs typically are smaller and have repetition frequencies ranging from 2-200 Hz, while type I ELMs range from 10-200 Hz and tend to be much larger. The lower limit on the ELM frequency is often comparable to the inverse of the confinement time.

Dithering cycles occur when the energy flux across the separatrix is near power threshold for the L-H transition (i.e. $P_{sep} \approx P_{thr}^{LH}$), such that the plasma cycles in and out of H-mode (called L-H-L transitions). There is no magnetic precursor observed in dithering cycles. As a noticeable difference from the other ELM types, dithering cycles are not MHD events, as there is only small magnetic fluctuations, but rather a limit cycle oscillation from the hysteresis in

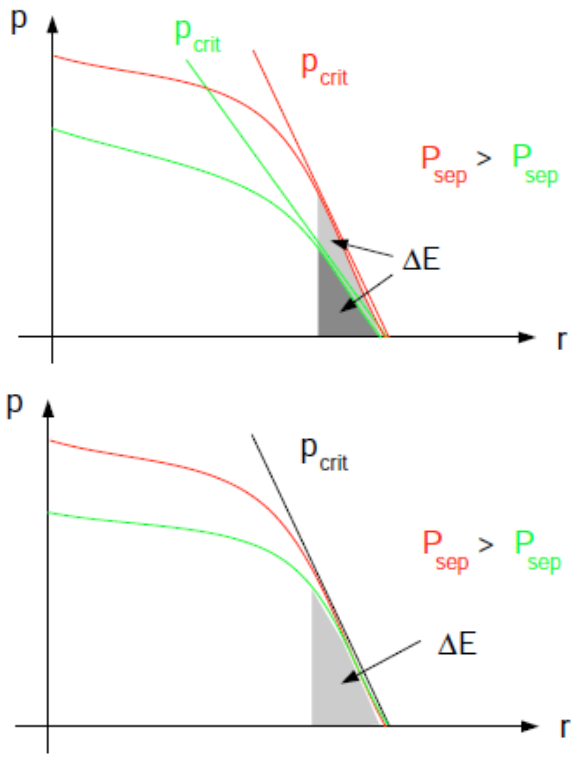

FIGURE 2.4: Sketch of the (a) type III ELM stability and (b) type I ELM stability. The red curves are the pre-ELM profiles, the green curves are the post-ELM profiles. [6]

the L-H transition[44].

Another prominent physical feature of the ELMs is the change in the density and temperature profiles during the event. Figure 2.4 shows the changing pressure profiles during type I and III ELMs. For type III ELMs, it is observed that the critical pressure gradient for the onset of instability increases with heating, developing a higher pressure gradient before the ELM. As a consequence, the ELM frequency decreases and the ELM energy change increases with heating[6]. For type I ELMs, the critical pressure gradient remains fixed, such that the ELM frequency increases with heating power, while the ELM energy change remains relatively constant[6].

The physical mechanism behind the different ELM types is still an active area of research. For type III ELMs, the ELMs are thought to be a resistive MHD instability, based on the critical role of the edge temperature plays in the behavior of the ELMs[45]. MHD models also exist for type III ELMs that predict the ELM mechanism to be peeling modes coupled to turbulent fluctuation in the edge[6]. Type I ELMs occur at higher temperatures than type III ELMs, meaning ideal MHD effects might be more important, which is consistent with ideal MHD analysis for these instabilities. This leads to an MHD model for type I ELMs as coupled peeling-ballooning modes, with a critical edge pressure gradient being a key factor in the onset of the instability[28]. However, the ideal ballooning stability limit is found to be a necessary, but not sufficient condition for instability, implying additional physics are important.

As a final note, there are a number of other ways to classify ELMs that are used throughout the literature. These definitions are found to vary slightly based on machine, and can be dependent on the size of the ELMs, the ELM signature in the D_α signal in the plasma edge, or their location on the peeling-ballooning stability diagram (figure 2.10). In this work, we primarily consider type I ELMs as defined above, which are related to MHD driven peeling-ballooning modes.

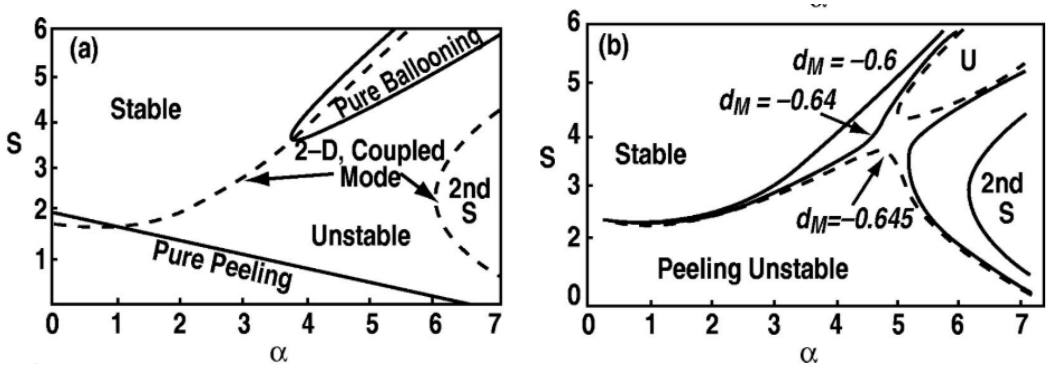

FIGURE 2.5: The marginal stability contours in $\hat{s} - \alpha$ space for (a) the $n = \infty$ pure peeling and pure ballooning modes, as well as the $n = 20$, $d_M = -0.6$ 2D coupled peeling-ballooning mode and (b) a sequence of curves for the $n = 20$ 2D coupled mode, with $d_M = -0.6, -0.64, -0.645$, showing second stability access reopening at the deepest well ($d_M = -0.645$). [48]

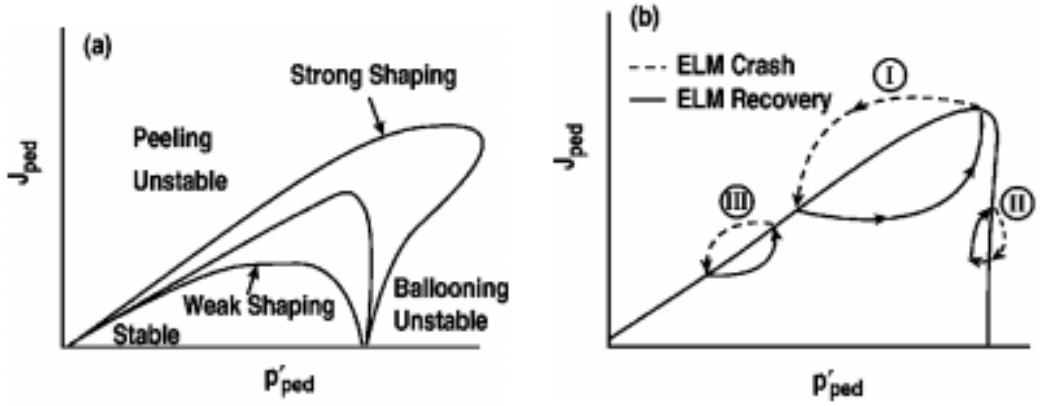

FIGURE 2.6: (a) Schematic diagram of stability limits in p'_{ped}, $J_{ped}/\langle J \rangle$ space, for a variety of cross section shapes. (b) Proposed simplified model of small and large ELM cycles. [28]

2.7 ELMs as Peeling-Ballooning Modes

As mentioned in the previous section, it has been found that type I ELMs can be represented by coupled peeling-ballooning instabilities. In this model, there are two limiting factors on the stability of the plasma pedestal: the critical pressure gradient determined by the ideal ballooning limit, and the effects of finite edge currents driving external kink or "peeling" modes[28, 46]. Additionally, these two instability drives can couple together, resulting in coupled peeling-ballooning instabilities that are more unstable than the sum of the two original modes[47].

Pressure driven high-n ideal ballooning modes provide a starting point for studying type I ELMs. The high-n ballooning limit correlates well to the observed type I ELM threshold in certain experimental regimes, but the ideal ballooning limit can be exceeded and ideal theory can break down in some experiments[49, 50]. This occurs when the observed mode number becomes too low, such that the formally infinite-n ballooning theory is no longer applicable. To resolve this, it is necessary to include the effects of the edge current and finite n modes, as the coupling of the peeling-ballooning modes becomes more virulent for lower n[28]. The effects of the edge current is two-fold, providing a source of free energy for the external kink or "peeling" mode, while reducing the magnetic shear in the pedestal and stabilizing high-n ballooning modes[51, 52].

Peeling modes are found to be the most unstable when a rational surface $(q = m/n)$ resides just outside the plasma boundary, minimizing the vacuum stabilization and resulting in the stability criterion[53]

$$\sqrt{1 - 4D_M} > 1 + \frac{2}{2\pi q'} \oint \frac{J_\parallel B}{R^2 B_p^3} dl, \tag{2.15}$$

where D_M is the Mercier coefficient[54], $J_\parallel$ is the current density in the direction of the magnetic field $\mathbf{B}$, q' is the radial derivative of the safety factor with respect to the poloidal flux, B_p is the poloidal field, and dl is the poloidal arc length (with all quantities evaluated at the

plasma surface). Based on this, for peeling modes, the edge current is destabilizing, while magnetic shear and the pressure gradient are stabilizing. This is illustrated in figure 2.5, which shows the dependence of peeling and ballooning modes (as well as their coupling) on magnetic shear ($\hat{s}$) and the pressure gradient (α)[48].

In the infinite-n limit, the "pure peeling" and "pure ballooning" limits are obtained with simple 1D calculation[53], including the so-called secondary stability region at low shear and high pressure gradient, between the pure modes. For finite values of n, the peeling and ballooning modes couple and act to "close-off" access to the secondary stability region. Shaping also plays an important roll in stability and coupling, which is shown in figure 2.5b through the "magnetic well factor" $d_M = D_M \hat{s}^2/\alpha$, which accounts for the plasma shaping and finite aspect ratio effects[28]. It is observed that increasing the magnetic well factor (through increased magnetic shear or decreased pressure gradient) acts to decouple the peeling and ballooning branches, allowing access to the secondary stability regime.

Figure 2.6 shows the stability boundaries when accounting for variations in the edge current. Peeling modes are destabilized with large J_{ped} and stabilized with increasing p'_{ped}, while ballooning modes are destabilized at high p'_{ped} and low J_{ped}. Coupled peeling-ballooning modes are driven unstable when both p'_{ped} and J_{ped} are large, leading to the 'nose' of the stability diagram observed in figure 2.6. Again, plasma shaping plays a key role in peeling-ballooning stability (figure 2.6a), as increasing the shaping leads to decoupling of the ballooning and peeling modes driving up the p'_{ped} and J_{ped} necessary for instability and generally lowers the toroidal mode number n.

Using the coupled peeling-ballooning model, a mechanism for the ELM cycles is observed (figure 2.6b), with the exact behavior varying based on where on the stability boundary the ELM is triggered. In all cases, the pedestal gradient increases between ELMs on a transport time scale with the current (primarily bootstrap) rising as well. For type I ELMs, high power and low density result in the stability boundary being reached at high p'_{ped} and J_{ped}. This results in large ELM events triggered by a low-n peeling-ballooning mode with a broad radial

structure and the initial pedestal collapse leaves the pedestal in the unstable domain while the current reduces at a slower rate[28]. Similar cycles are observed for type II and type III ELMs, with smaller ELM crashes predominately due to the more localized structure of the modes.

This model of ELMs as coupled peeling-ballooning modes is the foundation of a number of ideal MHD stability codes, including the Edge Localized Instabilities in Tokamak Experiments (ELITE) MHD stability code[46] and Peeling-Ballooning in 3D (PB3D) code, which will be discussed later in this report.

2.8 The EPED Model

Having established a physical basis for ELMs as peeling-ballooning modes, the next step is to create predictive models for the pedestal stability limits. This was done by Snyder *et al.* making use of the peeling-ballooning constraint, as well as the kinetic ballooning mode (KBM) limit, to determine the pedestal height and width at the onset of ELMs[55, 56]. The EPED model allows for predictions to be made prior to experiments to predict the stability of the discharges and optimize performance. It has been widely successful in predicting the experimental conditions, as seen in figure 2.7, which shows a comparison between the EPED predictions and experimental results from 288 cases across 5 separate machines[57].

At its core, the EPED model consists of two primary constraints: the peeling-ballooning (P-B) stability limit and the KBM stability limit. The P-B constraint makes use of the theory presented in the previous section, in which ELMs can be treated as coupled peeling-ballooning modes, and the P-B stability boundary is calculated using the ELITE code[46]. The stability of KBMs has been extensively studied using linear and nonlinear gyrofluid and gyrokinetic simulations, as well as semi-analytic treatments[58, 59], and can be considered the kinetic equivalent to the local ideal MHD ballooning mode, with the KBM being destabilized at critical pressure gradients near the ideal stability limit.

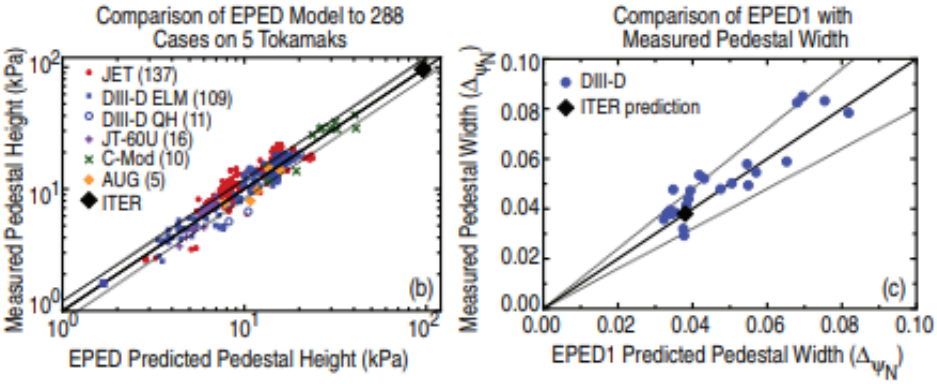

FIGURE 2.7: (b) Comparison of EPED prediction to observed pedestal height for 288 cases on 5 tokamaks, with ITER baseline prediction also shown (black diamond). (c) Comparison of EPED prediction to pedestal width measured with high resolution Thompson scattering on DIII-D, with ITER baseline pedestal width prediction also shown (black diamond). [57]

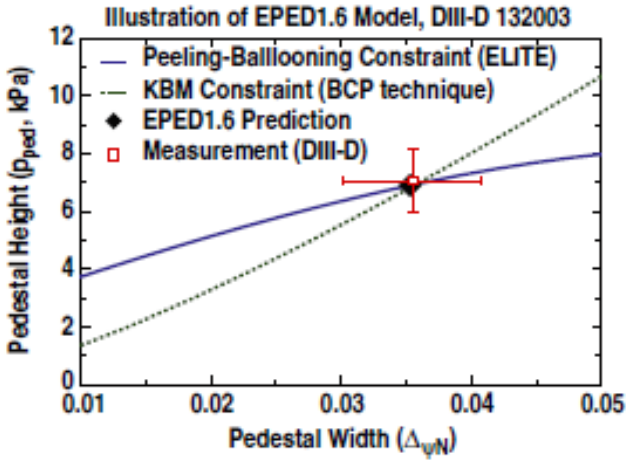

FIGURE 2.8: The EPED1.6 model predicts a pedestal height and width (solid diamond) from the intersection of calculated P-B (solid line) and KBM (dotted line) constraints. This can then be compared with observations, here shown by an open square, for DIII-D discharge 132003. [55]

While the P-B mode is global with a large radial extent, the KBM is mostly localized to specific unstable flux surfaces, and can be used to develop a relationship between the pedestal height and width. Combining these two constraints gives a model for predicting the height and width of the plasma pedestal. This is illustrated in figure 2.8. The solid blue line gives the P-B constraint while the dotted green line gives the KBM constraint. The diamond corresponds to the intersection of the two models, which is the predicted pedestal height and width.

The EPED model assumes confinement from the H-mode edge transport barrier is good enough that profiles will rise until the P-B and KBM stability limits are reached. At the onset of H-mode, the initial pedestal is narrow and stable. This barrier will steepen until the KBM boundary is reached locally, and then pedestal height and width will increase along the KBM constraint until the P-B boundary is reached and an ELM occurs (for large ELM regimes). Based on this model, it can be noted that pedestal height can be increased by either improving the P-B stability, or by degrading the KBM stability.

2.9 3D Magnetic Perturbations

There is a long and rich history of the use of applied non-axisymmetric magnetic perturbations (NAMPs) in tokamaks, with a particular focus on resonant magnetic perturbations (RMPs). In early experiments, field perturbations were typically applied using external error field correction coils (EFCC), while most modern experiments make use of a set of in-vessel saddle coils, which provide faster response times. An example of the in-vessel saddle coils is provided in figure 2.9. Early experiments on the TEXT device showed NAMPs are capable of modifying the edge plasma transport and subsequent performance of the tokamak[60, 61]. This motivated a large number of studies on the increase in particle transport during NAMPs (the so-call "density pump-out") on a number of tokamaks[62–64] and the Wendelstein 7-AS stellarator[65]. Based on these experiments, the use of NAMPs to control ELMs

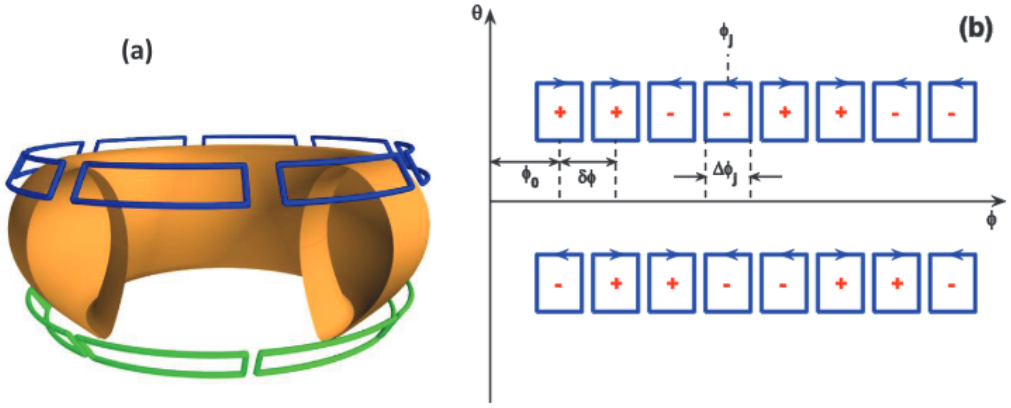

FIGURE 2.9: A sketch of the RMP coils distribution on AUG in (a) real geometry, and (b) on the (ϕ, θ)-plane. Shown in (b) is also an example of the coil current phasing of $(\Delta\phi_{UL} = 90^\circ)$ between the upper and lower rows, for the $n = 2$ configuration. [67]

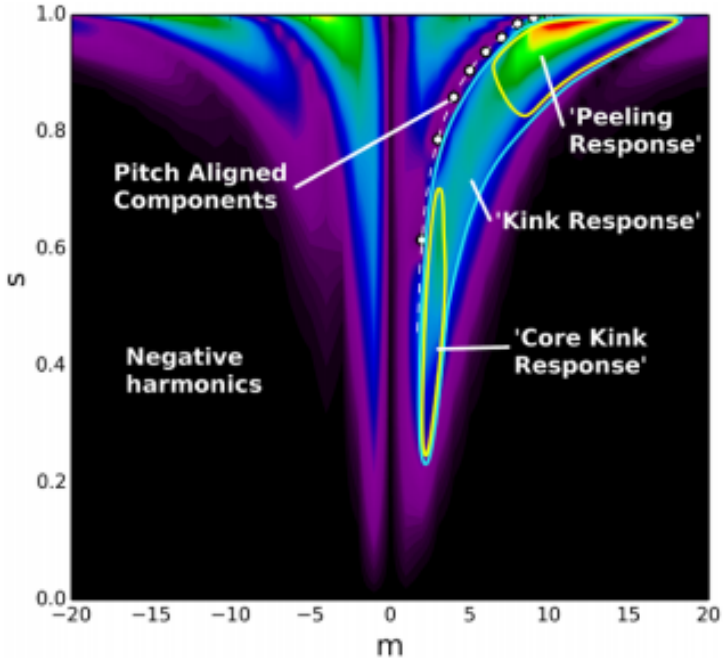

FIGURE 2.10: Spectrogram of the total field in response to an even coil configuration $(\Delta\phi_{UL} = 0^\circ)$. The spectral regions (i.e. regions in poloidal mode number m and normalized radius s) referred to as 'Kink', 'Core Kink', and 'Peeling' are labelled. [68]

was proposed[66].

The effects of NAMPs on axisymmetric plasma discharges is still an active area of research, as there are a number of complex plasma responses to consider. There are generally considered two types of major plasma responses to low-n externally applied field perturbations: the core kink response and the edge peeling-tearing response[67]. For the core kink response, the plasma displacement occurs globally, penetrating through the entire plasma column. The edge peeling-tearing response distributes the plasma displacement entirely in the edge region, with both resistive tearing effects and ideal kink-peeling effects observed. Figure 2.10 illustrates the types of response discussed above and where they are radially localized. Here, the poloidal harmonics for the magnetic field after the plasma response to the MPs has occurred is shown with various spectral regions (regions of poloidal mode number m and radius s). The white line shows the safety factor with dots indicating rational surfaces, which act to screen magnetic perturbations causing a "build-up" in the kink response for $m > qn$[68]. In this example, the peeling response is dominant, while the edge kink and core kink are relatively small.

The kink-peeling is characterized by a number of plasma phenomena: (1) a stable pressure-driven kink mode, with surface displacements localized on the LFS of the plasma[69], (2) a large peeling response localized to the top and bottom of the torus near the equilibrium X-points[70], and (3) plasma "lobe" structures in the X-point, often with partial divertor detachment[71]. The tearing response is often highly coupled to the kink-peeling response, but adds in resistive effects such as magnetic island formation localized to rational surfaces ($q = m/n$) and potential edge stochasticity[67].

Another key property of applied 3D magnetic perturbations is the so-called "density pump-out" effect[67, 72]. The density pump-out is a decrease in core plasma density during some NAMP operation, indicating an increase in radial particle transport. It is worth noting that pump-out does not occur in all NAMP discharges, and can occur in both L- and H-mode operation[72]. Studies have shown that the density drop is more strongly tied to the peeling

response near the X-point, rather than the outboard mid-plane kink[70, 72–74]. Additionally, the pump-out only appears in NAMP discharges with moderate to low collisionality ($\nu^* \lesssim 1.0$)[75], though this may be related to increases in core fueling in higher collisionality discharges, rather than a collisionality dependence on the transport[39, 76]. It is worth noting that ELM mitigation correlates strongly with the pump-out when present, implying the underlying transport changes may be related[70, 73, 77]. The mechanism behind this change in transport is still an open topic of research, though particle transport through stochastic magnetic fields appears to play an important role[72], as does changing X-point stability[71].

In more recent works, the effects of the plasma response to NAMPs has been studied, and shows a large variation from the predicted vacuum response models[67, 74, 78]. In-vessel coils with 2 rows were studied. It was seen that plasma response from the upper and lower coils couple, leading to increases/decreases in some parts of the plasma response, based on the phase angle between the two coil sets ($\Delta\phi_{UL}$). Based on the relative coil phases, the core kink and edge peeling-tearing response can change, as can the magnitude of the surface displacement at the LFS mid-plane and the X-point[67]. Furthermore, these parameters were found to vary with edge safety factor and the triangularity of the discharge[78]. Finally, it is worth noting that for finite-β plasmas, the core kink response is almost entirely suppressed by sound wave damping[67]. These studies show that the optimal coil configurations for maximizing the plasma response to the NAMPs are often different from the vacuum response optimization, and that optimization of the plasma response results in the greatest ELM mitigation[67, 74].

As mentioned previously, applied 3D magnetic perturbations can also impact the stability of ELMs in H-mode discharges. This is generally divided into two sub-topics: ELM mitigation and ELM suppression. ELM mitigation with NAMPs typically involves increasing the frequency and decreasing the size of type-1 ELMs, or replacing the type-1 ELMs with high frequency "mitigated-ELMs". ELM suppression, on the other hand, completely eliminates all types of ELMs. These two issues will be the topics of the following sections.

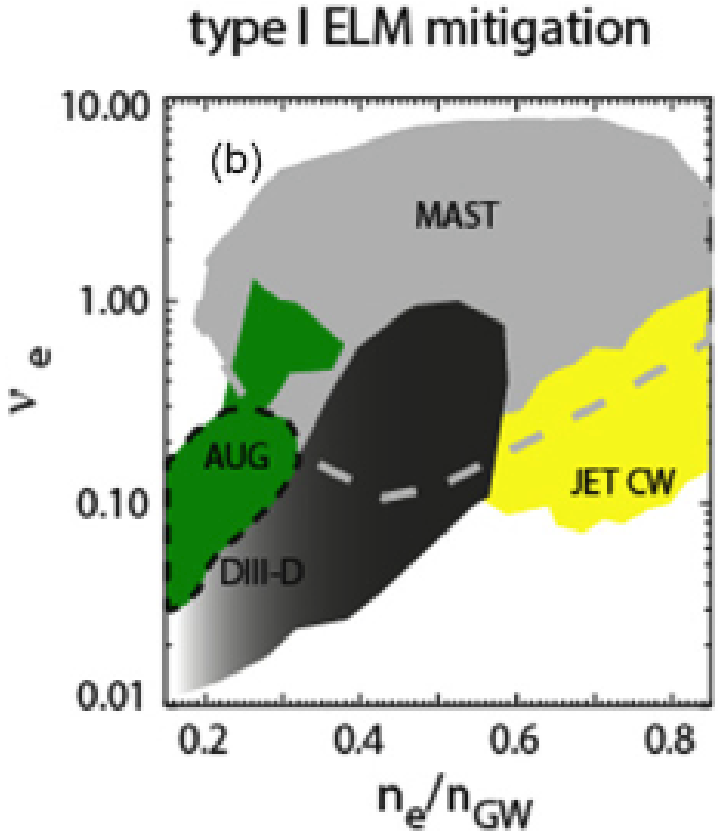

FIGURE 2.11: Experimentally determined access condition in terms of pedestal collisionality (ν_e^*) versus pedestal density as a fraction of the Greenwald density (n_e/n_{GW}) for type I ELM mitigation. [74]

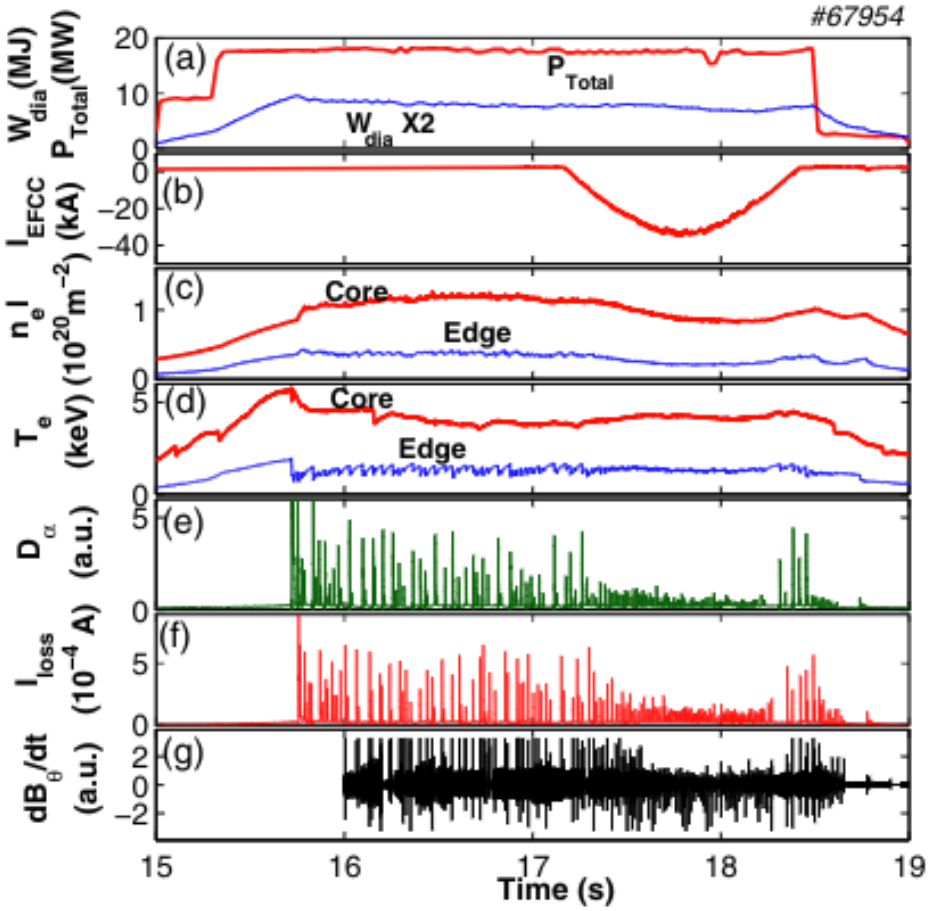

FIGURE 2.12: Overview of a typical ELM mitigation experiment on JET. [32]

2.10 ELM Mitigation

Experiments were performed that showed applied 3D MPs in diverted tokamaks could destabilize small ELMs in an otherwise ELM-free H-mode plasma[79]. The cause of this result was thought to be an uncontrolled rise in the density. This motivated one approach for ELM mitigation, in which smaller, high frequency ELMs are triggered in order to avoid reaching the natural ELM threshold. A number of experiments have been able to obtain ELM mitigation with NAMPs in various configurations, including JET[32], ASDEX Upgrade[33], MAST[34], and DIII-D[80]. These experiments showed the wide range of applicability of NAMP ELM mitigation, covering a large set of parameters including density, collisionality, and edge safety factor. In most of these cases, the mitigated ELM plasmas showed similar confinement, similar plasma density, and lower core impurities concentration compared to the unperturbed ELMy reference plasmas[33].

Early ELM mitigation experiments appeared to have dependence on the Greenwald density fraction (n_e/n_{GW})[33] and pedestal collisionality[80], though subsequent experiments have shown mitigation to be independent of these parameters[74], as seen in figure 2.11. It is worth noting that the low collisionality, high density regime missing in that figure is not accessible in current machines, but will be important for ITER. More recent proposals have identified a number of possible causes for increased transport and decreased edge stability observed in ELM mitigation[71], including (1) the deformation of the plasma shape, which is related to ballooning stability, (2) change in the edge rotation shear, which can affect peeling-ballooning stability[72], (3) toroidal periodicity, which can result in 3D localization of ballooning modes[81], or (4) lobe structures at the X-point enhancing the effects of the bad curvature region[71]. The proposed work to be addressed here is primarily concerned with the effects of (1) and (3).

Figure 2.12 shows an example discharge from JET showing ELM mitigation using $n = 1$ resonant magnetic NAMPs[32]. It is seen that application of the NAMPs cause an increase of

ELM frequency from 30 Hz to 120 Hz, with the energy loss per ELM decreasing from near 7% to less than 2%. Additionally, there is a small decrease in the core plasma density (pump-out), while the core temperature remains unchanged. The increase in ELM frequency appears to correlate with the magnitude of the pump-out, implying the changes in transport play an important role in ELM mitigation. The behavior observed in figure 2.12 is characteristic of most ELM mitigation cases, though it is worth noting that pump-out is not always observed in high collisionality ELM mitigation cases, which may be related to increased core fueling and edge recycling rates[39].

There has recently been a large effort to study the plasma response to NAMPs, and how they relate to changes in edge stability[78, 82, 83]. It has been shown that the plasma response plays a key role in ELM mitigation. In particular, there is strong correlation between ELM mitigation and the edge peeling response in MAST[72] and ASDEX Upgrade[68, 74] due to changes in 3D geometry near the X-point. Additionally, the edge kink response seems to play a role in ELM mitigation[83, 84], as it can lead to toroidal localization of ballooning instabilities[85], which will be discussed in chapter 4.

2.11 ELM Suppression

ELM suppression can be separated into two key groups: Type-I ELM suppression and complete ELM suppression. Type-I ELM suppression has been observed on a wide range of devices, and is characterized by the absence of large ELMs, as seen in figure 2.13. In type-I ELM suppression, large ELMs (50 Hz) vanish, but are replaced by small, repetitive transport events (400-800 Hz) with similar features to ELMs, which have been classified as "mitigated ELMs"[33]. This "ELM-mitigated phase" is different from the previously discussed ELM mitigation, as the diverter heat loads become negligibly small, while preserving the beneficial core impurity reduction[33, 77]. As such, it is possible that this form of ELM suppression

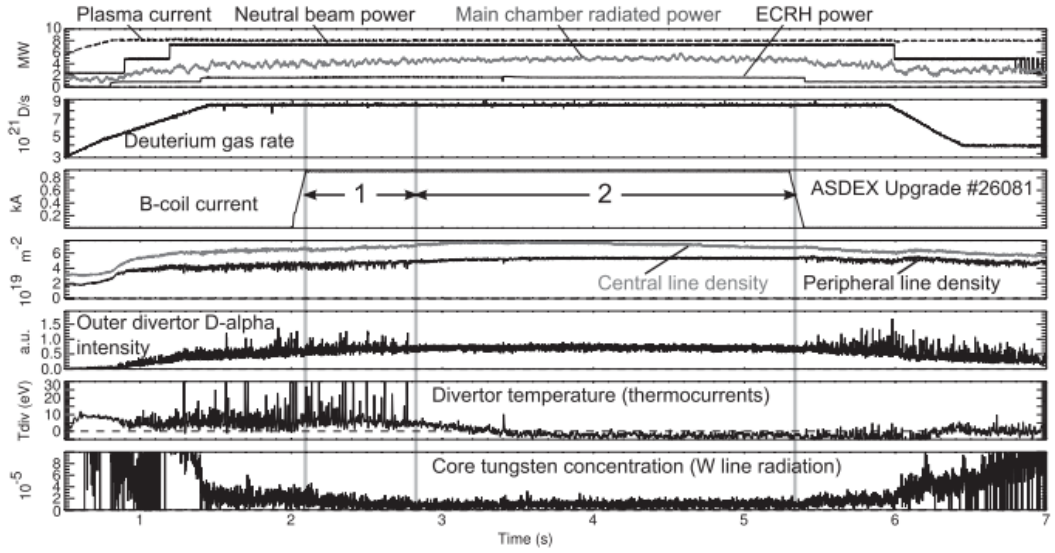

FIGURE 2.13: Time traces of ASDEX Upgrade discharge 26081 with B coils operating in odd parity (resonant). Time intervals marked "1" and "2" show a reduction of type-I ELM frequency and full suppression of type-I ELMS, respectively. [86]

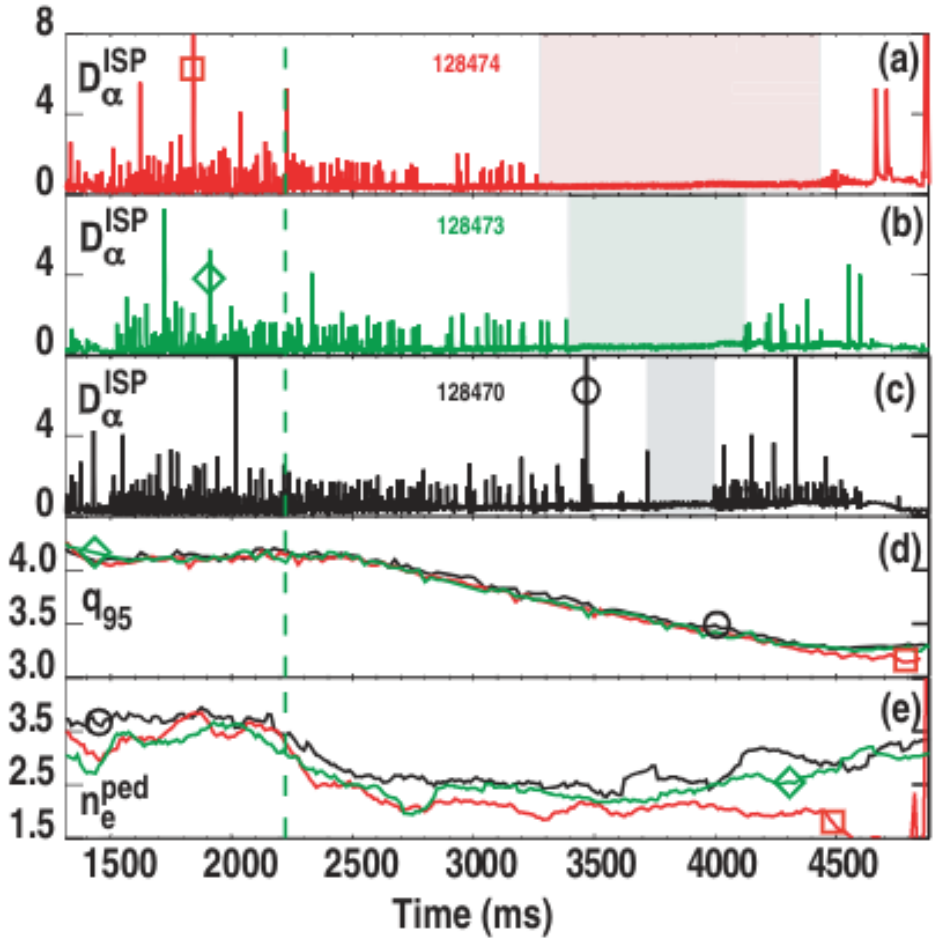

FIGURE 2.14: I

SP D_α intensity for each discharge, (d) q_{95} from standard EFITs, and (e) pedestal electron density. I-coil current, $\delta b_r^{11/3}/B_T$, and C-coil current are (a) 4.0 kAt, 3.2 $\times$ 10$^-$4, 9.6 kAt, (b) 3.0 kAt, 2.5 $\times$ 10$^-$4, 9.6 kAt, (c) 3.0 kAt, 2.5 $\times$ 10$^-$4, 4.8 kAt. I-coil turn on at green dashed line.]Time histories of parameters from discharges with different combinations of $n = 3$ RMP from the I-coil and $n - 1$ perturbation from the C-coil, including [(a)-(c)] ISP D_α intensity for each discharge, (d) q_{95} from standard EFITs, and (e) pedestal electron density. I-coil current, $\delta b_r^{11/3}/B_T$, and C-coil current are (a) 4.0 kAt, 3.2 $\times$ 10$^-$4, 9.6 kAt, (b) 3.0 kAt, 2.5 $\times$ 10$^-$4, 9.6 kAt, (c) 3.0 kAt, 2.5 $\times$ 10$^-$4, 4.8 kAt. I-coil turn on at green dashed line. [88]

is actually an extreme case of ELM mitigation, with the underlying physical mechanism remaining the same. Type-I ELM suppression has been observed on ASDEX-Upgrade[74, 86], MAST[74], and JET with an ITER-like wall, but not with the Carbon wall[87] .

By contrast, complete ELM suppression is characterized by the absence of all ELM-like events, with the underlying physics appearing to differ from that of typical ELM mitigation. First discovered on DIII-D[38], complete suppression has since been achieved on KSTAR[40, 89], EAST[90], and ASDEX Upgrade[91]. Complete suppression has been observed at a number of operational points, including both low collisionality (DIII-D and ASDEX Upgrade) and high collisionality (EAST and KSTAR), over a wide range of edge safety factors, making it a promising candidate for ITER and beyond.

The mechanism behind ELM suppression is not known, but it has been shown to depend highly on the value of the edge safety factor and the plasma shaping. Experiments have shown operational windows in q_{95} that noticeably avoid dominant rational surfaces in the edge (i.e. $q_{95} = 3.5, 4.0$ for $n = 2$ RMPs)[38]. It has been shown that strong plasma shaping is important for accessing an ELM suppressed regime[92]. There are a number of other factors that may play a role in ELM suppression, including wall conditioning, neutral particle recycling, gas fueling, and edge Z_{eff}[31], as well as plasma rotation[93]. There have been clear observations of an increase in edge turbulence and transport in ELM suppressed plasmas[94].

Figure 2.14 shows an example of complete ELM suppression on DIII-D[88]. All three discharges have clear windows of ELM suppression, with the width of the ELM suppressed region increasing with increasing I- and C-coil currents. Spectrographs of these discharges show the primary response is the $n = 1$ edge kink-peeling from the C-coils, thought the $n = 3$ response to the I-coils is present. The edge safety factor windows are clearly observed, centered at $q_{95} \approx 3.55$, and increasing in width with RMP strength, staying within the $10/3$ and $11/3$ surfaces. The cause of this widening is not fully understood, but correlates well with growth of and subsequent overlap of edge islands[88], resulting in a loss of confinement. While this has proven to be a decent metric, the plasma response also needs to be considered.

It is widely believed that ELM suppression occurs when transport mechanisms limit the pedestal height to a point that is stable to ELMs, but the cause of this increased transport is still under investigation. One theory is that RMPs create a magnetic island at the pedestal top that restricts its height[93]. Another theory relies on stochastic field produced near the X-point leading to higher edge transport[39]. A third theory is that the plasma response to the 3D fields that changes the stability properties also affects the underlying turbulence and plasma transport[81]. Finally, magnetic flutter (radial perturbations of magnetic field lines between island chains) has been shown to increase transport near rational surfaces[95]. These theories are all active areas of research, with efforts focused on relating these underlying mechanisms to the observed experimental behavior discussed above.

Complete ELM suppression comes with a number of advantages over traditional ELM mitigation. The primary advantage is the large reduction of the divertor heat fluxes, even compared to ELM mitigated discharges[38]. Additionally, while there is a decrease in pedestal density for ELM suppressed discharges, the core density and temperature are often greater than the ELMing case[31]. Finally, the absence of ELMs leads to less impurity production and material migration in the divertor region, leading to a reduction of edge impurities[31].

ELM suppression also introduces new difficulties that need to be addressed for future experiments. The first is the access regimes for complete ELM suppression. Current ELM suppression experiments have found a much more restrictive operational space in comparison to ELM mitigation experiments[74]. Most notably is an apparent temperature and density limit for full ELM suppression[91], which may become important for ITER scale experiments. Additionally, the need for strong control of edge safety factor further limits the operational space. Another issue is the large decrease in core impurity pumping normally associated with ELMy plasmas[31]. While the rate of impurities entering the core is decreased, there is no natural mechanism for removing impurities that do build up, leading to increased radiative losses in the core. These issues must be addressed for future fusion devices.

References

[1]J. Wesson, *Tokamaks*, 4th ed. (Oxford University Press, 2011).

[2]J. P. Freidberg, *Ideal mhd* (Cambridge University Press, 2014).

[3]M. Greenwald, "Density limits in toroidal plasmas", Plasma Physics and Controlled Fusion **44**, R27–R53 (2002).

[4]F Troyon, R Gruber, H Saurenmann, S Semenzato, and S Succi, "MHD-limits to plasma confinement", Plasma Physics and Controlled Fusion **26**, 209–215 (1984).

[5]M. D. Kruskal, M. Schwarzschild, and S. Chandrasekhar, "Some instabilities of a completely ionized plasma", Proceedings of the Royal Society of London. Series A. Mathematical and Physical Sciences **223**, 348–360 (1954).

[6]H. Zohm, "Edge localized modes (ELMs)", Plasma Phys. Control. Fusion **38**, 105–128 (1996).

[7]R. Hazeltine and J. Meiss, *Plasma confinement* (Dover Publications, Inc., 2003).

[8]W. D. D'haeseleer, W. N. Hitchon, J. D. Callen, and J. L. Shohet (Springer-Verlag Berlin Heidelberg, 1991).

[9]J. Barton, W. Wehner, E. Schuster, F. Felici, and O. Sauter, "Simultaneous closed-loop control of the current profile and the electron temperature profile in the tcv tokamak", Proceedings of the American Control Conference **2015**, 3316–3321 (2015).

[10]EUROFusion, *Tokamak principle*, (2011) `https://www.euro-fusion.org/news/detail/tokamak-principle` (visited on 10/04/2020).

[11] A. J. Creely et al., "Overview of the sparc tokamak", Journal of Plasma Physics **86**, 865860502 (2020).

[12] PPPL, *Nstx upgrade overview*, (2020) https://nstx-u.pppl.gov/nstx-upgrade (visited on 10/04/2020).

[13] P.-I. Experiment, *Pegasus-iii experiment*, (2020) https://pegasus.ep.wisc.edu/ (visited on 10/04/2020).

[14] T. C. Hender et al., "Chapter 3: MHD stability, operational limits and disruptions", Nucl. Fusion **47**, 10.1088/0029-5515/47/6/S03 (2007).

[15] B. B. Kadomtsev, "Behaviour of disruptions in tokamaks", Plasma Phys. Control. Fusion **26**, 217–226 (1984).

[16] J. A. Wesson et al., "Disruptions in JET", Nucl. Fusion **29**, 641–666 (1989).

[17] P. C. De Vries, M. F. Johnson, B. Alper, P. Buratti, T. C. Hender, H. R. Koslowski, and V. Riccardo, "Survey of disruption causes at JET", Nucl. Fusion **51**, 053018 (2011).

[18] M. N. Rosenbluth and S. V. Putvinski, "Theory for avalanche of runaway electrons in tokamaks", Nucl. Fusion **37**, 1355–1362 (1997).

[19] A. H. Boozer, "Runaway electrons and ITER", Nucl. Fusion **57**, 10.1088/1741-4326/aa6355 (2017).

[20] H. Smith, P. Helander, L. G. Eriksson, D. Anderson, M. Lisak, and F. Andersson, "Runaway electrons and the evolution of the plasma current in tokamak disruptions", Phys. Plasmas **13**, 10.1063/1.2358110 (2006).

[21] V. Plyusnin et al., "Study of runaway electron generation during major disruptions in JET", Nuclear Fusion **46**, 277–284 (2006).

[22] A. Loarte et al., "Progress on the application of ELM control schemes to ITER scenarios from the non-active phase to DT operation", Nuclear Fusion **54**, 033007 (2014).

[23]F. Wagner et al., "Regime of improved confinement and high beta in neutral-beam-heated divertor discharges of the ASDEX tokamak", Phys. Rev. Lett. **49**, 1408–1412 (1982).

[24]R. J. Groebner, "An emerging understanding of H-mode discharges in tokamaks", Phys. Fluids B **5**, 2343–2354 (1993).

[25]R. D. Stambaugh et al., "Enhanced confinement in tokamaks", Phys. Fluids B **2**, 2941–2960 (1990).

[26]E. J. Doyle et al., "Chapter 2: Plasma confinement and transport", Nucl. Fusion **47**, S18–S127 (2007).

[27]A Loarte et al., "Chapter 4: power and particle control", Nuclear Fusion **47**, S203–S263 (2007).

[28]P. B. Snyder et al., "Edge localized modes and the pedestal: A model based on coupled peeling-ballooning modes", Phys. Plasmas **9**, 2037–2043 (2002).

[29]M. Nave et al., "An overview of MHD activity at the termination of JET hot ion h modes", Nuclear Fusion **37**, 809–824 (1997).

[30]L. Baylor, P. Parks, T. Jernigan, J. Caughman, S. Combs, C. Foust, W. Houlberg, S Maruyama, and D. Rasmussen, "Pellet fuelling and control of burning plasmas in ITER", Nuclear Fusion **47**, 443–448 (2007).

[31]T. E. Evans, "ELM mitigation techniques", J. Nucl. Mater. **438**, S11–S18 (2013).

[32]Y. Liang et al., "Active control of type-I edge-localized modes with n=1 perturbation fields in the JET tokamak", Phys. Rev. Lett. **98**, 10.1103/PhysRevLett.98.265004 (2007).

[33]W. Suttrop et al., "Studies of edge localized mode mitigation with new active in-vessel saddle coils in ASDEX Upgrade", Plasma Phys. Control. Fusion **53**, 124014 (2011).

[34]A. Kirk et al., "Resonant magnetic perturbation experiments on MAST using external and internal coils for ELM control", Nucl. Fusion **50**, 034008 (2010).

[35]N. Oyama, "Progress and issues in understanding the physics of ELM dynamics, ELM mitigation, and ELM control", J. Phys. Conf. Ser. **123**, 012002 (2008).

[36]Y. Liang et al., "Overview of ELM control by low n magnetic perturbations on JET", 36th EPS Conf. Plasma Phys. 2009, EPS 2009 - Europhys. Conf. Abstr. **33 E1**, 166–169 (2009).

[37]T. E. Evans et al., "Edge stability and transport control with resonant magnetic perturbations in collisionless tokamak plasmas", Nat. Phys. **2**, 419–423 (2006).

[38]T. E. Evans et al., "Suppression of Large Edge-Localized Modes in High-Confinement", Phys. Rev. Lett. **92**, 235003 (2004).

[39]O. Schmitz et al., "Aspects of three dimensional transport for ELM control experiments in ITER-similar shape plasmas at low collisionality in DIII-D", Plasma Phys. Control. Fusion **50**, 124029 (2008).

[40]Y. M. Jeon et al., "Suppression of edge localized modes in high-confinement KSTAR plasmas by nonaxisymmetric magnetic perturbations", Phys. Rev. Lett. **109**, 10.1103/PhysRevLett.109.035004 (2012).

[41]K. H. Burrell et al., "Quiescent h-mode plasmas in the DIII-d tokamak", Plasma Physics and Controlled Fusion **44**, A253–A263 (2002).

[42]D. Whyte et al., "I-mode: an h-mode energy confinement regime with l-mode particle transport in alcator c-mod", Nuclear Fusion **50**, 105005 (2010).

[43]M. Greenwald et al., "Characterization of enhanced d-alpha high-confinement modes in alcator c-mod", Physics of Plasmas **6**, 1943–1949 (1999).

[44]H. Zohm, "Dynamic behavior of the L-H transition", Phys. Rev. Lett. **72**, 222–225 (1994).

[45]H Sugama and W Horton, "L-h confinement mode dynamics in three-dimensional state space", Plasma Physics and Controlled Fusion **37**, 345–362 (1995).

[46]H. R. Wilson, P. B. Snyder, G. T. A. Huysmans, and R. L. Miller, "Numerical studies of edge localized instabilities in tokamaks", Physics of Plasmas **9**, 1277–1286 (2002).

[47]C. C. Hegna, J. W. Connor, R. J. Hastie, and H. R. Wilson, "Toroidal coupling of ideal magnetohydrodynamic instabilities in tokamak plasmas", Physics of Plasmas **3**, 584–592 (1996).

[48]H. R. Wilson, J. W. Connor, A. R. Field, S. J. Fielding, R. L. Miller, L. L. Lao, J. R. Ferron, and A. D. Turnbull, "Ideal magnetohydrodynamic stability of the tokamak high-confinement-mode edge region", Phys. Plasmas **6**, 1925–1934 (1999).

[49]T. H. Osborne et al., "The effect of plasma shape on h-mode pedestal characteristics on DIII-d", Plasma Physics and Controlled Fusion **42**, A175–A184 (2000).

[50]J. R. Ferron et al., "Modification of high mode pedestal instabilities in the diii-d tokamak", Physics of Plasmas **7**, 1976–1983 (2000).

[51]E. A. Frieman, J. M. Greene, J. L. Johnson, and K. E. Weimer, "Toroidal effects on magnetohydrodynamic modes in tokamaks", The Physics of Fluids **16**, 1108–1125 (1973).

[52]D. Lortz, "The general "peeling" instability", Nuclear Fusion **15**, 49–54 (1975).

[53]J. W. Connor, R. J. Hastie, H. R. Wilson, and R. L. Miller, "Magnetohydrodynamic stability of tokamak edge plasmas", Phys. Plasmas **5**, 2687–2700 (1998).

[54]C. Mercier, "A necessary condition for hydromagnetic stability of plasma with axial symmetry", Nuclear Fusion **1**, 47–53 (1960).

[55]P. B. Snyder, R. J. Groebner, J. W. Hughes, T. H. Osborne, M. Beurskens, A. W. Leonard, H. R. Wilson, and X. Q. Xu, "A first-principles predictive model of the pedestal height and width: Development, testing and ITER optimization with the EPED model", Nucl. Fusion **51**, 10.1088/0029-5515/51/10/103016 (2011).

[56]P. B. Snyder et al., "The eped pedestal model and edge localized mode-suppressed regimes: studies of quiescent h-mode and development of a model for edge localized mode suppression via resonant magnetic perturbations", Physics of Plasmas **19**, 056115 (2012).

[57]P. B. Snyder et al., "Super H-mode: Theoretical prediction and initial observations of a new high performance regime for tokamak operation", Nucl. Fusion **55**, 10.1088/0029-5515/55/8/083026 (2015).

[58]G. Rewoldt, W. M. Tang, and R. J. Hastie, "Collisional effects on kinetic electromagnetic modes and associated quasilinear transport", The Physics of Fluids **30**, 807–817 (1987).

[59]P. B. Snyder and G. W. Hammett, "Electromagnetic effects on plasma microturbulence and transport", Physics of Plasmas **8**, 744–749 (2001).

[60]T. E. Evans et al., "Experiments to test an intra-island scoop limiter on TEXT", J. Nucl. Mater. **145-147**, 812–818 (1987).

[61]N. Ohyabu, J. S. DeGrassie, and T. E. Evans, "Model for divertor function in H-mode onset and proposal for H-mode operation with the island divertor", J. Nucl. Mater. **145-147**, 844–848 (1987).

[62]T. E. Evans et al., "Resonant helical divertor experiments in ohmic and auxiliary heated JIPP T-IIU plasmas", J. Nucl. Mater. **162-164**, 636–642 (1989).

[63]T. E. Evans, M. Goniche, A. Grosman, D. Guilhem, W. Hess, and J. C. Vallet, "Magnetic perturbation effects on boundary plasmas during high power lower hybrid current drive in Tore Supra", J. Nucl. Mater. **196-198**, 421–425 (1992).

[64]K. H. Finken et al., "Improved confinement due to open ergodic field lines imposed by the dynamic ergodic divertor in TEXTOR", Phys. Rev. Lett. **98**, 10.1103/PhysRevLett.98.065001 (2007).

[65]K. McCormick et al., "Island divertor experiments on the Wendelstein 7-AS stellarator", J. Nucl. Mater. **313-316**, 1131–1140 (2003).

[66]T. E. Evans, *Measurements of poloidal and toroidal energy deposition asymmetries in the ASDEX divertors, Max-Planck-Institut für Plasmaphysik, Garching, IPP III/154*, 1991.

[67]Y. Liu et al., "ELM control with RMP: Plasma response models and the role of edge peeling response", Plasma Phys. Control. Fusion **58**, 114005 (2016).

[68]D. A. Ryan et al., "Toroidal modelling of resonant magnetic perturbations response in ASDEX-Upgrade: Coupling between field pitch aligned response and kink amplification", Plasma Phys. Control. Fusion **57**, 095008 (2015).

[69]A. Wingen, T. E. Evans, and K. H. Spatschek, "High resolution numerical studies of separatrix splitting due to non-axisymmetric perturbation in DIII-D", Nucl. Fusion **49**, 055027 (2009).

[70]C. Paz-Soldan et al., "Observation of a multimode plasma response and its relationship to density pumpout and edge-localized mode suppression", Phys. Rev. Lett. **114**, 10.1103/PhysRevLett.114.105001 (2015).

[71]I. T. Chapman, A. Kirk, S. Saarelma, J. R. Harrison, and R. Scannell, "Towards understanding ELM mitigation: The effect of axisymmetric lobe structures near the X-point on ELM stability", Nucl. Fusion **52**, 10.1088/0029-5515/52/12/123006 (2012).

[72]Y. Liu, A. Kirk, Y. Gribov, M. P. Gryaznevich, T. C. Hender, and E. Nardon, "Modelling of plasma response to resonant magnetic perturbation fields in MAST and ITER", Nucl. Fusion **51**, 83002–83015 (2011).

[73]A. Kirk et al., "Understanding edge-localized mode mitigation by resonant magnetic perturbations on MAST", Nucl. Fusion **53**, 10.1088/0029-5515/53/4/043007 (2013).

[74]A. Kirk et al., "Effect of resonant magnetic perturbations on low collisionality discharges in MAST and a comparison with ASDEX Upgrade", Nucl. Fusion **55**, 043011 (2015).

[75]M. Garcia-Munoz et al., "Fast-ion losses induced by ELMs and externally applied magnetic perturbations in the ASDEX Upgrade tokamak", Plasma Phys. Control. Fusion **55**, 124014 (2013).

[76]L. Schmitz et al., "Reduced electron thermal transport in low collisionality h-mode plasmas in DIII-d and the importance of TEM/ETG-scale turbulence", Nuclear Fusion **52**, 023003 (2012).

[77]W. Suttrop et al., "Mitigation of edge localised modes with magnetic perturbations in ASDEX Upgrade", Fusion Eng. Des. **88**, 446–453 (2013).

[78]L. Li et al., "Modelling plasma response to RMP fields in ASDEX Upgrade with varying edge safety factor and triangularity", Nucl. Fusion **56**, 126007 (2016).

[79]T. Shoji et al., "Effects of ergodization on plasma confinement in JFT-2M", J. Nucl. Mater. **196-198**, 296–300 (1992).

[80]T. E. Evans et al., "RMP ELM suppression in DIII-D plasmas with ITER similar shapes and collisionalities", Nucl. Fusion **48**, 24002–24012 (2008).

[81]T. M. Bird and C. C. Hegna, "A model for microinstability destabilization and enhanced transport in the presence of shielded 3D magnetic perturbations", Nucl. Fusion **53**, 10.1088/0029-5515/53/1/013004 (2013).

[82]Y. Liu et al., "Toroidal modelling of RMP response in ASDEX Upgrade: Coil phase scan, q 95 dependence, and toroidal torques", Nucl. Fusion **56**, 056015 (2016).

[83]M. Willensdorfer et al., "Plasma response measurements of external magnetic perturbations using electron cyclotron emission and comparisons to 3D ideal MHD equilibrium", Plasma Phys. Control. Fusion **58**, 10.1088/0741-3335/58/11/114004 (2016).

[84]M. Willensdorfer et al., "Three dimensional boundary displacement due to stable ideal kink modes excited by external n = 2 magnetic perturbations", Nucl. Fusion **57**, 10.1088/1741-4326/aa7f4c (2017).

[85]T. B. Cote, C. C. Hegna, M. Willensdorfer, E. Strumberger, W. Suttrop, and H. Zohm, "Helically localized ballooning instabilities in three-dimensional tokamak pedestals", Nucl. Fusion **59**, 10.1088/1741-4326/aaf01d (2019).

[86]"First observation of edge localized modes mitigation with resonant and nonresonant magnetic perturbations in ASDEX upgrade", Phys. Rev. Lett. **106**, 225004 (2011).

[87]Y. Liang et al., "Mitigation of type-I ELMs with n = 2 fields on JET with ITER-like wall", Nucl. Fusion **53**, 10.1088/0029-5515/53/7/073036 (2013).

[88]M. E. Fenstermacher et al., "Effect of island overlap on edge localized mode suppression by resonant magnetic perturbations in DIII-D", Phys. Plasmas **15**, 56122 (2008).

[89]J. Kim et al., "ELM control experiments in the KSTAR device", Nucl. Fusion **52**, 114011 (2012).

[90]Y. Sun et al., "Nonlinear Transition from Mitigation to Suppression of the Edge Localized Mode with Resonant Magnetic Perturbations in the EAST Tokamak", Phys. Rev. Lett. **117**, 10.1103/PhysRevLett.117.115001 (2016).

[91]W. Suttrop et al., "Experimental conditions for suppressing Edge Localised Modes by magnetic perturbations in ASDEX Upgrade", 45th EPS Conf. Plasma Physics, EPS 2018 **2018-July**, 25–28 (2018).

[92]R. Nazikian, W. Suttrop, A. Kirk, D. M. Orlov, C. Paz-Soldan, M. Willensdorfer, R. M. McDermott, and T. E. Evans, *First Observation of ELM Suppression in ASDEX-Upgrade In A Similarity Experiment With DIII-D*, tech. rep. (2016), PD/1–1.

[93]R. Nazikian et al., "Pedestal bifurcation and resonant field penetration at the threshold of edge-localized mode suppression in the DIII-d tokamak", Phys. Rev. Lett. **114**, 10.1103/PhysRevLett.114.105002 (2015).

[94]G. R. McKee et al., "Increase of turbulence and transport with resonant magnetic perturbations in ELM-suppressed plasmas on DIII-D", Nucl. Fusion **53**, 113011 (2013).

[95]J. D. Callen, C. C. Hegna, and A. J. Cole, "Magnetic-flutter-induced pedestal plasma transport", Nucl. Fusion **53**, 10.1088/0029-5515/53/11/113015 (2013).

Chapter 3

Review of MHD Theory

3.1 Ideal Magnetohydrodynamics

Ideal magnetohydrodynamics (MHD) is one of the simplest models for describing both the macroscopic equilibrium and stability properties of a plasma. MHD provides a single-fluid description of macroscopic plasma behavior at long-wavelength and low-frequency. This discussion of the ideal MHD model in this section is largely a summary of References [1] and [2], which provide a much more in-depth look into the theory than what is presented here.

The ideal MHD model considers the plasma to be a single-species conducting fluid, with a collective, fluid-like behavior that can be described by coupling the fluid equations of motion with Maxwell's equations. In doing so, we are left with a nonlinear system of partial

differential equations, given by [1]

$$\text{Mass :} \quad \frac{\partial \rho}{\partial t} + \nabla \cdot \rho \mathbf{v} = 0, \tag{3.1}$$

$$\text{Momentum :} \quad \rho \frac{d\mathbf{v}}{dt} = \mathbf{J} \times \mathbf{B} - \nabla p, \tag{3.2}$$

$$\text{Energy :} \quad \frac{d}{dt}\left(\frac{p}{\rho^{\gamma}}\right) = 0 \tag{3.3}$$

$$\text{Ohm's Law :} \quad \mathbf{E} + \mathbf{v} \times \mathbf{B} = 0 \tag{3.4}$$

$$\text{Maxwell :} \quad \nabla \times \mathbf{E} = -\frac{\partial \mathbf{B}}{\partial t} \tag{3.5}$$

$$\nabla \times \mathbf{B} = \mu_0 \mathbf{J} \tag{3.6}$$

$$\nabla \cdot \mathbf{B} = 0 \tag{3.7}$$

where the fluid variables are the mass density ρ, the single-fluid velocity $\mathbf{v}$, and the pressure p, with the specific heat ratio $\gamma = 5/3$. The electromagnetic variables are the electric field $\mathbf{E}$, the magnetic field $\mathbf{B}$, and the current density $\mathbf{J}$.

The above system of equations make use of MHD fluid equations to describe the time evolution of the mass, momentum, and energy, while using the low-frequency, pre-Maxwell equations to describe the electromagnetic behavior. The system is closed with the ideal MHD Ohm's Law, which assumes the plasma to be perfectly conducting and the electric field to be zero in the reference frame of the moving plasma.

The MHD model describes the low frequency, long wavelength, macroscopic behavior of the plasma. Thus, the characteristic length and timescales of MHD phenomena are related to the overall radial dimension of the plasma, given by the minor radius a, and the characteristic plasma speed, given by the thermal ion velocity, $V_{T_i} = (2T_i/m_i)^{1/2}$, leading to an MHD timescale $\tau_{MHD} \sim a/V_{T_i}$. Using a minor radius $a \sim 1m$, the mass of deuterium for m_i, and $T_i = 3\ keV$, the characteristic time for ideal MHD is $\tau_{MHD} \sim 2\mu s$.

A second characteristic timescale is the Alfvén time, which corresponds to the time it takes MHD waves to propagate from the center of the plasma to its edge, and its inverse indicates

the maximum rate of large scale plasma motion. The Alfvén time is defined as

$$\tau_A = \frac{a}{v_A} \qquad v_a^2 = \frac{B^2}{\mu_0 \rho} \tag{3.8}$$

where a is again the minor radius of the plasma, B is the magnetic field (typically the on-axis value of the toroidal field, B_0), and $\rho = n_i m_i$ is the ion mass density. While the Alfvén time varies significantly between plasma devices, typical tokamaks have $\tau_A \sim 10^{-7} - 10^{-8}\ s$, with $T_i = 3\ keV$ and $n_i = 10^{20} m^{-3}$.

3.1.1 Ideal MHD Equilibrium Theory

MHD equilibrium theory, which consists of finding plasma configurations that are in force-balance, is an essential component to studying fusion plasma systems. The primary goals of the equilibrium is to find a magnetic geometry that confines the plasma within a specific "magnetic bottle", protecting the walls of the vacuum vessel, and to confine the plasma for a sufficient amount of time to reach fusion relevant conditions. The concept of plasma confinement in steady state systems is in contrast to that of plasma stability, which focuses on identifying sources of free energy that trigger transient events causing the plasma to evolve to a new equilibrium state or terminate completely. The topic of plasma stability is discussed in the following section, while this section focuses on plasma confinement in steady state systems.

The ideal MHD equilibrium equations are derived from the ideal MHD model by assuming a steady state condition (i.e. $\partial / \partial t \rightarrow 0$). Additionally, it is often assumed that the plasma is static (i.e. no equilibrium flow $\mathbf{v} = 0$), though there are additional models that include the

flow. The static, steady state equilibrium equations are given by [1]

$$\mathbf{J} \times \mathbf{B} = \nabla p \tag{3.9}$$

$$\nabla \times \mathbf{B} = \mu_0 \mathbf{J} \tag{3.10}$$

$$\nabla \cdot \mathbf{B} = 0 \tag{3.11}$$

At its core, ideal MHD equilibrium theory comes down to a basic force balance between the outward pressure gradient and the confining magnetic fields. Solutions to 3.9 imply that the surfaces of constant p are described by tori in a volume where $\nabla p \neq 0$[3]. For these systems, the field lines wind around the surfaces of constant pressure until they either close in on themselves after a finite number of revolutions or ergodically fill the surface. As discussed in section 2.2.1, these surfaces can be described in terms of the magnetic flux function ψ_p proportional to the magnetic flux within the surface[4]

$$\psi_p \equiv \int \mathbf{B} \cdot d\mathbf{S}_p \tag{3.12}$$

As the flux functions are also constant on the surfaces, it is typical to recast the pressure as a flux function, $p = p(\psi)$.

There is a special case solution to equation 3.9 when the pressure gradient goes to zero ($\nabla p = 0$), resulting in equilibria unconstrained to toroidal surfaces such that the field lines are able to stochastically fill a finite volume. This scenario is not considered here, as the resulting configurations tend to have poor plasma confinement properties.

For axisymmetric plasma configurations, the complexity of the equilibrium calculations are simplified by introducing a directional invariant such that the dimensionality of the problem is reduced by one. By imposing toroidal invariance ($\partial/\partial\phi \rightarrow 0$), equations 3.9-3.11 can be simplified in the cylindrical coordinate system (R, ϕ, Z), resulting in the Grad-Shafranov equation[5, 6]. The Grad-Shafranov equation is a second-order nonlinear elliptic equation

given by[1]

$$\Delta^* \psi = -\mu_0 R^2 \frac{\partial p}{\partial \psi} - F \frac{\partial F}{\partial \psi} \tag{3.13}$$

where Δ^* is the elliptical differential operator

$$\Delta^* \psi \equiv R^2 \nabla \cdot \left(\frac{\nabla \psi}{R^2} \right) = \frac{\partial^2 \psi}{\partial Z^2} + R \frac{\partial}{\partial R} \left(\frac{1}{R} \frac{\partial \psi}{\partial R} \right) \tag{3.14}$$

and the flux function F is defined as

$$F(\psi) = R B_\phi. \tag{3.15}$$

The behavior of the equilibrium is largely determined by the choice of the free functions $p(\psi)$ and $F(\psi)$ along with the appropriate boundary conditions for the system. Once the functional form of ψ has been determined, the corresponding magnetic fields and current density are determined by

$$\mathbf{B} = \frac{1}{R} \nabla \psi \times \mathbf{e}_\phi + \frac{F}{R} \mathbf{e}_\phi \tag{3.16}$$

$$\mu_0 \mathbf{J} = \frac{1}{R} \frac{\mathrm{d}F}{\mathrm{d}\psi} \nabla \psi \times \mathbf{e}_\phi - \frac{1}{R} \Delta^* \psi \mathbf{e}_\phi \tag{3.17}$$

As such, the Grad-Shafranov equation provides a complete description of radial pressure and toroidal force balance in the plasma.

3.1.2 Ideal MHD Stability Theory

The investigation of linear ideal MHD stability centers around the idea of making small perturbations from the plasma equilibrium state and observing if the plasma returns to equilibrium (which we call a stable equilibrium) or moves away from the equilibrium (unstable equilibrium). To do this, it is assumed that all MHD quantities can be linearized about their equilibrium values as

$$Q(\mathbf{r}, t) = Q_0(\mathbf{r}) + \tilde{Q}_1(\mathbf{r}, t) \tag{3.18}$$

where $Q_0(\mathbf{r})$ is the zeroth-order equilibrium value and $\tilde{Q}_1(\mathbf{r},t)$ is a small higher-order perturbation such that $|\tilde{Q}_1(\mathbf{r},t)/Q_0(\mathbf{r})| \ll 1$. Next, since the equilibrium is time independent, the perturbation can be defined as

$$\tilde{Q}_1(\mathbf{r},t) = Q_1(\mathbf{r})e^{-i\omega t} \tag{3.19}$$

where ω is the mode frequency to be determined. In most systems, the definition of MHD stability is given by the "exponential stability," that is systems with $\mathrm{Im}(\omega) > 0$ result in exponential growth and are thus unstable, while systems with $\mathrm{Im}(\omega) \leq 0$ are stable.

In order to determine the eigenvalue of a system, it is necessary to linearize the ideal MHD equations making use of the assumptions above. Doing so, the conservation of mass, conservation of energy, and Faraday's law reduce down to

$$\rho_1 = -\nabla \cdot \left(\rho_0 \bar{\xi}\right) \tag{3.20}$$

$$p_1 = -\bar{\xi} \cdot \nabla p_0 - \gamma p_0 \nabla \cdot \bar{\xi} \tag{3.21}$$

$$\mathbf{B}_1 = \nabla \times \left(\bar{\xi} \times \mathbf{B}_0\right) \tag{3.22}$$

where $\bar{\xi}$ is the displacement of the plasma away from its equilibrium position, given by

$$\mathbf{v}_1 = \frac{\partial \bar{\xi}}{\partial t}. \tag{3.23}$$

Substituting the above relations into the momentum equation and applying the normal mode approximation gives

$$-\omega^2 \rho \bar{\xi} = \mathbf{F}\left(\bar{\xi}\right) \tag{3.24}$$

where

$$\mathbf{F}\left(\bar{\xi}\right) = \frac{1}{\mu_0}\left(\nabla \times \mathbf{B}_0\right) \times \mathbf{B}_1 + \frac{1}{\mu_0}\left(\nabla \times \mathbf{B}_1\right) \times \mathbf{B}_0 - \nabla p_1 \tag{3.25}$$

is the linear ideal force operator. Using this formulation, the eigenvalue ω^2 is determined solving equation 3.24 for a given set of boundary conditions on $\bar{\xi}$.

The force operator $\mathbf{F}\left(\bar{\xi}\right)$ is self-adjoint[1], which results in the eigenvalues ω^2 being purely real. This simplifies the stability analysis as the transition point ($\mathrm{Im}(\omega) = 0$) occurs only when ω^2 crosses zero. This simplification leads to an efficient formulation for testing linear stability known as the Energy Principle. Additionally, the self-adjointness of $\mathbf{F}$ leads to the unstable normal modes being both orthogonal and discrete. This further simplifies the stability problem, as the plasma perturbation will always be dominated by the single fastest growing linear mode (as opposed to a combination of modes), reducing the stability problem to finding only the fastest growing normal mode.

The property of self-adjointness can be defined for any two arbitrary vectors $\bar{\xi}(\mathbf{r})$ and $\bar{\eta}(\mathbf{r})$ such that both satisfy the relation

$$\int \bar{\eta} \cdot \mathbf{F}\left(\bar{\xi}\right) d\mathbf{r} = \int \bar{\xi} \cdot \mathbf{F}\left(\bar{\eta}\right) d\mathbf{r} \tag{3.26}$$

as well satisfying any boundary conditions. The starting point for the Energy Principle is the left-hand side of this equation. Defining the factor δW as

$$\delta W\left(\bar{\eta}, \bar{\xi}\right) = -\frac{1}{2} \int \bar{\eta} \cdot \mathbf{F}\left(\bar{\xi}\right) d\mathbf{r} \tag{3.27}$$

where the factor of $-1/2$ is added such that $\delta W\left(\bar{\xi}^*, \bar{\xi}\right)$ is equal to a physically relevant quantity, the perturbed potential energy of the plasma. Making use of previous definitions, dropping the zero subscript for equilibrium terms, and introducing $\bar{\xi} = \bar{\xi}_\perp + \xi_\parallel \mathbf{b}$, δW can be expressed as

$$\delta W\left(\bar{\eta}, \bar{\xi}\right) = \delta W_F + BT \tag{3.28}$$

where the fluid energy (volume term) is

$$\delta W_F = \frac{1}{2} \int \left[\frac{1}{\mu_0} \mathbf{B}_1\left(\bar{\eta}_\perp\right) \cdot \mathbf{B}_1\left(\bar{\xi}_\perp\right) + \gamma p \left(\nabla \cdot \bar{\eta}\right)\left(\nabla \cdot \bar{\xi}\right) - \bar{\eta}_\perp \cdot \mathbf{J} \times \mathbf{B}_1\left(\bar{\xi}_\perp\right) + \left(\bar{\xi}_\perp \cdot \nabla p\right) \nabla \cdot \bar{\eta}_\perp \right] d\mathbf{r} \tag{3.29}$$

and the surface term arising from the use of Gauss' theorem in the integration by parts is

$$BT = \frac{1}{2}\int (\mathbf{n}\cdot\bar{\eta}_\perp)\left[\frac{1}{\mu_0}\mathbf{B}\cdot\mathbf{B}_1\left(\bar{\xi}_\perp\right) - \gamma p\nabla\cdot\bar{\xi} + \bar{\xi}_\perp\cdot\nabla p\right] dS \tag{3.30}$$

The boundary term contains exactly the right terms to account for the vacuum region surrounding the plasma, but can be simplified to zero by assuming the plasma is surrounded by a perfectly conducting wall.

The above expression is known as the "standard form" of δW, but is not the most useful for stability analysis. The next step in stability analysis is to covert to the so-called "intuitive form" of δW, which is better suited to provide physical insight into the nature of MHD instabilities. The first step in this transformation is to define the parallel and perpendicular components of the perturbed magnetic field as

$$\mathbf{B}_1\left(\bar{\xi}_\perp\right) = \left[\mathbf{b}\times\nabla\times\left(\bar{\xi}_\perp\times\mathbf{B}\right)\right]\times\mathbf{b} + \left[\mathbf{b}\cdot\nabla\times\left(\bar{\xi}_\perp\times\mathbf{B}\right)\right]\mathbf{b} \tag{3.31}$$

$$= \mathbf{Q}_\perp\left(\bar{\xi}_\perp\right) + \mathbf{Q}_\parallel\left(\bar{\xi}_\perp\right) = \mathbf{Q}\left(\bar{\xi}_\perp\right) \tag{3.32}$$

Making use of this relation, simplifying, and rearranging, the δW equation can be expressed in its "intuitive form" [7–9]

$$\begin{aligned}\delta W_F = \frac{1}{2\mu_0}\int \Big[&\mathbf{Q}_\perp\left(\bar{\eta}_\perp\right)\cdot\mathbf{Q}_\perp\left(\bar{\xi}_\perp\right) + B^2\left(\nabla\cdot\bar{\eta}_\perp + 2\bar{\eta}_\perp\cdot\bar{\kappa}\right)\left(\nabla\cdot\bar{\xi}_\perp + 2\bar{\xi}_\perp\cdot\bar{\kappa}\right)\\ &+\mu_0\gamma p\left(\nabla\cdot\bar{\eta}\right)\left(\nabla\cdot\bar{\xi}\right) - 2\mu_0\left(\bar{\xi}_\perp\cdot\nabla p\right)\left(\bar{\eta}_\perp\cdot\bar{\kappa}\right) - \mu_0 J_\parallel\bar{\eta}_\perp\times\mathbf{b}\cdot\mathbf{Q}_\perp\Big]\, d\mathbf{r}\end{aligned} \tag{3.33}$$

where $\bar{\kappa} = \mathbf{b}\cdot\nabla\mathbf{b}$ is the magnetic curvature vector. The intuitive nature of this form is best seen when choosing the arbitrary vector $\bar{\eta} = \bar{\xi}^*$ relating δW to the potential energy, in which the above reduces to

$$\begin{aligned}\delta W_F = \frac{1}{2\mu_0}\int \Big[&\left|\mathbf{Q}_\perp\right|^2 + B^2\left|\nabla\cdot\bar{\xi}_\perp + 2\bar{\xi}_\perp\cdot\bar{\kappa}\right|^2 + \mu_0\gamma p\left|\nabla\cdot\bar{\xi}\right|^2\\ &-2\mu_0\left(\bar{\xi}_\perp\cdot\nabla p\right)\left(\bar{\xi}^*_\perp\cdot\bar{\kappa}\right) - \mu_0 J_\parallel\bar{\xi}^*_\perp\times\mathbf{b}\cdot\mathbf{Q}_\perp\left(\bar{\xi}_\perp\right)\Big]\, d\mathbf{r}\end{aligned} \tag{3.34}$$

The first three terms presented above are positive definite, meaning their contributions are purely stabilizing. The $|\mathbf{Q}_\perp|^2$ term represents the magnetic energy necessary to bend the magnetic field lines, which leads to shear Alfven waves for homogeneous magnetic fields. The $B^2\left|\nabla\cdot\bar{\xi}_\perp+2\bar{\xi}_\perp\cdot\bar{\kappa}\right|^2$ and $\mu_0\gamma p\left|\nabla\cdot\bar{\xi}\right|^2$ terms are the magnetic field and plasma compression terms, respectively. These terms generate the magnetosonic waves (compressional Alfven waves and sound waves, respectively) in a homogeneous magnetic field. The last two terms can be positive or negative; negative values correspond to drives for plasma instabilities. The $2\mu_0\left(\bar{\xi}_\perp\cdot\nabla p\right)\left(\bar{\xi}_\perp^*\cdot\bar{\kappa}\right)$ term is responsible for pressure-curvature driven instabilities, while the $\mu_0 J_\parallel\bar{\xi}_\perp^*\times\mathbf{b}\cdot\mathbf{Q}_\perp\left(\bar{\xi}_\perp\right)$ term results in current driven instabilities. These two terms are critical in the work presented here, and will be discussed in detail in the forthcoming sections.

In order to simplify the stability calculations, it is worth introducing a variational formulation that is mathematically equivalent to the integral representation of the linearized MHD system discussed here [10]. Making use of the self-adjointness of the force operator, we can define the variational form

$$\omega^2=\frac{\delta W\left(\bar{\xi}^*,\bar{\xi}\right)}{K\left(\bar{\xi}^*,\bar{\xi}\right)} \tag{3.35}$$

where

$$\delta W\left(\bar{\xi}^*,\bar{\xi}\right)=-\frac{1}{2}\int\bar{\xi}^*\cdot\mathbf{F}\left(\bar{\xi}\right)d\mathbf{r} \tag{3.36}$$

$$K\left(\bar{\xi}^*,\bar{\xi}\right)=\frac{1}{2}\int\rho\left|\bar{\xi}\right|d\mathbf{r} \tag{3.37}$$

Here, $\delta W\left(\bar{\xi}^*,\bar{\xi}\right)$ is proportional to the potential energy of the plasma, while $\omega^2K\left(\bar{\xi}^*,\bar{\xi}\right)$ is proportional to the kinetic energy of the plasma. Using these equations, the variational principle states that any trial function $\bar{\xi}$ that produces an extremum in ω^2 is an eigenfunction with the eigenvalue given by equation 3.35.

This leads to the fundamental tool for determining plasma stability: the Energy Principle. The Energy Principle states that an equilibrium is stable if and only if

$$\delta W\left(\bar{\xi}^*, \bar{\xi}\right) \geq 0 \tag{3.38}$$

for all allowable trial displacements. Based on this, if any trial displacements lead to a negative δW, the equilibrium is unstable. This reduces the stability problem to finding any eigenfunctions that lead to instability, which is posed as a minimization problem with respect to the eigenfunction.

To this point, the Energy Principle has assumed a close fitting conducting wall to eliminate the surface term contributions. However, the most dangerous MHD instabilities occur for perturbations that move the plasma surface away from its equilibrium position. In order to accurately studies these instabilities, it is necessary to include the surface contributions to δW, leading to the "Extended Energy Principle" formulation. Inclusion of the boundary term from equation 3.28 introduces a surface potential δW_S and vacuum potential δW_V such that the potential energy of the system becomes

$$\delta W = \delta W_F + \delta W_S + \delta W_V \tag{3.39}$$

The surface energy term is given by

$$\delta W_S\left(\bar{\xi}^*, \bar{\xi}\right) = \frac{1}{2\mu_0} \int_{S_p} \left|\mathbf{n} \cdot \bar{\xi}_\perp\right|^2 \mathbf{n} \cdot \left[\!\left[\nabla\left(\frac{B^2}{2} + \mu_0 p\right)\right]\!\right] dS \tag{3.40}$$

where the $\mathbf{n} \cdot [\![\mathbf{X}]\!]$ corresponds to the jump in $\mathbf{X}$ across the surface normal. The vacuum energy term is given by

$$\delta W_V\left(\bar{\xi}^*, \bar{\xi}\right) = \frac{1}{2\mu_0} \int_V \left|\hat{\mathbf{B}}_1\right|^2 d\mathbf{r} \tag{3.41}$$

This creates a complete model for the potential energy of an equilibrium state, which can

be minimized in the same was as the standard Energy Principle to determine the stability of systems with a complete vacuum region.

In this thesis we make use of the normal mode analysis, the Standard Energy Principle, and the Extended Energy Principle to determine the stability of equilibrium to specific types of instabilities, which will be discussed in subsequent sections.

3.1.3 Overview of Ideal MHD Instabilities

Before moving to the specific instabilities of interest to this thesis, it is important to define general types of instabilities and their properties. Ideal MHD instabilities are classified by their general structure as well as the free-energy source driving them. Structurally, instabilities fall into two categories: internal or external modes. Internal (or fixed boundary) modes are instabilities whose mode structure does not perturb the plasma boundary. These instabilities often occur at isolated internal surfaces, and lead to boundary conditions such as $\left[\mathbf{n}\cdot\bar{\xi}_{\perp}\right]_{S_p}=0$ which is equivalent to the conducting wall limit with $\delta W_S=\delta W_V=0$. In contrast, external (or free boundary) modes involve perturbation of the plasma-vacuum interface. For these instabilities, δW_S and δW_V must be included as the surface term $\left[\mathbf{n}\cdot\bar{\xi}_{\perp}\right]_{S_p}$ is non-zero.

For the dominant driving source, instabilities are either pressure-driven or current-driven, as seen in the δW formulation. Pressure-driven instabilities arise when the outward pushing pressure gradient force aligns with the magnetic field curvature vector as a source of free energy. The dominant pressure-driven instability in Tokamaks is the ballooning instability, though interchange instabilities can also occur. Ballooning modes are internal instabilities that occur for $k_{\perp}a\gg 1$ and $k_{\parallel}/k_{\perp}\ll 1$, and are the dominant topic of section 4.2. While both ballooning and interchange modes are pressure-curvature driven, the main difference is interchange modes are approximately constant along the field lines (i.e. $k_{\parallel}=0$) to minimize the stabilizing line bending effects, effectively sampling the average field line curvature. Ballooning instabilities are considered a "local" instability, in that it is the local coupling of the pressure with the curvature that is important, and only regions with "bad curvature" will

be unstable. Additionally, magnetic field line geometry becomes important in balancing the local stability, leading to the ballooning structure of the mode.

The driving source behind current-driven instabilities is proportional to the parallel current, $J_{\parallel}$, even in the absence of pressure gradients. Current-driven modes are often referred to as "kink" modes, as they often lead to a kinking-effect of the flux surfaces. In general, the most unstable kink modes occur when $k_{\parallel}a \ll 1$ and $k_{\perp}a \sim 1$, leading to more large scale, global instabilities in comparison to the pressure-driven modes. Current-driven modes can be either internal or external, depending on the system configuration and the location of the rational surface. External kink modes are considered detrimental to tokamak operation, as they often lead to large scale disruption of the plasma causing large amounts of stored energy to leave the confinement region. Internal kink modes are very similar to the external kink, but tend to be weaker. Regardless, they can have large impact on core plasma confinement, as kinks such as the "sawtooth oscillations" can transport stored energy out of the core confinement region.

One specific type of external kink instability is the so-called "peeling" mode[11, 12]. Peeling modes localize at the edge of the plasma when rational surfaces ($q = m/n$) exist just outside the plasma boundary, minimizing the stabilizing effects of vacuum magnetic perturbations[13]. While peeling modes are destabilized by large edge currents, they can be stabilized by increasing the magnetic shear or pressure gradient in the edge.

3.2 Magnetic Coordinates and Geometry in 3D

In the following sections, the linear ballooning, peeling, and peeling-ballooning models will be discussed at length, as they are the primary topics of this thesis. Before continuing with these topics, it is necessary to define the 3D magnetic geometry that will be used in these models, as well as key values related to the magnetic geometry.

3.2.1 Magnetic Coordinate System

For this work we make use of magnetic flux coordinates (ψ, θ, ζ) where $\psi = \Psi_p/2\pi$ is the normalized poloidal flux, ζ is the geometric toroidal angle, and θ is the poloidal coordinate in which the magnetic field lines are straight. Using this system, the magnetic field is given by [4]

$$\mathbf{B} = \nabla\zeta \times \nabla\psi + q(\psi)\nabla\psi \times \nabla\theta \tag{3.42}$$

which, by defining the field line label $\alpha = \zeta - q(\psi)\theta$, can be recast into a Clebsch form in the equivalent (α, ψ, θ) coordinate system as

$$\mathbf{B} = \nabla\alpha \times \nabla\psi. \tag{3.43}$$

These two straight field line coordinate systems have equivalent Jacobians

$$\mathcal{J}(\alpha, \psi, \theta) = (\nabla\alpha \times \nabla\psi \cdot \nabla\theta)^{-1} = (\nabla\psi \times \nabla\theta \cdot \nabla\zeta)^{-1} = \mathcal{J}(\psi, \theta, \zeta) \tag{3.44}$$

allowing the systems to be freely interchanged. The Clebsch form of the magnetic field yields significant analytic advantages, such as simplifying the parallel derivative to

$$\mathbf{B} \cdot \nabla = \frac{1}{\mathcal{J}} \frac{\partial}{\partial\theta} \tag{3.45}$$

implying that the remaining coordinates are orthogonal to the magnetic field ($\mathbf{B} \cdot \nabla\alpha = \mathbf{B} \cdot \nabla\psi = 0$).

3.2.2 Problem Domain

For a given magnetic surface ψ, it is normal to consider a position vector $\mathbf{r}(\theta, \zeta)$ with the domain taken to be the square unit cell

$$D_1 : \quad 0 \leq \theta \leq 2\pi, \quad 0 \leq \zeta \leq 2\pi \tag{3.46}$$

with periodic boundaries at the edges, such that the toroidal magnetic surface has been "unfolded". For ballooning analysis in tokamak geometry, it is useful to analytically continue the function space periodically in θ and ζ to the infinite domain

$$D_\infty : \quad -\infty < \theta < \infty, \quad -\infty < \zeta < \infty \tag{3.47}$$

which is topologically planar ($D_\infty = \mathcal{R}^2$). The position vector $\mathbf{r}(\theta, \zeta)$ defined on the domain D_∞ forms a covering space[14] for the toroidal magnetic surface. Mathematically, this allows for the problem to be solved using the metric of the torus, but on the topology of a slab, allowing access to a wider range of solutions on the covering space. From here, it is possible to construct a general solution over the covering space, from which the physical solutions lie within, using standard functional analysis[14]. By defining the covering space to be a Hilbert space [14], the force operator is Hermitian, insuring square integrable solutions which are periodic on the physical domain.

3.2.3 Important Quantities of the Magnetic Geometry

In addition to the above flux coordinates, it is necessary to establish a set of orthonormal basis vectors to help define different geometric quantities. The logical starting point for these systems is to use the unit vector following the magnetic field line, $\hat{b} = \mathbf{B}/B$. Based on the definition of the magnetic field in equation 3.43, the unit normal vector perpendicular to the field is defined as $\hat{n} = \nabla\psi/|\nabla\psi|$. The third basis vector is trivially obtained by taking the

cross-product of the other vectors, resulting in the geodesic vector (or bi-normal vector), $\hat{g} = \hat{b} \times \hat{n}$. The complete sets of basis vectors

$$\hat{b} = \frac{\mathbf{B}}{B} \qquad \hat{n} = \frac{\nabla\psi}{|\nabla\psi|} \qquad \hat{g} = \frac{\mathbf{B} \times \nabla\psi}{B|\nabla\psi|} \tag{3.48}$$

provide a foundation for defining relevant geometric quantities in 3D.

Using the above basis set, the magnetic curvature is defined as

$$\kappa = \hat{b} \cdot \nabla\hat{b} = \frac{1}{B^2} \cdot \nabla \left(\mu_0 p + \frac{B^2}{2} \right) \tag{3.49}$$

The normal and geodesic components of the curvature are thus

$$\kappa_n = \hat{n} \cdot \kappa \qquad \kappa_g = \hat{g} \cdot \kappa \tag{3.50}$$

The local magnetic shear is defined as

$$s = \left(\hat{b} \times \hat{n} \right) \cdot \nabla \times \left(\hat{b} \times \hat{n} \right) \tag{3.51}$$

but can be written as

$$s = \mu_0 \sigma - 2\tau_n \tag{3.52}$$

where the local current density along the field line is defined as

$$\sigma = \frac{\mathbf{J} \cdot \mathbf{B}}{B^2} = \frac{J_\parallel}{B} \tag{3.53}$$

and the normal torsion, a purely geometric term, is given by

$$\tau_n = -\hat{n} \cdot \left(\hat{b} \cdot \nabla \right) \hat{g} \tag{3.54}$$

3.2.4 Energy Principle

Now that the magnetic coordinate system has been established, it is useful to transform the Energy Principle given by equation 3.34 into the straight field line coordinate system. For the plasma potential energy, it is convenient to define it in an equivalent form

$$\delta W_p\left[\xi\right] = \frac{1}{2}\int_p \mathrm{d}\mathbf{r}\left[\frac{|\bar{\mathbf{Q}}|^2}{\mu_0} + \gamma p|\nabla\cdot\xi|^2 - 2\left(\xi\cdot\nabla p\right)\left(\kappa\cdot\xi^*\right) - \sigma\left(\xi^*\times\mathbf{B}\right)\cdot\bar{\mathbf{Q}}\right] \tag{3.55}$$

where the modified perturbed magnetic field is given by

$$\bar{\mathbf{Q}} = \mathbf{Q} - \mathbf{B}\frac{\mu_0\xi\cdot\nabla p}{B^2} = \mathbf{Q}_\perp - \mathbf{B}\left[\nabla\cdot\xi_\perp + 2\xi_\perp\cdot\kappa\right] \tag{3.56}$$

The first step is to decompose the plasma perturbation ξ and the perturbed magnetic field $\bar{\mathbf{Q}}$ into a normal, geodesic, and parallel component, such that

$$\xi = X\frac{\nabla\psi}{|\nabla\psi|^2} + U\frac{\nabla\psi\times\mathbf{B}}{B^2} + W\mathbf{B} \tag{3.57}$$

and

$$\bar{\mathbf{Q}} = Q_X\frac{\nabla\psi}{|\nabla\psi|^2} + Q_U\frac{\nabla\psi\times\mathbf{B}}{B^2} + Q_W\mathbf{B} \tag{3.58}$$

where

$$\begin{aligned} Q_X &= \left(\mathbf{B}\cdot\nabla\right)X \\ Q_U &= \left(\mathbf{B}\cdot\nabla\right)U + X\left(\mathbf{B}\cdot\nabla\right)\Theta^\alpha \\ Q_W &= -B^2\left[\nabla\cdot\xi_\perp + 2\xi_\perp\cdot\kappa\right] \end{aligned} \tag{3.59}$$

with

$$\Theta^i = \frac{\nabla\psi\cdot\nabla u_i}{\nabla\psi\cdot\nabla\psi} \tag{3.60}$$

All that remains is to calculate the components of the potential in terms of the new coordinate system. Going term-by-term, it is seen that the line-bending term is

$$\frac{1}{2}\int_p \mathrm{d}\mathbf{r}\frac{|\mathbf{Q}_\perp|^2}{\mu_0} = \frac{1}{2}\frac{1}{\mu_0}\int_p \mathrm{d}\mathbf{r}\left(\frac{1}{|\nabla\psi|^2}\left|(\mathbf{B}\cdot\nabla)\,X\right|^2 + \frac{|\nabla\psi|^2}{B^2}\left|(\mathbf{B}\cdot\nabla)\,U + (\mathbf{B}\cdot\nabla)\,\Theta^\alpha\right|^2\right) \tag{3.61}$$

the pressure-curvature term is

$$-\frac{1}{2}\int_p \mathrm{d}\mathbf{r}\,2\left(\xi\cdot\nabla p\right)\left(\kappa\cdot\xi^*\right) = -\frac{1}{2}\int_p \mathrm{d}\mathbf{r}\,2Xp'\left(X^*\kappa_n + U^*\kappa_g\right) \tag{3.62}$$

and the kink-peeling term is

$$-\frac{1}{2}\int_p \mathrm{d}\mathbf{r}\,\sigma\left(\xi^*\times\mathbf{B}\right)\cdot\bar{\mathbf{Q}} = -\frac{1}{2}\int_p \mathrm{d}\mathbf{r}\,\sigma\left[X^*\left((\mathbf{B}\cdot\nabla)\,U + X\,(\mathbf{B}\cdot\nabla)\,\Theta^\alpha\right) - U^*\left((\mathbf{B}\cdot\nabla)\,X\right)\right] \tag{3.63}$$

For the sake of simplicity, the compressional sound wave term $\gamma p|\nabla\cdot\xi|^2$ and the Alfvenic term $B^2\left|\nabla\cdot\xi_\perp + 2\xi_\perp\cdot\kappa\right|^2$ are kept in their standard forms, as the minimization techniques used in the various stability problems use different schemes to eliminate them. Combining the other terms gives the plasma potential energy in straight field line coordinate system

$$\begin{aligned}\delta W_P = \frac{1}{2\mu_0}\int_p \mathrm{d}\mathbf{r}\Bigg[&\frac{\left|(\mathbf{B}\cdot\nabla)\,X\right|^2}{|\nabla\psi|^2} + \frac{|\nabla\psi|^2}{B^2}\left|(\mathbf{B}\cdot\nabla)\,U + X\,(\mathbf{B}\cdot\nabla)\,\Theta^\alpha\right|^2\\ &+B^2\left|\nabla\cdot\xi_\perp + 2\xi_\perp\cdot\kappa\right|^2 + \gamma p|\nabla\cdot\xi|^2\\ &-2\mu_0 p'X\left(X^*\kappa_n + U^*\kappa_g\right) - \mu_0\sigma X^*X\,(\mathbf{B}\cdot\nabla)\,\Theta^\alpha\\ &-\mu_0\sigma\left(X^*\,(\mathbf{B}\cdot\nabla)\,U - U^*\,(\mathbf{B}\cdot\nabla)\,X\right)\Bigg]\end{aligned} \tag{3.64}$$

where the curvatures are found using

$$\kappa\cdot\xi = \kappa\cdot\left(X\frac{\nabla\psi}{|\nabla\psi|^2} + U\frac{\nabla\psi\times\mathbf{B}}{B^2}\right) = \frac{1}{|\nabla\psi|}\left(X\kappa_n + \frac{|\nabla\psi|^2}{B}U\kappa_g\right) \tag{3.65}$$

This form of the plasma potential provides a convenient starting point for the ballooning, peeling, and peeling-ballooning theory in 3D discussed in the remainder of this chapter.

3.3 Linear Ballooning Theory in 3D

Linear ballooning theory is a well studied model for describing the stability of pressure driven ideal MHD modes [14, 15]. While there exist a number of different derivations of the ballooning model, they all tend to follow the same general structure. First, a ballooning eikonal is introduced to account for the large anisotropic behavior relative to the magnetic fields requiring mode structures with long parallel wavelengths and short perpendicular wavelengths [15]. However, the assumptions made for the ballooning eikonal breaks the required poloidal periodicity requirements in the presence of magnetic shear[15], so steps are taken to account for this drawback. This is usually resolved via the ballooning transformation [15] or the introduction of a covering space[14] to expand the periodic domain infinitely while reconciling the local solution. After the solution space of the problem is defined, a variation of normal mode analysis or the Energy Principle can be applied to determine the linear ballooning equation, involving an expansion in the toroidal mode number n to reduce the model.

In this work, motivation for ballooning theory is derived from a number of references [14, 15], but strives to follow a similar setup to [16] peeling-ballooning derivation for easier comparison between the two. Details of the derivation are given in the following sections. First, a discussion of the ballooning formalism is provided, along with identifying the ballooning ordering. Then, a minimization of the plasma potential energy along the lines of section 3.2.4 is used. This derivation does not claim to be as rigorous as those in the provided references, but is still useful in determining the important underlying physics of ballooning instabilities.

3.3.1 Ballooning Formalism and Ordering

The foundations for the ballooning formalism come from the WKB theory from hydrodynamics [17], for which both the wave vector $\mathbf{k}$ and the frequency ω are ordered to be large. The ballooning ordering deviates from this by allowing the frequency to be finite in order to allow for the destabilization of Alfven waves and slow magnetosonic waves to lowest order. As such, the instabilities are assumed to be flute-like ($k_{\parallel}/k_{\perp} \ll 1$), incompressible, and combine the dynamics of the Alfven and slow magnetosonic waves.

Based on the previous assumptions, the ballooning ordering is one with large $\mathbf{k}$, but finite $\mathbf{k} \cdot \mathbf{B}$ and ω. This is achieved by introducing a WKB-like ansatz via the eikonal representation of the perturbation vector

$$\xi = \hat{\xi}(\mathbf{r}) e^{inS(\mathbf{r})} \tag{3.66}$$

where the amplitude $\hat{\xi}(\mathbf{r})$ contains the slow deviations from the flute-like behavior and $n \gg 1$ introduces the expansion parameter $\epsilon = 1/n$. The envelope function $S(\mathbf{r})$ is also constrained to be slowly varying by defining $\mathbf{k} = \nabla S$ to be $\mathcal{O}(\epsilon^0)$. To ensure that the amplitude varies slowly, we constrain $\mathbf{k} \cdot \mathbf{B}$ to vanish to all orders, meaning

$$\mathbf{B} \cdot \nabla S = 0 \tag{3.67}$$

which leads to the solution $S = S(\alpha, \phi)$, such that the exponent of equation 3.66 is not a single-valued function on $\mathbf{r}$. To resolve this, it is necessary to consider only solutions defined on the covering space discussed previously.

For systems with finite magnetic shear, it is useful to use the representation

$$\mathbf{k} = k_\alpha \nabla \alpha + k_\psi \nabla \psi \tag{3.68}$$

where $q' = \partial q/\partial\psi$, $k_\alpha(\alpha,\psi) = \partial S/\partial\alpha$, and $k_\psi = \partial S/\partial\psi$. From this, it is useful to define the parameter

$$\theta_k(\alpha,\psi) = \frac{k_q}{k_\alpha} = \frac{1}{q'}\frac{k_\psi}{k_\alpha} \tag{3.69}$$

thus giving

$$\nabla S = k_\alpha\left(\nabla\alpha + q'\theta_k\nabla\psi\right) \tag{3.70}$$

3.3.2 Ballooning Equation

The first step in solving for the ideal ballooning equation is the minimization of the plasma potential (3.64) along the field lines, to minimize the effects of the compressional Alfven and sound waves. The sounds wave term $\nabla\cdot\xi$ is trivially minimized by choosing the parallel perturbation W such that

$$\nabla\cdot\xi = \nabla\cdot\xi_\perp + \nabla\cdot\xi_\parallel = 0 \tag{3.71}$$

Next, it is necessary to minimize the magnetic response parallel to the field that would break the flute-like mode structure previously assumed. To this end, an ordering technique for the normal and geodesic perturbations is applied as

$$X = X^{(0)} + X^{(1)} + \cdots \qquad U = U^{(0)} + U^{(1)} + \cdots \tag{3.72}$$

with $|X^{(k)}|/|X^{(k+1)}| \sim \mathcal{O}(n)$. Keeping in mind the form of the eikonal, the parallel field component $\nabla\cdot\xi_\perp$ is expanded. To lowest order, we have the relations

$$\hat{X}^{(0)}\left(\frac{\nabla\psi\cdot\nabla S}{|\nabla\psi|^2}\right) + \hat{U}^{(0)}\left(\frac{\nabla\psi\times\mathbf{B}\cdot\nabla S}{B^2}\right) = 0 \tag{3.73}$$

which can be solved to get a relation between the leading orders of X and U. The first order term includes the curvature term $2\kappa\cdot\xi^*$ that was neglected in the lowest order term as it does

not appear there. Including this term, the first order term is given by

$$in\hat{X}^{(1)}\left(\frac{\nabla\psi\cdot\nabla S}{|\nabla\psi|^2}\right)+in\hat{U}^{(1)}\left(\frac{\nabla\psi\times\mathbf{B}\cdot\nabla S}{B^2}\right)+F(\hat{X}^{(0)},\hat{U}^{(0)})=0 \tag{3.74}$$

where

$$\begin{aligned}F(\hat{X}^{(0)},\hat{U}^{(0)})=&\frac{\nabla\psi\cdot\nabla\hat{X}^{(0)}}{|\nabla\psi|^2}+\frac{\nabla\psi\times\mathbf{B}\cdot\nabla\hat{U}^{(0)}}{B^2}+\hat{X}^{(0)}\nabla\cdot\left(\frac{\nabla\psi}{|\nabla\psi|^2}\right)\\&+\hat{U}^{(0)}\nabla\cdot\left(\frac{\nabla\psi\times\mathbf{B}}{B^2}\right)+\frac{2}{|\nabla\psi|}\left(\hat{X}^{(0)}\kappa_n+\frac{|\nabla\psi|^2}{B}\hat{U}^{(0)}\kappa_g\right)\end{aligned} \tag{3.75}$$

can be used to solve the higher-order terms. However, it will be seen that there higher-order terms are not necessary to simply obtain the eigenvalue for the ballooning system. Nevertheless, solutions to the above system are useful for obtaining detailed information on the structure of the eigenfunction.

Referring back to the lowest-order contribution, the geodesic term is related to the normal term such that

$$U=-\left(\Theta^{\alpha}+q'\theta_k\right)X \tag{3.76}$$

where the notation has been simplified. The theta derivative of this expression is also important, and is given by

$$\frac{\partial U}{\partial\theta}=-\left(\Theta^{\alpha}+q'\theta_k\right)\frac{\partial X}{\partial\theta}-X\frac{\partial\Theta^{\alpha}}{\partial\theta} \tag{3.77}$$

Making use of the above minimization, as well as the definition of the magnetic derivative (3.45), the plasma potential energy (3.64) simplifies down to

$$\begin{aligned}\delta W_P=\frac{1}{2\mu_0}\int_p d\mathbf{r}\Bigg[&\frac{1}{|\nabla\psi|^2}\left|\frac{1}{\mathcal{J}}\frac{\partial X}{\partial\theta}\right|^2+\frac{|\nabla\psi|^2}{B^2}\left|\frac{1}{\mathcal{J}}\frac{\partial U}{\partial\theta}+\frac{X}{\mathcal{J}}\frac{\partial\Theta^{\alpha}}{\partial\theta}\right|^2\\&-2\mu_0p'X\frac{1}{|\nabla\psi|}\left(X^*\kappa_n+\frac{|\nabla\psi|^2}{B}U^*\kappa_g\right)\\&-\frac{\mu_0\sigma}{\mathcal{J}}\left(X^*\frac{\partial U}{\partial\theta}+X^*X\frac{\partial\Theta^{\alpha}}{\partial\theta}-U^*\frac{\partial X}{\partial\theta}\right)\Bigg]\end{aligned} \tag{3.78}$$

such that it contains only derivatives along the field line. Making use of the lowest-order relationships given in equations 3.76 and 3.77, the geodesic component of the perturbation U can be eliminated, resulting in the expression

$$\delta W_P = \frac{1}{2\mu_0} \int_p \mathrm{d}\mathbf{r} \left[\frac{1+\Lambda^2}{|\nabla\psi|^2} \left| \frac{1}{\mathcal{J}} \frac{\partial X}{\partial \theta} \right|^2 - 2\mu_0 p' \frac{\kappa_n + \Lambda \kappa_g}{|\nabla\psi|} |X|^2 \right] \tag{3.79}$$

where the integrated local shear, Λ, is defined as

$$\Lambda = -\frac{|\nabla\psi|^2}{B} \left(\Theta^\alpha + q' \theta_k \right) \tag{3.80}$$

It is worth rewriting the plasma potential energy equation in terms of a Hermitian operator. To do this, we take the first term of the potential and rewrite it using integration by parts with the theta integral, where the boundary term vanished since $\xi \to 0$ as $\theta \to \infty$ in order for the solutions to be valid in the specified covering space. Making use of this, the plasma potential can be written in a final form as

$$\delta W_P = \frac{1}{2\mu_0} \int_p \mathrm{d}\mathbf{r} X^* \left[-\frac{1}{\mathcal{J}} \frac{\partial}{\partial \theta} \left(\frac{1}{\mathcal{J}} \frac{1+\Lambda^2}{|\nabla\psi|^2} \frac{\partial}{\partial \theta} \right) - 2\mu_0 p' \left(\frac{\kappa_n + \Lambda \kappa_g}{|\nabla\psi|} \right) \right] X \tag{3.81}$$

where the operator in question is Hermitian as desired.

Similar to the potential energy, it is possible to simplify the kinetic energy of the plasma

$$\mathbf{K}[\xi] = \frac{1}{2} \int_p \mathrm{d}\mathbf{r}\, \rho \left[\frac{1}{|\nabla\psi|^2} |X|^2 + \frac{|\nabla\psi|^2}{B^2} |U|^2 \right] \tag{3.82}$$

using the lowest-order eigenfunctions. Doing so gives an expression for the kinetic energy in terms of the X eigenfunction alone:

$$\mathbf{K}[\xi] = \frac{1}{2} \int_p \mathrm{d}\mathbf{r}\, \rho \left(\frac{1+\Lambda^2}{|\nabla\psi|^2} \right) |X|^2 \tag{3.83}$$

The final step in determining the ideal MHD ballooning equation is to make use of equation 3.35, which states that eigenmodes satisfy

$$\delta W_P[\xi] - \omega^2 K[\xi] = 0 \tag{3.84}$$

Expanding this expression in terms of the energies gives

$$\frac{1}{2\mu_0}\int_p \mathrm{d}\mathbf{r} X^* \left[-\frac{1}{\mathcal{J}}\frac{\partial}{\partial\theta}\left(\frac{1}{\mathcal{J}}\left(\frac{1+\Lambda^2}{|\nabla\psi|^2}\right)\frac{\partial X}{\partial\theta}\right) - 2\mu_0 p'\left(\frac{\kappa_n + \Lambda\kappa_g}{|\nabla\psi|}\right)X - \omega^2\mu_0\rho\left(\frac{1+\Lambda^2}{|\nabla\psi|^2}\right)X\right] = 0 \tag{3.85}$$

This is trivially solved in the case that the integrand goes to zero, giving the linear, ideal MHD ballooning equation as the Euler-Lagrange equation of 3.85

$$\frac{1}{\mathcal{J}}\frac{\partial}{\partial\theta}\left[\frac{1}{\mathcal{J}}\left(\frac{1+\Lambda^2}{|\nabla\psi|^2}\right)\frac{\partial X}{\partial\theta}\right] + 2\mu_0 p'\left(\frac{\kappa_n + \Lambda\kappa_g}{|\nabla\psi|}\right)X + \omega^2\mu_0\rho\left(\frac{1+\Lambda^2}{|\nabla\psi|^2}\right)X = 0 \tag{3.86}$$

Equation 3.86 provides the final form of the ballooning equation, which is used to solve for the eigenvalue ω^2 and thus determine the stability of the system.

3.3.3 Properties of the Ballooning Equation

At its core, the infinite-n ballooning equation is a 1D Sturm-Liouville equation (a second order ODE), written as

$$\frac{\partial}{\partial\theta}\left[P(\theta)\frac{\partial X}{\partial\theta}\right] + Q(\theta)X + \lambda R(\theta)X = 0 \tag{3.87}$$

where the coefficient functions are defined as

$$P(\theta) = \frac{1}{\sqrt{g}}\frac{(1+\Lambda^2)}{|\nabla\psi|^2} \qquad Q(\theta) = \beta'\sqrt{g}\frac{(\kappa_n + \Lambda\kappa_g)}{|\nabla\psi|} \qquad R(\theta) = \sqrt{g}\frac{(1+\Lambda^2)}{|\nabla\psi|^2} \qquad \lambda = \omega^2 \tag{3.88}$$

The eigenvalue λ is related to the shape of the eigenfunction X through the variational expression

$$\lambda = \frac{\int_{-\infty}^{\infty} P(\theta) \left(\frac{\partial X}{\partial \theta}\right)^2 d\theta - \int_{-\infty}^{\infty} Q(\theta) X^2 d\theta}{-\int_{-\infty}^{\infty} R(\theta) X^2 d\theta}. \tag{3.89}$$

This shows that the growth rates are a balance between the stabilizing line-bending energy $(\bar{W}_{LB})$ and the destabilizing pressure-curvature potential $(\bar{W}_{PC})$

$$\bar{W}_{LB} = \int_{-\infty}^{\infty} \delta W_{LB} d\theta = \int_{-\infty}^{\infty} P(\theta) \left(\frac{\partial X}{\partial \theta}\right)^2 d\theta \tag{3.90}$$

$$\bar{W}_{PC} = \int_{-\infty}^{\infty} \delta W_{PC} d\theta = \int_{-\infty}^{\infty} Q(\theta) X^2 d\theta \tag{3.91}$$

with the stability of a given equilibrium and eigenvector X determined based on the relative contributions from these two terms.

3.4 Linear Peeling Theory in 3D

In this work, motivation for the peeling theory is derived predominately from [18], adapting the formulation to tokamak based coordinate system (as in [12, 19]). First, a discussion of the peeling length scale and subsequent expansion is given. Then, minimization of the parallel magnetic perturbation is used to derive an Euler-Lagrange equation for the minimized plasma potential. Finally, analytic solutions to the Euler-Lagrange peeling equation are given which can be related to the Mercier stability criteria for interchange modes[20].

3.4.1 Peeling setup

The starting point for this analysis is to consider the stability of rational surface that lies near the plasma surface. For this derivation, it is useful to deviate from the ballooning style coordinates (α, ψ, θ) used in the previous section to the more conventional (ψ, θ, ζ) system to

take advantage of the periodic properties of the poloidal angle θ and toroidal angle ζ. In this coordinate system, the equilibrium magnetic field is given by equation 3.42.

Using the definition of the displacement vector (equation 3.57) and minimizing δW_P with respect to W to eliminate the compressional sound wave term $\gamma p|\nabla\cdot\xi|^2$, the perturbed plasma potential energy (equation 3.34) can be rewritten as

$$\delta W_P = \frac{1}{2\mu_0}\int_p \mathrm{d}\mathbf{r}\left[\frac{1}{|\nabla\psi|^2}|\mathbf{B}\cdot\nabla X|^2 + \frac{|\nabla\psi|^2}{B^2}\left|\mathbf{B}\cdot\nabla U - X\frac{sB^2}{|\nabla\psi|^2}\right|^2 + B^2|\nabla\cdot\xi_\perp + 2\xi_\perp\cdot\kappa|^2 \right.$$
$$\left. -2\mu_0 p' X\left(X^*\kappa_n + U^*\kappa_g\right) - \mu_0\sigma\frac{sB^2}{|\nabla\psi|^2}X^*X + \mu_0\sigma\left(X^*\mathbf{B}\cdot\nabla U + U^*\mathbf{B}\cdot\nabla X\right)\right] \tag{3.92}$$

where s is the local magnetic shear defined by equation 3.51. In this coordinate system, the derivative along the field line is defined as

$$\mathbf{B}\cdot\nabla = \frac{1}{\mathcal{J}}\left(\frac{\partial}{\partial\theta} + q\frac{\partial}{\partial\zeta}\right). \tag{3.93}$$

The geodesic curvature can be related to the derivative of the parallel current along the field line as

$$\kappa_g = -\frac{1}{2p'}\mathbf{B}\cdot\nabla\sigma \tag{3.94}$$

such that equation 3.92 reduces down to

$$\begin{aligned}\delta W_P = \frac{1}{2\mu_0}\int_p \mathrm{d}\mathbf{r}\Bigg[&\frac{|\mathbf{B}\cdot\nabla X|^2}{|\nabla\psi|^2} + \frac{|\nabla\psi|^2}{B^2}\left|\mathbf{B}\cdot\nabla U - X\frac{sB^2}{|\nabla\psi|^2}\right|^2 \\ &+B^2\left|\nabla\cdot\left(X\frac{\nabla\psi}{|\nabla\psi|^2}\right) + \left(\frac{\nabla\psi\times\mathbf{B}}{B^2}\right)\cdot\nabla U + 2\kappa_n X\right|^2 \\ &-2\mu_0 p'|X|^2 - \mu_0\sigma\frac{sB^2}{|\nabla\psi|^2}|X|^2 \\ &+U^*\left(\mathbf{B}\cdot\nabla\right)\left(\mu_0\sigma X\right) + U\left(\mathbf{B}\cdot\nabla\right)\left(\mu_0\sigma X^*\right)\Bigg]\end{aligned} \tag{3.95}$$

For this analysis, we look to minimize equation 3.95 with respect to X and U, which is done by expanding the perturbation quantities near the rational surface.

3.4.2 Expansion near rational surfaces

Assuming that the instability will radially localize near this surface, we can introduce the small parameter ϵ and corresponding length scale

$$x = \frac{\psi - \psi_0}{\epsilon} \tag{3.96}$$

where $x = 0$ is the rational surface defined by $q_0 = m/n$ and $|x| = 1$ is the plasma edge such that ϵ gives the separation of the rational surface and the plasma boundary. The perturbation quantities satisfy the order

$$x\left(\frac{\partial X}{\partial x}\right) \sim X \tag{3.97}$$

whereas the equilibrium quantities vary weakly in x, such that the safety factor can be Taylor expanded about the rational surface as

$$q(\psi) = q(\psi_0) + (\psi - \psi_0)\left.\frac{\partial q}{\partial \psi}\right|_{\psi_0} \cdots = q_0 + xq'. \tag{3.98}$$

Using this, we can define the magnetic derivative as

$$\mathcal{J}\mathbf{B}\cdot\nabla = \frac{\partial}{\partial\theta} + q_0\frac{\partial}{\partial\zeta} + q'x\frac{\partial}{\partial\zeta} = \frac{\partial}{\partial\eta} + q'x\frac{\partial}{\partial\zeta} \tag{3.99}$$

The local magnetic shear can be written as the sum of the averaged magnetic shear and the variation of the local shear[21]

$$\frac{\mathcal{J}B^2}{|\nabla\psi|^2}s = q' + \mathcal{J}\mathbf{B}\cdot\nabla D = q' + q'x\frac{\partial D}{\partial\zeta} + \frac{\partial D}{\partial\eta} \tag{3.100}$$

where D is a periodic function of θ and ζ. Finally, the perturbation quantities are expanded as

$$X = \epsilon X_1 + \epsilon^2 X_2 + \cdots \tag{3.101}$$

$$U = U_0 + \epsilon^1 U_1 + \cdots \tag{3.102}$$

which can be used to systematically minimize the plasma potential δW_p. In order to

3.4.3 Minimizing the plasma perturbation

Applying the expansion from the previous section, the lowest order contributions come at $\delta W_p \sim \epsilon$ as

$$\delta W^1 = \frac{1}{2\mu_0} \int dx d\theta d\zeta \left[\frac{|\nabla\psi|^2}{\mathcal{J} B^2} \left| \frac{\partial U_0}{\partial \eta} \right|^2 + B^2 \mathcal{J} \left| \frac{\partial X_1}{\partial x} + \left(\frac{\nabla\psi \times \mathbf{B}}{B^2} \right) \cdot \nabla U_0 \right|^2 \right] \tag{3.103}$$

which is minimized with

$$\frac{\partial U_0}{\partial \eta} = 0 \qquad\qquad \frac{\partial X_1}{\partial x} = -\frac{U_0}{d\zeta} = \frac{1}{q_0} \frac{U_0}{d\theta} \tag{3.104}$$

From these expressions, it follows that $\partial X_1 / \partial \eta = 0$ and $\delta W^2 = 0$. To next order, we have

$$\begin{aligned} \delta W^3 = \frac{1}{2\mu_0} \int dx d\theta d\zeta \Bigg[& \frac{1}{q'^2 a_0} \left| \frac{\partial U_1}{\partial \eta} + q' x \frac{\partial U_0}{\partial \zeta} - X_1 \left(q' + \frac{\partial D}{\partial \eta} \right) \right|^2 \\ & + B^2 \mathcal{J} \left| \frac{\partial X_2}{\partial x} + \left(\frac{\nabla\psi \times \mathbf{B}}{B^2} \right) \cdot \nabla U_1 + \cdots \right|^2 \\ & - |X_1|^2 \left(2\mu_0 p' \kappa_n \mathcal{J} + \mu_0 \sigma \frac{\partial D}{\partial \eta} \right) - q' \mu_0 \sigma \frac{d}{dx} \left(x |X_1|^2 \right) \\ & + U_1^* \frac{\partial}{\partial \eta} \left(\sigma X_1 \right) + U_1 \frac{\partial}{\partial \eta} \left(\sigma X_1^* \right) \Bigg] \end{aligned} \tag{3.105}$$

where $a_0 = \mathcal{J} B^2 / (q'^2 |\nabla\psi|^2)$. δW^3 can be minimized by first choosing $\partial X_2 / \partial x$ such that the second set of terms is equal to zero, followed by minimization with respect to U_1. This yields

the Euler-Lagrange equation

$$\frac{\partial}{\partial \eta}\left[\frac{1}{q'^2 a_0}\left(\frac{\partial U_1}{\partial \theta}-\beta\right)\right]+\frac{\partial}{\partial \eta}\left(\mu_0 \sigma X_1\right)=0 \tag{3.106}$$

where

$$\beta = q' x \frac{\partial X_1}{\partial x}+\left(q'+\frac{\partial D}{\partial \eta}\right) X_1 \tag{3.107}$$

Using the periodicity of the configuration, a solution for $\partial U_1/\partial \eta$ can be obtained. Inserting this solution in the above expression yields the final expression for δW^3

$$\delta W^3 = \frac{4\pi^2}{2\mu_0 \oint a_o}\int dx\left[x^2\left|\frac{\partial X_1}{\partial x}\right|^2 - D_M\left|X_1\right|^2+\left(1-H_1\right)\frac{\partial}{\partial x}\left(x\left|X_1\right|^2\right)\right] \tag{3.108}$$

where $\oint a_o = \int_0^{2\pi}\int_0^{2\pi} d\theta d\alpha a_0/4\pi^2$. The Mercier quantity D_m describes the contribution from the pressure-curvature drive given by

$$\begin{aligned} D_M = {} & \mu_0 p' \frac{\hat{V}'^2}{q'^2}\left\langle\frac{B^2}{|\nabla\psi|^2}\right\rangle\left[\mu_0 p'\left\langle\frac{1}{B^2}\right\rangle-\frac{\hat{V}''}{\hat{V}'}\right] \\ & + \mu_0^2\frac{\hat{V}'^2}{q'^2}\left[\left\langle\sigma^2\frac{B^2}{|\nabla\psi|^2}\right\rangle\left\langle\frac{B^2}{|\nabla\psi|^2}\right\rangle-\left\langle\sigma\frac{B^2}{|\nabla\psi|^2}\right\rangle^2\right] \\ & + \mu_0\frac{\hat{V}'}{q'}\left[\left\langle\sigma\frac{B^2}{|\nabla\psi|^2}\right\rangle - I'\left\langle\frac{B^2}{|\nabla\psi|^2}\right\rangle\right], \end{aligned} \tag{3.109}$$

where

$$\langle A\rangle = \frac{\int_0^{2\pi}\int_0^{2\pi} d\theta d\alpha \mathcal{J} A}{\int_0^{2\pi}\int_0^{2\pi} d\theta d\alpha \mathcal{J}} = \frac{1}{4\pi^2}\frac{\int_0^{2\pi}\int_0^{2\pi} d\theta d\alpha \mathcal{J} A}{\hat{V}'}, \tag{3.110}$$

$p' = dp/d\psi$, $I' = dI/d\psi$, and $2\pi I = I_{tor}$ is the net toroidal current. The quantity $\hat{V}'' = (4\pi^2)^{-1} d^2V/d\psi^2$ denotes a magnetic well when $\hat{V}'' < 0$. Finally, the quantity H_1 measures the edge current-peeling drive defined by

$$H_1 = \frac{\mu_0 \hat{V}'}{q'}\left\langle\sigma\frac{B^2}{|\nabla\psi|^2}\right\rangle. \tag{3.111}$$

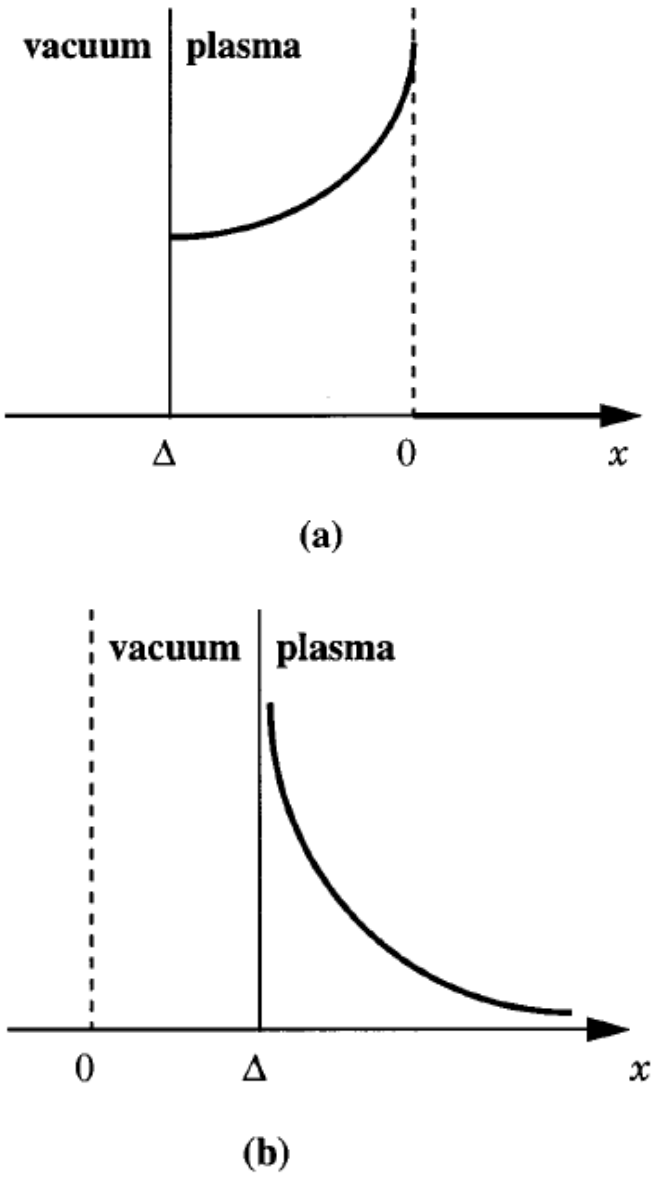

FIGURE 3.1: The geometry for the localized peeling mode analysis, showing the form of the trial function in bold for (a) the rational surface (at $x = 0$) inside the plasma and (b) the rational surface outside the plasma. [19]

3.4.4 Peeling stability

The final step in determining the stability of peeling modes involves the minimization of equation 3.108 via the Euler equation

$$\frac{d}{dx}\left(x^2\frac{dX_1}{dx}\right) + D_M X_1 = 0 \tag{3.112}$$

which has solutions

$$X_1 = a_+|x|^{\lambda_+} + a_-|x|^{\lambda_-} \tag{3.113}$$

with

$$\lambda_\pm = -\frac{1}{2} \pm \sqrt{\frac{1}{4} - D_M}. \tag{3.114}$$

From here, there are two potential cases to consider, as seen in figure 3.1. The first case occurs when the rational surface of interest exists inside the plasma. A trial function is chosen which is zero for $x > 0$ and satisfies 3.112 for $\Delta < x < 0$, where Δ is the separation between the rational surface and vacuum interface (see figure 3.1(a)). For δW_P to be finite, we must choose $a_i = 0$, resulting in

$$\delta W_P = -\frac{2\pi^2}{\mu_0 \oint a_0}|a_+|^2\,\delta^{2\lambda_+ + 1}\left(\lambda_+ + 1 - H_1\right) \tag{3.115}$$

Using this, stability for this case is given by

$$\sqrt{1 - 4D_M} > 2H_1 - 1. \tag{3.116}$$

When the rational surface of interest is outside the plasma (see figure 3.1(b)), we are only interested in solutions for X_1 that are in the plasma, such that $a_+ = 0$. In this case, the solution to 3.112 is

$$\delta W_P = -\frac{2\pi^2}{\mu_0 \oint a_0}|a_-|^2\,\delta^{1+2\lambda_-}\left(\lambda_- - 1 + H_1\right) \tag{3.117}$$

with the corresponding stability requirement

$$\sqrt{1-4D_M} > 1 - 2H_1. \tag{3.118}$$

Combining the two stability conditions (as they both must be satisfied for stability), the stability criterion for the usual tokamak case ($\sigma > 0$) becomes[19]

$$\sqrt{1-4D_M} > 1 + \frac{2}{2\pi q'} \oint \frac{\sigma B^2}{R^2 B_p^3} dl \tag{3.119}$$

where all quantities are evaluated at the plasma surface. From this, it is seen that edge parallel current density is destabilizing when in the same direction as the magnetic field.

For fixed boundary modes, it can be shown that the last term of equation 3.108 vanishes. The resulting equation gives the standard Mercier stability criterion[20]

$$\frac{1}{4} - D_M > 0. \tag{3.120}$$

Comparison of the peeling stability criterion shows the edge current results in a more strict limit on the stability.

3.5 Linear Peeling-Ballooning Theory in 3D

The literature for linear peeling-ballooning theory is much more limited than that of basic ballooning theory, especially in the case of 3D equilibria. There is a significant body of work describing peeling-ballooning modes with axisymmetric equilibria [13, 22], but studies with 3D equilibria are mostly limited to the work described in reference [16], and more recently[23]. In [16], similar steps are made in comparison to the ballooning derivation presented in the previous section, though the assumption of the ballooning ansatz has been relaxed and replaced

with a Fourier decomposition in the α and θ coordinates making similar use of the covering space and principles of functional analysis, with expansion in both the toroidal mode number n and poloidal mode number m. Additionally, peeling-ballooning theory requires application of the full Extended Energy Principle, as the kink response can couple with the plasma-vacuum boundary.

In this work, motivation for the peeling-ballooning theory is derived predominantly from [16, 24–26], but takes some insight from the similar 2D works [13, 22]. First, a discussion of the Fourier representation and relevant assumptions is given. Then, minimization of the parallel magnetic perturbation is used to get relations between the various Fourier coefficients. Finally, the Extended Energy Principle is applied to get set of expressions useful for studying peeling-ballooning modes, at which point some simplifications and comparisons to standard ballooning theory can be made.

3.5.1 Fourier Representation of the Perturbation

The modes being considered in this work are intermediate to high n (i.e. $\epsilon = 1/n \ll 1$), meaning the modes are assumed to have a spectral content that is much higher than that of the equilibrium quantities. To avoid large stabilization of the plasma potential energy due to excitation of Alfven and fast magnetosonic waves, the allowable perturbations have to approximately follow the magnetic field and thus have a fluted shape. Mathematically, this translates to the parallel derivative being of order 1 and thus

$$\mathbf{B} \cdot \nabla = \frac{1}{\mathcal{J}} \frac{\partial}{\partial \theta} \sim \mathcal{O}(1) \tag{3.121}$$

This reduces the order of the normal and geodesic components of $\bar{\mathbf{Q}}$ to $\mathcal{O}(1)$, and the only remaining term of order $\mathcal{O}(\epsilon^{-1})$ is $\nabla \cdot \xi_\perp$. Additionally, the stabilizing term due to sound waves that compress the plasma (the term containing $\nabla \cdot \xi$) is assumed to be minimized

to zero by correctly adjusting the parallel component of the perturbation to cancel out the contribution of $\nabla \cdot \xi_\perp$ due to the perpendicular components (all of order $\mathcal{O}(1)$).

To derive the corresponding criteria relating the two components X and U of $\xi_\perp$, in the (ψ, θ, ζ) coordinate system, the Fourier representation in the variables $\epsilon^{-1}\alpha$ and $\epsilon^{-1}\theta$ is presented, with n the toroidal and m the poloidal mode number

$$X\left(\psi, \epsilon^{-1}\theta, \epsilon^{-1}\zeta\right) = \sum_{m,n} \hat{X}_{m,n}\left(\psi\right) e^{i[n\zeta - m\theta]} \tag{3.122}$$

$$U\left(\psi, \epsilon^{-1}\theta, \epsilon^{-1}\zeta|\theta, \zeta\right) = \sum_{m,n} \hat{U}_{m,n}\left(\psi|\theta, \zeta\right) e^{i[n\zeta - m\theta]} \tag{3.123}$$

where the notation $\left(\psi, \epsilon^{-1}\theta, \epsilon^{-1}\zeta|\theta, \zeta\right)$ means that an additional periodic slow variation of the Fourier amplitude $U_{m,n}$ is allowed, as is customary in multiple-scale analysis [27]. It will be seen that this is necessary to cancel secular terms that will appear to ultimately yield a solution that is indeed periodic. Transforming to the (α, ψ, θ) coordinate system with $\alpha = \zeta - q\theta$, yields

$$e^{i[n\zeta - m\theta]} = e^{i[n\alpha + (nq - m)\theta]} \tag{3.124}$$

which means that the condition that the parallel derivatives be of order $\mathcal{O}(1)$ reduces to

$$nq - m \sim \mathcal{O}(1) \tag{3.125}$$

meaning that the perturbations, though with both $m \sim \mathcal{O}(\epsilon^{-1})$ and $n \sim \mathcal{O}(\epsilon^{-1})$, lie clustered around the line with slope q. This anisotropy has an important implication: the modes do not couple for different magnetic field lines, but only along magnetic field lines, so the double

summation reduces to a single summation over m,

$$\begin{aligned}
&\sum_{m,n}\left[\int \mathrm{d}\theta \int \mathrm{d}\alpha A(\alpha,\psi,\theta)e^{i[n-n']\alpha}e^{i[(nq-m)-(n'q-m')]\theta}\right] X_{m,n}X^*_{m',n'} \\
&=\sum_{m,n}\left[\int \mathrm{d}\theta \left[\int \mathrm{d}\alpha A(\alpha,\psi,\theta)e^{i[n-n']\alpha}\right] e^{i[(nq-m)-(n'q-m')]\theta}\right] X_{m,n}X^*_{m',n'} \\
&\approx \frac{1}{2\pi}\sum_{m,n}\left[\int \mathrm{d}\theta A(\alpha,\psi,\theta)\delta^{n'}_{n} e^{i[(nq-m)-(n'q-m')]\theta}\right] X_{m,n}X^*_{m',n'} \\
&\approx \frac{1}{2\pi}\sum_{m}\left[\int \mathrm{d}\theta A(\alpha,\psi,\theta)e^{i[m'-m]\theta}\right] X_m X^*_{m'}|_{n=n'}
\end{aligned} \tag{3.126}$$

implying that while the equilibrium quantities vary across field lines α, they are quasi-constant in the $n\alpha$ scales on which the perturbations very. Using this, we can see that the Fourier representation becomes

$$X=\sum_m \hat{X}_m\left(\psi\right)e^{i[n\alpha+(nq-m)\theta]} \tag{3.127}$$

$$U=\sum_m \hat{U}_m\left(\psi|\alpha,\theta\right)e^{i[n\alpha+(nq-m)\theta]} \tag{3.128}$$

with the exponents containing both terms of order $\mathcal{O}(1)$ and $\mathcal{O}(n)$ with ϵ from now on chosen to be equal to n^{-1}.

3.5.2 Minimizing the plasma perturbation

The first step in the minimization is to account for the fast variation across the field lines in the coordinate $n\alpha$, which is introduced by inserting only the fast part of the full Fourier representation

$$\begin{aligned}
X&=\hat{X}\left(\psi\right)e^{in\alpha} \\
U&=\hat{U}\left(\psi,\theta|\alpha,\theta\right)e^{in\alpha}
\end{aligned} \tag{3.129}$$

into the condition $\nabla \cdot \xi_\perp \sim \mathcal{O}(1)$. To this end, an ordering technique for the normal and geodesic perturbations is applied as

$$X = X^{(0)} + X^{(1)} + ... \qquad U = U^{(0)} + U^{(1)} + ... \tag{3.130}$$

with $|X^{(k)}|/|X^{(k+1)}| \sim \mathcal{O}(n)$. Expanding $\nabla \cdot \xi_\perp$, the lowest order contribution is given as

$$\hat{U}^{(0)} = \left[\frac{i}{n}\left(\frac{\partial}{\partial\psi} + \Theta^\theta \frac{\partial}{\partial\theta}\right) - \Theta^\alpha\right] \hat{X}^{(0)} \tag{3.131}$$

where again we have defined

$$\Theta^i = \frac{\nabla\psi \cdot \nabla u_i}{\nabla\psi \cdot \nabla\psi}. \tag{3.132}$$

for $\mathbf{u} = (\alpha, \psi, \theta)$.

Note that in this expression, we have left in the θ term of X even though it is formally $\mathcal{O}(1)$. This is done in hindsight by realizing that it is the most convenient way for the geodesic perturbation to be periodic, simplifying the two-scale analysis. The second order term is obtained by balancing the remaining terms in $\nabla \cdot \xi_\perp$ against the curvature term $2\xi_\perp \cdot \kappa$ to minimize the parallel component of the magnetic perturbation. In doing this, we get the relation

$$\left[in\Theta^\alpha + \frac{\partial}{\partial\psi} + \Theta^\theta \frac{\partial}{\partial\theta}\right] \hat{X} + in\hat{U} + \hat{Q}\left(\hat{X}\right) = 0 \tag{3.133}$$

where

$$\begin{aligned} \hat{Q}(\beta) = &\left[2\kappa_n + \frac{1}{\mathcal{J}}\frac{\partial}{\partial u^i}\left(\mathcal{J}\Theta^i\right)\right]\beta \\ &+ \left[2\kappa_g + \frac{1}{\mathcal{J}}\frac{\partial}{\partial\alpha}(\mathcal{J}) - \frac{1}{\mathcal{J}}\frac{\partial}{\partial\theta}\left(\frac{B_\alpha}{B^2}\right) - \frac{1}{\mathcal{J}}\frac{B_\alpha}{B^2}\frac{\partial}{\partial\theta} + \frac{\partial}{\partial\alpha}\right] \\ &\times \left[\frac{i}{n}\left(\frac{\partial}{\partial\psi} + \Theta^\theta\frac{\partial}{\partial\theta}\right) - \Theta^\alpha\right]\beta \end{aligned} \tag{3.134}$$

which now gives the perturbation solution to order $\mathcal{O}(1)$, and eliminates the parallel components of the perturbation and perturbation magnetic response.

The second step is to include the remainder of the Fourier representation for the slow coordinate $(nq - m)\,\theta$ along the magnetic field

$$\begin{aligned} \hat{X} &= \sum_m \hat{X}_m\,(\psi)\,e^{i(nq-m)\theta} \\ \hat{Q} &= \sum_m \hat{Q}_m\,(\psi|\alpha,\theta)\,e^{i(nq-m)\theta} \end{aligned} \tag{3.135}$$

which reduces Eq. 3.133 to

$$U_m = \left(-\Theta^\zeta + \frac{m}{n}\Theta^\theta + \frac{i}{n}\frac{\partial}{\partial\psi}\right) X_m + \frac{i}{n}Q_m(X_m) \tag{3.136}$$

to relate U_m to X_m, where $\Theta^\zeta = \Theta^\alpha + q'\theta + q\Theta^\theta$ and

$$Q_m(X_m) = \left(Q_m^0 + Q_m^1\frac{1}{n}\frac{d}{d\psi}\right) X_m \tag{3.137}$$

where Q_m^0 and Q_m^1 are dependent only on the equilibrium quantities, and are defined as

$$Q_m^0 = \frac{B_\alpha q' + \mathcal{J}\mu_0 p'}{B^\theta} + \left(-\Theta^\zeta + \frac{m}{n}\Theta^\theta\right) Q_m^1 + \frac{nq-m}{n}\frac{\mathcal{J}\mathbf{B}\cdot\nabla\psi\times\nabla\Theta^\theta}{B_\theta} \tag{3.138}$$

and

$$Q_m^1 = -i\,(nq - m)\,\frac{B_\alpha}{B_\theta} \tag{3.139}$$

Note that we have left out the hat to simplify notation and the Fourier mode treatment is implied. The term in Eq. 3.136 proportional Q_M is an order of magnitude smaller than the other terms and U_m contains slowly varying components relative to α and θ as desired. The solution presented here can be plugged into the Energy Principle to obtain a function of the normal displacement X_m accurate to $\mathcal{O}(n)$.

It is worth manipulating the expression for $U_m\left(X_m\right)$ and simplify it in orders of ∂_ψ such that

$$U_m = \left(U_m^0 + U_m^1 \frac{i}{n}\frac{\partial}{\partial\psi}\right) X_m \tag{3.140}$$

with

$$\begin{aligned} U_m^0 &= -\Theta^\zeta + \frac{m}{n}\Theta^\theta + \frac{i}{n}Q_m^0 \\ U_m^1 &= 1 + \frac{i}{n}Q_m^1 \end{aligned} \tag{3.141}$$

thus expressing U_m as a linear differential operator acting on the normal perturbation. It is also worth expanding the parallel derivative of U_m in θ, which can be written out compactly as

$$\frac{\partial U_m}{\partial\theta} = \left(DU_m^0 + DU_m^1 \frac{i}{n}\frac{\partial}{\partial\psi}\right) X_m \tag{3.142}$$

with

$$\begin{aligned} DU_m^0 &= i\left(nq - m\right) U_m^0 + \frac{\partial U_m^0}{\partial\theta} \\ DU_m^1 &= i\left(nq - m\right) U_m^1 + \frac{\partial U_m^1}{\partial\theta} \end{aligned} \tag{3.143}$$

3.5.3 Extended Energy Principle

Making use of the operators defined in the previous section, the terms of the Extended Energy Principle can be expanded in a series, and the components of the normal and geodesic eigenfunction can substituted in. Doing so, it is possible to reduce the volume integrals coupling the modes m and k into three types of terms based on the order of the radial derivative acting on X_m. The plasma potential energy then becomes

$$\frac{1}{2}\sum_{k,m}\int_{\psi_a}^{\psi_s} \mathrm{d}\psi \left[\int \mathrm{d}\theta \mathcal{J} X_k^* e^{i(k-m)\theta}\left\{PV_{k,m}^0 + PV_{k,m}^1\left(\frac{i}{n}\right)\frac{\mathrm{d}}{\mathrm{d}\psi} + PV_{k,m}^2\left(\frac{i}{n}\right)^2\frac{\mathrm{d}^2}{\mathrm{d}\psi^2}\right\}\right] X_m \tag{3.144}$$

along with a surface term

$$\frac{1}{2}\sum_{k,m}\int \mathrm{d}\theta \mathcal{J} X_k^* e^{i(k-m)\theta}\left\{PS_{k,m}^0 + PS_{k,m}^1\left(\frac{i}{n}\right)\frac{\mathrm{d}}{\mathrm{d}\psi}\right\} X_m|_{\psi_s} \tag{3.145}$$

with the coefficients $PV_{k,m}^i$ and $PS_{k,m}^i$ are given by

$$\begin{aligned}
PV_{k,m}^0 &= \widetilde{PV}_{k,m}^0 + \frac{1}{\mathcal{J}}\left(\frac{i}{n}\right)\frac{\mathrm{d}}{\mathrm{d}\psi}\left(\mathcal{J}\widetilde{PV}_{k,m}^{1*}\right)\\
PV_{k,m}^1 &= \left(\widetilde{PV}_{k,m}^1 + \widetilde{PV}_{k,m}^{1*}\right) + \frac{1}{\mathcal{J}}\left(\frac{i}{n}\right)\frac{\mathrm{d}}{\mathrm{d}\psi}\left(\mathcal{J}\widetilde{PV}_{k,m}^2\right)\\
PV_{k,m}^2 &= \widetilde{PV}_{k,m}^2\\
PS_{k,m}^0 &= -\frac{i}{n}\widetilde{PV}_{k,m}^{1*}\\
PS_{k,m}^1 &= -\frac{i}{n}\widetilde{PV}_{k,m}^2
\end{aligned} \tag{3.146}$$

and

$$\begin{aligned}
\widetilde{PV}_{k,m}^0 &= \frac{1}{\mu_0}\frac{|\nabla\psi|^2}{\mathcal{J}^2B^2}\left(DU_k^{0*} - \mathcal{J}S\right)\left(DU_m^0 - \mathcal{J}S\right) + \frac{1}{\mathcal{J}}\frac{\partial\sigma}{\partial\theta}\left(U_k^{0*} + U_m^0\right) + S\sigma\\
&\quad + \frac{\sigma}{\mathcal{J}}\left(i(nq-m)U_k^{0*} - i(nq-k)U_m^0\right) + \frac{1}{\mu_0}\frac{(nq-k)(nq-m)}{\mathcal{J}^2|\nabla\psi|^2} - 2p'\kappa_n\\
\widetilde{PV}_{k,m}^1 &= \frac{1}{\mu_0}\frac{|\nabla\psi|^2}{\mathcal{J}^2B^2}\left(DU_k^{0*} - \mathcal{J}S\right)DU_m^1 + \frac{U_m^1}{\mathcal{J}}\frac{\partial\sigma}{\partial\theta} - \sigma\frac{U_m^1}{\mathcal{J}}i(nq-k)\\
\widetilde{PV}_{k,m}^2 &= \frac{1}{\mu_0}\frac{|\nabla\psi|^2}{\mathcal{J}^2B^2}DU_m^1DU_k^{1*}
\end{aligned} \tag{3.147}$$

The above system is found to be Hermitian, which is useful for obtaining numerical solutions to the system. The integrand of volume term can be expressed in tensorial notation

$$\left(\mathbf{X}^*\right)^T\mathbf{PX} \tag{3.148}$$

where a factor of $\frac{\mathcal{J}}{2}$ has been left out, with $\mathbf{X} = \left(X_m e^{-im\theta}\right)^T$ and the elements of the tensor $\mathbf{P}$ given by

$$P_{k,m} = \widetilde{PV}^0_{k,m} - \frac{i}{n}\frac{\overleftarrow{\partial}}{\partial\psi}\widetilde{PV}^{1*}_{m,k} + \widetilde{PV}^1_{k,m}\frac{i}{n}\frac{\overrightarrow{\partial}}{\partial\psi} - \frac{i}{n}\frac{\overleftarrow{\partial}}{\partial\psi}\widetilde{PV}^2_{k,m}\frac{i}{n}\frac{\overrightarrow{\partial}}{\partial\psi} \tag{3.149}$$

which are indeed Hermitian. The arrows indicate whether the derivatives act on the right or on the left.

For the edge energy term in the Energy Principle, it is assumed that an equilibrium edge current is not present, and thus the term is neglected. In contrast, the vacuum energy is non-negligible, is always stabilizing, and should be minimized while respecting the essential boundary condition. Since the vacuum is current-free, the vacuum magnetic perturbation satisfies

$$\nabla \cdot \mathbf{Q}_v = \nabla \times \mathbf{Q}_v = 0 \tag{3.150}$$

which implies that it can be represented by a scalar potential $\mathbf{Q}_v = \nabla\phi$ that has to obey Laplace's equation

$$\nabla^2\phi = 0 \tag{3.151}$$

Using the essential boundary conditions, we can obtain boundary conditions for the vacuum region at the plasma-vacuum interface surface (s) and the outer vacuum wall (w)

$$\nabla\psi \cdot \nabla\phi = \begin{cases} \mathbf{B}\cdot\nabla X & \text{at } s \\ 0 & \text{at } w \end{cases} \tag{3.152}$$

reducing the vacuum energy term to

$$\delta W_v = -\frac{1}{2}\frac{1}{\mu_0}\int_s \mathcal{J}\left(\mathbf{B}\cdot\nabla X^*\right)\phi \mathrm{d}\theta\mathrm{d}\alpha \tag{3.153}$$

where the negative sign is due to the difference between the definition of the outward normal of the plasma volume and the direction of increasing magnetic flux. Here, we have made use

of the boundary condition to first convert the system to a surface integral around the volume, and then eliminate the side and wall component of the integral as they cancel or are zero, respectively. This leaves a simple surface integral at the plasma-vacuum boundary, which can be treated similarly to the surface terms from the plasma potential.

The plasma potential ϕ is to be solved with Laplace's equation as a function of the plasma perturbation X at the edge. This is done using Green's method, based on Green's second identity

$$\nabla \cdot (a\nabla b) = a\nabla^2 b + \nabla a \cdot \nabla b \tag{3.154}$$

which, upon interchanging a and b, taking the difference between both equations and integrating over the volume

$$\int_v \left(a\nabla^2 b - b\nabla^2 a\right) \mathrm{d}V = \int_{\partial v} (a\nabla b - b\nabla a) \cdot \mathrm{d}\mathbf{S} \tag{3.155}$$

This equation is used by setting $a = \phi(\mathbf{r})$ and $b = G_N(\mathbf{r}, \mathbf{r}') = \frac{1}{|\mathbf{r}-\mathbf{r}'|} + F(\mathbf{r}, \mathbf{r}')$, a modified Green's function for Neumann boundary conditions for the Laplacian in three dimensions, with $\nabla^2 G = -\delta(\mathbf{r} - \mathbf{r}')$ and F a function that is symmetric in its arguments and satisfies

$$\begin{cases} \nabla^2 F(\mathbf{r}, \mathbf{r}') = 0 \\ \nabla\psi \cdot \nabla G_N = -\frac{4\pi}{\partial v} \end{cases} \tag{3.156}$$

where ∂v is the total surface surrounding the volume. Choosing the volume equal to the vacuum volume and evaluating at a point in the plasma edge, this yields an expression for the potential

$$\phi(\mathbf{r}) = <\phi> - \iint_s G_N(\mathbf{r}, \mathbf{r}')\mathcal{J}\mathbf{B}(\mathbf{r}') \cdot \nabla X'(\psi)\mathrm{d}\alpha'\mathrm{d}\theta' \tag{3.157}$$

where $<\phi>$ is the average value of the potential over the whole surface, which is set to an arbitrary constant (zero in this case) due to the surrounding wall. Inserting this expression

into the energy term gives

$$\delta W_v = \frac{1}{2}\sum_{k,m} X_k^* \delta_{k,m}^{vac} X_m \tag{3.158}$$

where the surface integral component is

$$\delta_{k,m}^{vac} = \iint_s \mathcal{J}\mathrm{d}\theta\mathrm{d}\alpha \iint_s \mathcal{J}\mathrm{d}\alpha'\mathrm{d}\theta' V S_{k,m} \tag{3.159}$$

and the Hermitian coefficients are defined

$$VS_{k,m} = \frac{1}{\mu_0}\frac{G_N(\mathbf{r},\mathbf{r}')}{\mathcal{J}^2}(nq-k)(nq-m)e^{-i[n(\alpha-\alpha')+(nq-k)\theta-(nq-m)\theta']} \tag{3.160}$$

Finally, the plasma kinetic energy can be reduced along the lines of the plasma potential energy. The resulting expression for the kinetic energy mimics the expression for the potential

$$K(\xi) = \frac{\omega^2}{2}\int_p \mathrm{d}\mathbf{r}\sum_{k,m} X_k^* e^{i(k-m)\theta}\left\{KS_{k,m}^0 + KS_{k,m}^1\frac{i}{n}\frac{\partial}{\partial\psi} + KS_{k,m}^2\left(\frac{i}{n}\right)^2\frac{\partial^2}{\partial\psi^2}\right\}X_m \tag{3.161}$$

along with a surface term

$$\frac{1}{2}\sum_{k,m}\int \mathrm{d}\theta\mathcal{J}X_k^* e^{i(k-m)\theta}\left\{KS_{k,m}^0 + KS_{k,m}^1\left(\frac{i}{n}\right)\frac{\mathrm{d}}{\mathrm{d}\psi}\right\}X_m|_{\psi_s} \tag{3.162}$$

with the coefficients $KV_{k,m}^i$ and $KS_{k,m}^i$ are given by

$$\begin{aligned}
KV_{k,m}^0 &= \widetilde{KV}_{k,m}^0 + \frac{1}{\mathcal{J}}\left(\frac{i}{n}\right)\frac{\mathrm{d}}{\mathrm{d}\psi}\left(\mathcal{J}\widetilde{KV}_{k,m}^{1*}\right)\\
KV_{k,m}^1 &= \left(\widetilde{KV}_{k,m}^1 + \widetilde{KV}_{k,m}^{1*}\right) + \frac{1}{\mathcal{J}}\left(\frac{i}{n}\right)\frac{\mathrm{d}}{\mathrm{d}\psi}\left(\mathcal{J}\widetilde{KV}_{k,m}^2\right)\\
KV_{k,m}^2 &= \widetilde{KV}_{k,m}^2\\
KS_{k,m}^0 &= -\frac{i}{n}\widetilde{KV}_{k,m}^{1*}\\
KS_{k,m}^1 &= -\frac{i}{n}\widetilde{KV}_{k,m}^2
\end{aligned} \tag{3.163}$$

and

$$\begin{aligned}\widetilde{KV}^0_{k,m} &= \frac{\rho}{|\nabla\psi|^2} + AU^{0*}_k U^0_m \\ \widetilde{KV}^1_{k,m} &= AU^{0*}_k U^1_m \\ \widetilde{KV}^2_{k,m} &= AU^{1*}_k U^1_m\end{aligned} \tag{3.164}$$

3.5.4 The Peeling-Ballooning Equations in 3D

Using the expressions found for the potential energy of the plasma and the kinetic energy, it is possible to take the Euler minimization with respect to each of the M amplitudes of the Fourier modes X^*_k to obtain an equation in the M unknowns X_m. This results in a field line equation for each M mode

$$\sum_m \left\{ \left\langle e^{i(k-m)\theta} V^0_{k,m} \right\rangle_\theta + \left\langle e^{i(k-m)\theta} V^1_{k,m} \right\rangle_\theta \left(\frac{i}{n}\right) \frac{\mathrm{d}}{\mathrm{d}\psi} + \left\langle e^{i(k-m)\theta} V^2_{k,m} \right\rangle_\theta \left(\frac{i}{n}\right)^2 \frac{\mathrm{d}^2}{\mathrm{d}\psi^2} \right\} X_m = 0 \tag{3.165}$$

with the boundary conditions coming from the surface term

$$\sum_m \left\{ \left\langle e^{i(k-m)\theta} S^0_{k,m} \right\rangle_\theta + \left\langle e^{i(k-m)\theta} S^1_{k,m} \right\rangle_\theta \left(\frac{i}{n}\right) \frac{\mathrm{d}}{\mathrm{d}\psi} + \delta^{vac}_{k,m} \right\} X_m = 0 \tag{3.166}$$

for $k = m_0 \cdots m_0 + M$ and the field line average $< \cdot >_\theta$ is defined as

$$\langle A \rangle_\theta = \int_{-\infty}^{\infty} \mathcal{J} A \mathrm{d}\theta \tag{3.167}$$

and the coefficients $V^i_{k,m}$ and $S^i_{k,m}$ are given by

$$V^i_{k,m} = PV^i_{k,m} - \omega^2 KV^i_{k,m} \tag{3.168}$$

and

$$S^i_{k,m} = PS^i_{k,m} - \omega^2 KS^i_{k,m} \tag{3.169}$$

The restriction due to the normalization of the plasma kinetic energy using a Lagrange multiplier ω^2 is mathematically equivalent to the minimization of the Rayleigh quotient with an eigenvalue ω^2 and the appropriate boundary conditions.

3.5.5 Properties of the Peeling-Ballooning Equations

There are a number of similarities between the the 3D peeling-ballooning model and the infinite-n ballooning model that are worth considering. In both models, the stabilizing contribution comes from the line bending term from the δW formulation, so behaviors identified in 3D ballooning studies should also be represented in the full peeling-ballooning model. While the drive term for these instabilities is much more complex, incorporating both the peeling and ballooning sources, they tend to depend on the same geometric quantities as the ballooning case, making analysis of the instabilities and underlying physical changes relatively similar.

The line bending term, $|\bar{\mathbf{Q}}|^2$, can be separated into the normal and geodesic components, both of which are stabilizing. Together, these terms are given by

$$\begin{aligned}
\widetilde{PV}^0_{k,m} &= \frac{1}{\mu_0}\frac{(nq-k)(nq-m)}{\mathcal{J}^2|\nabla\psi|^2} + \frac{1}{\mu_0}\frac{|\nabla\psi|^2}{\mathcal{J}^2B^2}\left(DU^{0*}_k - \mathcal{J}S\right)\left(DU^0_m - \mathcal{J}S\right) \\
\widetilde{PV}^1_{k,m} &= \frac{1}{\mu_0}\frac{|\nabla\psi|^2}{\mathcal{J}^2B^2}\left(DU^{0*}_k - \mathcal{J}S\right)DU^1_m \\
\widetilde{PV}^2_{k,m} &= \frac{1}{\mu_0}\frac{|\nabla\psi|^2}{\mathcal{J}^2B^2}DU^1_m DU^{1*}_k
\end{aligned} \tag{3.170}$$

showing a strong dependence of the stabilizing terms on the magnetic shear. The pressure-curvature term, which is responsible for the ballooning response, is given by

$$\begin{aligned}
\widetilde{PV}^0_{k,m} &= -2p'\left(\kappa_n + U^{0*}_k\kappa_g\right) \\
\widetilde{PV}^1_{k,m} &= -2p'U^1_m\kappa_g \\
\widetilde{PV}^2_{k,m} &= 0
\end{aligned} \tag{3.171}$$

where the $\widetilde{PV}^1_{k,m}$ impacts both the ballooning and the peeling term, so it will be included in both for analysis. This demonstrates that the ballooning drive is proportional to the pressure gradient and curvatures, as expected, as well as a weak dependence on the magnetic shear (through U^{0*}_k, a term related to the integrated local magnetic shear).

The parallel current term, which is responsible for the peeling response, is given by

$$\begin{aligned}
\widetilde{PV}^0_{k,m} &= \frac{1}{\mathcal{J}}\frac{\partial\sigma}{\partial\theta}U^0_m + S\sigma + \frac{\sigma}{\mathcal{J}}\left(i(nq-m)U^{0*}_k - i(nq-k)U^0_m\right) \\
\widetilde{PV}^1_{k,m} &= \frac{U^1_m}{\mathcal{J}}\frac{\partial\sigma}{\partial\theta} - \sigma\frac{U^1_m}{\mathcal{J}}i(nq-k) \\
\widetilde{PV}^2_{k,m} &= 0
\end{aligned} \tag{3.172}$$

where the $\frac{\partial\sigma}{\partial\theta}$ in $\widetilde{PV}^1_{k,m}$ is the shared term with the ballooning component, as it affects both terms. This demonstrates that the peeling drive is directly proportional to the parallel current and the magnetic shear, as well as dependent on the poloidal variation in the parallel current, which will be important in strongly shaped devices. In this case, the local shear is a key factor, but the dependence on it is still weaker than that of the line-bending term. Additionally, there is a 3D coupling term for the imaginary component of the peeling drive.

3.5.6 Reduction of Order near Rational Surfaces

One important case of the 3D peeling-ballooning equations is what happens if the modes localize near rational surfaces (i.e $q = m/n$). Taking the limit as $nq - m \ll 1$, the peeling-ballooning coefficients $\widetilde{PV}^i_{k,m}$ reduce down to the somewhat reduced lowest order term

$$\begin{aligned}
\widetilde{PV}^0_{k,m} = \frac{1}{\mu_0}\frac{|\nabla\psi|^2}{\mathcal{J}^2B^2}\left(DU^{0*}_k - \mathcal{J}S\right)\left(DU^0_m - \mathcal{J}S\right) - 2p'\left(\kappa_n + U^{0*}_k\kappa_g\right) \\
+ \frac{U^0_m}{\mathcal{J}}\left(\frac{\partial\sigma}{\partial\theta} - i(m-k)\sigma\right) + S\sigma
\end{aligned} \tag{3.173}$$

as well as the drastically reduced higher order terms

$$\begin{aligned}
\widetilde{PV}^1_{k,m} &= \frac{1}{\mathcal{J}}\left[\frac{\partial\sigma}{\partial\theta} - i(m-k)\sigma\right] \\
PV^1_{k,m} &= \frac{2}{\mathcal{J}}\frac{\partial\sigma}{\partial\theta} \\
\widetilde{PV}^2_{k,m} &= 0 \\
PV^2_{k,m} &= 0
\end{aligned} \tag{3.174}$$

It's worth noting that the entire order of the differential system is reduced near rational surfaces, with the term proportional to the second radial derivative vanishing completely. The resulting first-order system more closely resembles the form of our ballooning equation, with the line bending term simplified down to

$$\widetilde{PV}^0_{k,m} = \frac{1}{\mu_0}\frac{|\nabla\psi|^2}{\mathcal{J}^2 B^2}\left(D\mathcal{U}^{0*}_k - \mathcal{J}S\right)\left(D\mathcal{U}^0_m - \mathcal{J}S\right) \tag{3.175}$$

with the $\widetilde{PV}^1_{k,m}$ and $\widetilde{PV}^2_{k,m}$ terms vanishing, leaving a term proportionate to the second derivatives along the field line, that is zeroth order with respect to the radial derivatives. The curvature term

$$\begin{aligned}
\widetilde{PV}^0_{k,m} &= -2p'\left(\kappa_n + \mathcal{U}^{0*}_k\kappa_g\right) \\
\widetilde{PV}^1_{k,m} &= -2p'\kappa_g \\
\widetilde{PV}^2_{k,m} &= 0
\end{aligned} \tag{3.176}$$

and peeling term

$$\begin{aligned}
\widetilde{PV}^0_{k,m} &= S\sigma + \frac{1}{\mathcal{J}}\left[\frac{\partial\sigma}{\partial\theta} - i(m-k)\sigma\right]\mathcal{U}^0_m \\
\widetilde{PV}^1_{k,m} &= \frac{1}{\mathcal{J}}\left[\frac{\partial\sigma}{\partial\theta} - i(m-k)\sigma\right] \\
\widetilde{PV}^2_{k,m} &= 0
\end{aligned} \tag{3.177}$$

Both retain a first order dependence on the radial derivatives, but the zeroth order contributions are much more simple to analyze. For the ballooning term, the leading order term is directly related to the ballooning term in the infinite-n model, and should behave in a predictable manner. The peeling term, which is not present in the infinite-n model, is seen to become proportional to the magnetic shear and parallel current, both of which can have significant 3D variation.

References

[1]J. P. Freidberg, *Ideal mhd* (Cambridge University Press, 2014).

[2]J. Wesson, *Tokamaks*, 4th ed. (Oxford University Press, 2011).

[3]H. de Blank, "Plasma equilibrium in tokamaks", Fusion Science and Technology **61**, 89–95 (2012).

[4]W. D. D'haeseleer, W. N. Hitchon, J. D. Callen, and J. L. Shohet (Springer-Verlag Berlin Heidelberg, 1991).

[5]G. H. and R. H., "Hydromagnetic equilibria and force-free fields", Proceedings of the 2nd UN Conf. on the Peaceful Uses of Atomic Energy **31** (1958).

[6]S. V.D., "Equilibrium of a plasma toroid in a magnetic field", J. Exptl. Theoret. Phys. (U.S.S.R) **37** (1960).

[7]J. M. Greene and J. L. Johnson, "Interchange instabilities in ideal hydromagnetic theory", Plasma Physics **10**, 729–745 (1968).

[8]G. Laval, C. Mercier, and R. Pellat, "Necessity of the energy principles for magnetostatic stability", Nuclear Fusion **5**, 156–158 (1965).

[9]H. P. Furth, P. H. Rutherford, and H. Selberg, "Tearing mode in the cylindrical tokamak", The Physics of Fluids **16**, 1054–1063 (1973).

[10]I. B. Bernstein, E. A. Frieman, M. D. Kruskal, and R. M. Kulsrud, "An energy principle for hydromagnetic stability problems", Proc. R. Soc. Lond. A **244**, 17–40 (1958).

[11]E. A. Frieman, J. M. Greene, J. L. Johnson, and K. E. Weimer, "Toroidal effects on magneto-hydrodynamic modes in tokamaks", The Physics of Fluids **16**, 1108–1125 (1973).

[12]D. Lortz, "The general "peeling" instability", Nuclear Fusion **15**, 49–54 (1975).

[13]P. B. Snyder et al., "Edge localized modes and the pedestal: A model based on coupled peeling-ballooning modes", Phys. Plasmas **9**, 2037–2043 (2002).

[14]R. L. Dewar and A. H. Glasser, "Ballooning mode spectrum in general toroidal systems", The Physics of Fluids **26**, 3038–3052 (1983).

[15]J. W. Connor, R. J. Hastie, and J. B. Taylor, "High Mode Number Stability of an Axisymmetric Toroidal Plasma.", Proc R Soc London Ser A **365**, 1–17 (1979).

[16]T. Weyens, R. Sánchez, L. García, A. Loarte, and G. Huijsmans, "Three-dimensional linear peeling-ballooning theory in magnetic fusion devices", Phys. Plasmas **21**, 10.1063/1.4871859 (2014).

[17]R. L. Dewar, "Interaction between hydromagnetic waves and a time-dependent, inhomogeneous medium", The Physics of Fluids **13**, 2710–2720 (1970).

[18]C. Hegna and J. Schmitt, "Peeling stability in quasi-symmetric stellarators", Publication is forthcoming.

[19]J. W. Connor, R. J. Hastie, H. R. Wilson, and R. L. Miller, "Magnetohydrodynamic stability of tokamak edge plasmas", Phys. Plasmas **5**, 2687–2700 (1998).

[20]C. Mercier, "A necessary condition for hydromagnetic stability of plasma with axial symmetry", Nuclear Fusion **1**, 47–53 (1960).

[21]C. C. Hegna, "Local three-dimensional magnetostatic equilibria", Phys. Plasmas **7**, 3921–3928 (2000).

[22]H. R. Wilson, P. B. Snyder, G. T. A. Huysmans, and R. L. Miller, "Numerical studies of edge localized instabilities in tokamaks", Physics of Plasmas **9**, 1277–1286 (2002).

[23]M. Anastopoulos-Tzanis, B. Dudson, C. Ham, C. Hegna, P. Snyder, and H. Wilson, "Non-axisymmetric equilibrium and stability using the ELITE stability code", Nuclear Fusion **59**, 126028 (2019).

[24]T. Weyens, R. Sánchez, G. Huijsmans, A. Loarte, and L. García, "PB3D: A new code for edge 3-D ideal linear peeling-ballooning stability", J. Comput. Phys. **330**, 997–1009 (2017).

[25]T. Weyens, "Expressions for perturbed vacuum potential energy for 3D linear MHD stability", Phys. Plasmas **26**, 10.1063/1.5086538 (2019).

[26]T. Weyens, J. M. Reynolds-Barredo, and A. Loarte, "Computationally advantageous expressions for 3-D MHD stability", Comput. Phys. Commun. **242**, 60–71 (2019).

[27]C. M. Bender and S. A. Orszag, *Advanced mathematical methods for scientists and engineers i* (Springer-Verlag New York, 1999).

Chapter 4

Overview of Numerical Tools

Finding useful solutions to the MHD equilibrium and stability equations derived in Chapter 3 generally requires the use of numerical tools, especially when considering realistic experimental configurations. While simple analytic solutions to these problems do exist, they require a number of assumptions and simplifications to be made, including very simplistic geometries, significantly limiting the scope of their usefulness. Because of this, it is necessary to rely on computational tools in order to perform more comprehensive analysis of these models. There are a wide range of MHD based codes currently in use or development.

For this project, the numerical workflow is typically done in three parts: experimental reconstruction, equilibrium calculations, and stability analysis. Initially, the CLISTE code[1] is used to solved the 2D Grad-Shafranov equation under the constraint of experimental data from ASDEX Upgrade. These experimental reconstructions describe the axisymmetric equilibrium profiles and magnetic fields. For studies involving axisymmetric equilibria, the CLISTE reconstructions are used as inputs to the HELENA code[2] to produce equilibria formatted for a variety of analysis tools.

For non-axisymmetric studies, the impact of externally imposed 3D magnetic fields is accommodated by treating the resultant state as a 3D MHD equilibria. As the 3D MHD problem

cannot be described as a Grad-Shafranov solution, specialized equilibrium tools need to be employed. The 2D CLISTE reconstructions can be used along was experimental data on the 3D perturbation coil configuration as inputs to the VMEC code[3], producing complete 3D equilibria with varied parameters useful for our analysis.

Finally, these equilibria provide the inputs for the various MHD stability and analysis codes used in this work. The PyBalloon code (section 4.3) uses 3D VMEC equilibria to study the effects of the 3D magnetic geometry on infinite-n ballooning stability, and is used extensively for the analysis presented in chapter 5. For finite-n peeling-balloon stability, the PB3D code (section 4.4) uses either 2D HELENA or 3D VMEC equilibria, allowing a wide range of problems to be analysed. PB3D is still in the development stages, with code testing and verification being the focus of Chapter 6.

4.1 Equilibrium Codes

Equilibrium solvers provide a good starting point for computational plasma analysis, and can be combined with experiments, theory, and simulations for exploring and isolating specific plasma behaviors. There are a wide range of different equilibrium tools, with the equilibria produced ranging from very simple models useful for comparing numerical and analytic results, to more complex equilibria used to explore experimental conditions and complex plasma phenomena.

Experimental reconstruction is used to determine the equilibrium state of a given experimental plasma using diagnostic measurements, effectively creating a "snapshot" of that specific discharge. The accuracy of the reconstruction and range of information it contains is largely determined by the availability of experimental data. This presents a number of challenges, as a large number of diagnostics are required to properly quantify the plasma core, pedestal, and edge regions, each addressing a range of different phenomena and physical

scales. Additionally, diagnostics in tokamaks are typically designed to take advantage of axisymmetry, meaning experimental reconstructions are inherently 2D, posing a problem for studying RMPs and 3D geometry. Nevertheless, they provide an invaluable tool for tokamak data analysis and relating experimental observations to comparable computational analysis.

The EFIT code [4, 5] is one of the most widely used experimental reconstruction equilibrium codes, utilized by DIII-D, JET, MAST-U, and a number of other tokamak facilities. EFIT leverages a Green function approach to the Grad-Shafanov equation combined with a Picard linearization scheme interleaved between the equilibrium and fitting iterations to accurately and efficiently find the optimal equilibrium solution. EFIT can be used both in real-time for equilibrium construction and plasma control [6], as well as in post processing where calculations requiring larger computational resources and higher accuracy are required.

The CompLete Interpretive Suite for Tokamak Equilibria, or CLISTE, is another equilibrium reconstruction tool used predominantly by the ASDEX-Upgrade tokamak [1]. CLISTE consists of both a slow and fast mode of operation. The slow mode uses nonlinear least squares optimization of the Garching Equilibrium Code[7] to find equilibrium solutions that best match a set of user-specified diagnostic signals, producing highly accurate reconstructions at significant computational cost. CLISTE's fast mode leverages a linear optimization scheme similar to that of EFIT to rapidly identify equilibria profiles, making it useful for real-time equilibria control and rapid analysis.

In many cases, equilibrium reconstructions are used as the starting point for other equilibrium codes. This is useful for mitigating accumulated errors in the reconstructions, creating a large set similar equilibria for studying the effects of specific parameters on stability boundaries, or adding physics not available in the reconstructions, such as the 3D field effects.

One of the most widely used equilibrium codes—and the primary code used in this work—is VMEC[3, 8], which is discussed at length in the next section. This work also makes use of the axisymmetric HELENA equilibrium code[2] as a part of the PB3D benchmarking exercise in chapter 6.

4.1.1 VMEC

The starting point for the problems studied in this thesis is the 3D nonlinear ideal MHD equilibria developed using the Variational Moments Equilibrium Code (VMEC) [3, 8]. These VMEC equilibria use 2D experimental reconstructions (from CLISTE and EFIT) and the measured plasma response to 3D magnetic perturbations to construct equilibria derivative of specific experimental results for both ASDEX Upgrade and DIII-D systems, as well a number of 3D stellerators. This thesis makes use of the PARVMEC version, a new parallelized implementation of VMEC, allowing for both highly accurate equilibria calculations as well as rapid iteration on different equilibrium solutions to study a variety of equilibrium parameters [9].

At its core, VMEC minimizes the total energy of a plasma confined in a toroidal domain

$$W_p = \int \left(\frac{1}{2} B^2 + p \right) \mathrm{d}\ V \tag{4.1}$$

by prescribing the magnetic flux on each surface and the pressure profile to produce an equilibrium state. The magnetic field $\mathbf{B}$ is given in the Clebsch coordinate system

$$\mathbf{B} = \nabla s \times \nabla \nu \tag{4.2}$$

where s is radial flux variable, typically equal to the normalized toroidal flux $\psi(s)/\psi(1)$ such that $s \in (0, 1)$. The angular coordinate, $\nu = \psi'(\theta + \lambda) - \chi'\zeta$ with poloidal angle θ and toroidal angle ζ is helical in nature, with $\lambda(\psi)$ being a periodic stream function used to take advantage of straight field line geometries (with $\theta + \lambda$ equal to the poloidal coordinate in which the field lines are straight), while introducing a degree of freedom useful for accelerating the series convergence of the equilibrium mapping (R, Z) significantly improving code performance

[8]. The main output from VMEC is the equilibrium mapping, given by

$$\begin{aligned} R(s,u,v) &= \sum_{m,n} \left[r^c_{m,n}(s) \cos(mu - nv) + r^s_{m,n}(s) \sin(mu - nv) \right] \\ Z(s,u,v) &= \sum_{m,n} \left[z^c_{m,n}(s) \cos(mu - nv) + z^s_{m,n}(s) \sin(mu - nv) \right] \end{aligned} \tag{4.3}$$

as well as the magnetic field components (which have a similar form). The mapping and magnetics, as well as the profile variables pressure and safety factor, provide the basis for the stability calculations performed using the PyBalloon and PB3D codes, to be discussed.

Care needs to be taken when producing 3D equilibrium, as a number of factors can lead to poorly converged equilibria. The main issue is that VMEC assumes the existence of nested flux surfaces, excluding the tearing response necessary for the formation of magnetic islands. In doing so, singularities in the current form at rational surfaces, which are not rigorously treated in the code. Studies have shown radial grid resolution can strongly influence the non-axisymmetric plasma currents near rational surfaces, resulting in improper calculations of the kink response and related 3D geometry terms important to this work [10]. Currents generated at rational surfaces in VMEC tend to increase in magnitude and decrease in radial width with decreasing radial step size, slowly moving toward the theoretical limit of radial delta functions, though they do not saturate or fully converge [11].

While this raises questions to the validity of VMEC near rational surfaces, analysis of the key geometric quantities studied here shows convergence with sufficient radial resolution, allowing use of the 3D VMEC equilibrium for the cases of interest [11]. PARVMEC makes use of a non-linear radial grid distribution to densely pack magnetic surfaces near the plasma edge, further alleviating these problems [12]. Additionally, PARVMEC provides a convenient workflow for computing the necessary free-boundary equilibria using an iterative process to maximize the convergence rate for the equilibrium, leading to higher quality equilibria with quick turnaround and better reproducible.

4.2 MHD Stability Codes

In addition to MHD equilibrium tools, there are a large number of codes used to study the local and global stability of a given equilibrium configuration. These codes are classified as linear or non-linear, as well as by the type of MHD model that they employ. The most complex codes, such as NIMROD[13] or M3D-C1[14], make use of the expansive, non-linear, extended MHD model[15], allowing them to address a wide range of different plasma phenomena over extensive parameter spaces, but are computationally expensive and often contain more physics than necessary for a simpler problem. At the other extreme are codes that make use of linear reduced models like the ballooning or peeling theory discussed in chapter 3. These codes tend to be significantly easier and cheaper to run, but are much more limited in scope. One challenge in computational stability analysis is choosing the numerical tools best suited for a specific problem. Because of this, it is common practice to perform stability analysis using a mix of different tools to assess the validity of the different models and help identify the key physical phenomena for a given instability.

Linear ideal MHD codes are useful for determining the stability limits of a given equilibrium based on a number of plasma conditions, including the magnetic geometry, boundary conditions, pressure and current profiles, magnetic safety factor, and plasma rotation. This can be especially useful in determining the operational limits for certain experiments and providing design constraints for new devices. While some of the most basic linear codes only determine plasma stability thresholds, higher order codes can be used to address issues like instability onset, mode structure, and some of the more basic dynamical characteristics of the instability.

In many cases, linearization of the MHD models used in these codes is done along side expansions with respect to toroidal mode number, n, to further simplify the physics being studied and computational demands of the code. For example, the ballooning codes COBRA[16,

17] and PyBalloon (4.3) make use of the lowest order expansion of the formally infinite-n ballooning model (section 3.3). This allows for highly efficient calculations of the absolute ballooning stability limits of a given equilibrium, but sacrifices physics elements such as global mode structure and instability dynamics. By comparison, intermediate to high-n codes such as ELITE[18] relax the strict infinite-n assumption of the ballooning model and make use of higher order terms in the toroidal mode expansion to gain insight into the instability onset and mode structure, but still lack the necessary physics for studying the complete dynamical behavior of the mode.

Due to the limits of the linear MHD models, it is often necessary to include non-linear MHD physics in order to achieve a comprehensive understanding of a plasma instability. In terms of ELM stability studies, nonlinear effects may be critical in understanding mode evolution, size, relaxation, and saturation; post ELM crash dynamics; and the energy and particle transport in ELMy discharges. While the scope of this thesis is limited to linear MHD analysis for edge instabilities, non-linear codes will likely be necessary to fully understand the effects of the 3D magnetic geometry on stability.

The primary stability analysis tools used in this work are PyBalloon and PB3D, which are discusses at length in the remaining sections of this chapter. In addition to these newly developed tools, the existing codes COBRA[16, 17], MISHKA[2, 19, 20], and ELITE[18] are used for the benchmarking exercise discussed in chapter 6.

COBRA

The COBRA code[16] is a highly optimized ballooning solver built to take advantage of the 3D equilibrium calculations from VMEC. The computational bottleneck for any ballooning code is the evaluation of the ballooning coefficients P, Q, and R (see equation 5.2) for a given magnetic field line. VMEC calculates the magnetic field and metric components necessary for determining the ballooning coefficients in terms of Fourier coefficients in a straight field line geometry. The Fourier inversion of these series inside of COBRA makes up the majority of

the computational expense, and can be minimized by taking advantage of fast solvers and minimizing the number of grid points necessary for a well converged eigenvalue.

For the solver, COBRA solves a discrete form of the ballooning equation cast into a matrix form

$$A\bar{F}^m = \lambda^m \bar{F}^m \tag{4.4}$$

where $\bar{F}^m$ and λ^m are the matrix eigenvector and eigenvalue, respectively. In this form, the task of solving the ballooning spectrum is simplified to obtaining the eigenvalues of the discrete coefficient matrix A, a real nonsymmetric tridiagonal matrix, allowing use of a very fast algorithm. Specifically, COBRA uses a combination of Gerschgorin's theorem along with bisection and Newton-like methods to rapidly identify the most unstable eigenvalue.

In order to further improve efficiency, COBRA implements a combination of variational refinement and Richardson extrapolation to significantly improve the convergence relative to the mesh step size, h. The initial eigenvalue estimate is calculated using the matrix formulation above and a second-order discretization of the ballooning formalism, solved on a relatively coarse mesh for speed. Using the variational expression for the ballooning equation (3.35 and 3.89) and a higher order discretization, subsequent iterations of mesh refinement can achieve fourth-order numerical convergence while Richardson convergence is used to maintain a linear scaling in the computational costs with respect to the step-size. These improvements make COBRA significantly more efficient than other 3D ballooning solver codes.

MISHKA

The MISHKA-1 code[2] is a general linear ideal MHD stability tool for utilized for studying axisymmetric equilibria from the HELENA code. MISHKA takes advantage of the axisymmetric geometry to solve a set of MHD equations that are optimized for conditions specific to tokamak discharges.

MISHKA uses a numerical scheme based on the Galerkin method to solve the MHD equation in their weak form[20], allowing for problems described by non-self-adjoint MHD operators to be studied. This opens up room for improvements to MISHKA-1 to include more complicated effects such as flow (MISHKA-F[21]) or non-ideal MHD effects such as drifts (MISHKA-D[20]).

ELITE

The ELITE (edge localized instability in tokamak equilibria) code[18, 22] is a linear MHD analysis tool used to better understand short wavelength instabilities in close proximity to the plasma edge, making it an essential tool for the study of ELMs. ELITE employs a linear peeling-ballooning model[18] similar to that of section 3.5, which consists of an expansion of the energy principle with respect to the inverse toroidal mode number n^{-1} to second order, retaining the surface terms and radial current density information necessary for describing peeling mode. This model includes the physics of the infinite-n ballooning model, extending them to include finite-n effects like the peeling drive and mode coupling.

ELITE evaluates the change in energy associated with a radial perturbation of a plasma fluid element, X, for the intermediate-high n peeling-ballooning equation, derived from the ideal MHD energy principle $\delta W(X)$. This Euler equation is solved by Fourier decomposing X as

$$X = \sum_m u_m(\psi) e^{-im\omega} \tag{4.5}$$

where ψ is the poloidal flux, m are the poloidal mode numbers, and ω is the straight field line poloidal angle. This results in a series of coupled differential equations of the general form

$$\sum_m \left[A^2_{m,k} \frac{d^2 u_m}{d\psi^2} + A^1_{m,k} \frac{du_m}{d\psi} + A^0_{m,k} u_m \right] = 0 \tag{4.6}$$

for the plasma contribution and

$$\sum_m \left[S^2_{m,k} \frac{d^2 u_m}{d\psi^2} + S^1_{m,k} \frac{du_m}{d\psi} + S^0_{m,k} u_m + \delta W^v_{m,k} u_m \right] = 0 \tag{4.7}$$

for the surface contribution. The $\delta W^v_{m,k}$ term represents the contribution of the vacuum potential energy, given in terms of the plasma displacement at the plasma-vacuum interface having assumed a vacuum model where the vessel wall is far from the plasma boundary.

The above equations constitute the complete eigenmode system that ELITE solves to determine the stability of a given equilibrium configuration and calculate the corresponding eigenvalue for that system. To increase the efficiency of these calculations, ELITE first separates the equilibrium and perturbation length scales, allowing the equilibrium components to be calculated on a coarse mesh, with only the Fourier modes u_m requiring a fine radial grid. ELITE further simplifies the problem by assuming the perturbations to be highly localized around rational surfaces due to the bending in the magnetic field lines. These simplifications provide significant reduction in the required computational resources.

Two major drawbacks to the ELITE code are the absence of low-n physics that may be important to some problems and the restriction to studying axisymmetric equilibria. For the former, ELITE traditionally is paired with the low-n stability code GATO[23]. There have been efforts to further expand the peeling-ballooning formulation used in ELITE to include higher orders of the n^{-1} expansion, allowing low-n physics to be incorporated into the model[24]. More recently, ELITE has been expanded using linear perturbation theory to allow for 3D equilibrium and magnetic perturbation effects to be studied[25]. These advancements significantly increase the number of problems accessible to the ELITE code, though development on them is ongoing.

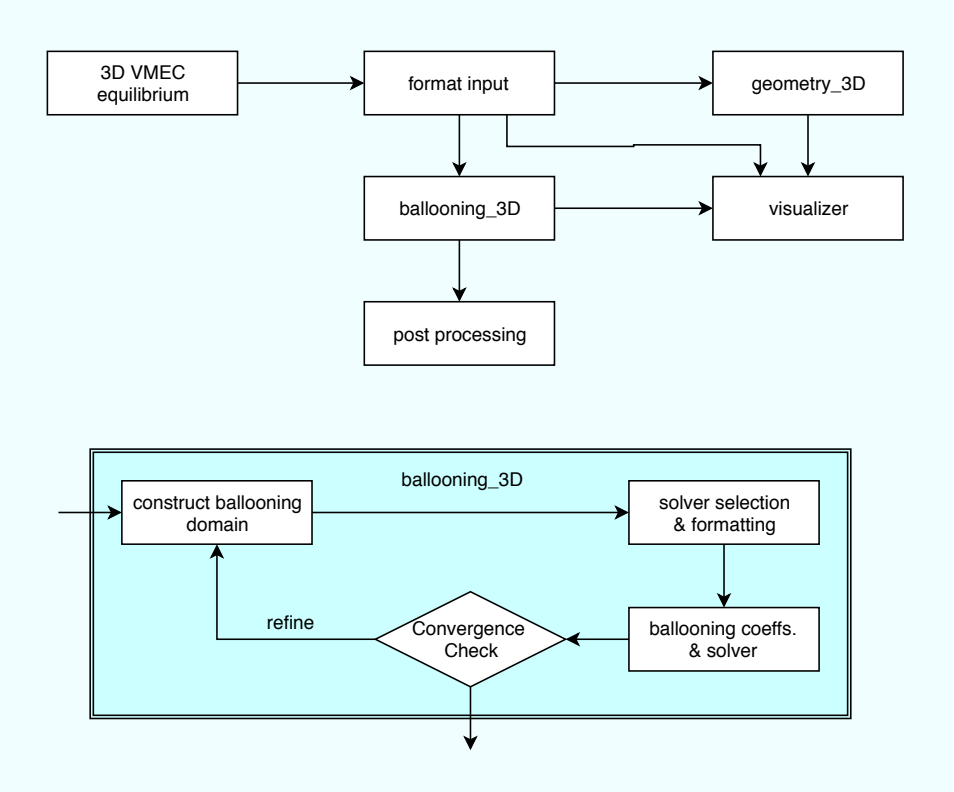

FIGURE 4.1: Workflow for PyBalloon

4.3 The PyBalloon Code

The PyBalloon code is an infinite-n ideal ballooning eigenvalue solver developed for studying ballooning stability of 3D VMEC equilibria built in Python3[26]. While other 3D ballooning codes exist (such as COBRA [16]), PyBalloon was developed specifically for studying the effects of 3D geometry on ballooning stability.

The PyBalloon code is designed in a modular way, creating a clean workflow and allowing for easy customization to specific problems. The general layout of the code is given in Figure 4.1. Starting from a VMEC equilibrium as an input, the data is preprocessed for use by the code. This process includes converting the VMEC output into a ballooning coordinate system and formatting the data so it is optimized for future calculations. While VMEC is currently the only equilibrium code used as an input, alternate equilibrium codes could be used by simply creating a new preprocessing module, without making any changes to the core code. This allows for a large amount of flexibility, allowing users to take data from whichever source best suites their needs.

The core components of PyBalloon are the 3D geometry and 3D ballooning modules. As the main purpose of PyBalloon is to study the impact of 2D and 3D geometric quantities on ballooning stability, the inclusion of a comprehensive geometry module is essential. This module makes use of the equilibrium mapping and magnetics to calculate the various geometric quantities discussed in section 3.2 both along a single field line and across a full flux surface. Analyzing the geometric quantities along each field line is useful for determining contributions of various terms to isolated field line stability, while analysis of the complete flux surface allows for qualitative analysis of 3D variations in the geometry and how that relates to localized stability.

The ideal MHD ballooning eigensolver used in PyBalloon is an extension of the STESA code[27–29] and its successor developed for studying ballooning in local 3D equilibria[30,

31]. These codes are based on and utilize numerical techniques from the well studied ballooning solver COBRA [16], with STESA having been benchmarked directly against the COBRA solver[27]. Our extension of these codes utilizes the same underlying eigensolver, while allowing for more flexibility in choice of equilibria and additional tools for analysis of the equilibria and eigenvalue results.

4.3.1 Ballooning Module

The ballooning module calculates the stability of a single field line; repeated calculations over a number of field lines can then be used to map the ballooning stability throughout the domain. The ideal ballooning equation (Equation 3.86) being solved here is a second order, linear ordinary differential equations, which can be written in the form

$$\frac{\partial}{\partial\theta}\left[P(\theta)\frac{\partial}{\partial\theta}\right]\xi + Q(\theta)\xi + \lambda R(\theta)\xi = 0 \tag{4.8}$$

where $\lambda = \omega^2$. For a given magnetic field line, a descretized ballooning domain can be created ranging from $\theta = (-\theta_\infty, \theta_\infty)$ where θ_∞ is sufficiently large enough to approximate the theoretically infinite ballooning domain. Using an odd number of points n_θ, a full and half grid can be defined as

$$\theta_j = -\theta_\infty + h(j-1), \quad j = 1, ..., n_\theta \tag{4.9}$$

$$\theta_{j+1/2} = -\theta_\infty + h(j-1/2), \quad j = 1, ..., n_\theta - 1 \tag{4.10}$$

with the step-size $h = 2\theta_\infty/(n_\theta - 1)$. The ballooning equation can be written as eigenvalue problem

$$\mathbf{A}\cdot\xi = \lambda\xi \tag{4.11}$$

where the values of the matrix **A** are given by

$$h^2 A_{ij} = \delta(i-j+1)\left(\frac{P_{j+3/2}}{R_j}\right) + \delta(i-j-1)\left(\frac{P_{j+1/2}}{R_{j+1}}\right) - \delta(i-j)\left(\frac{P_{j+3/2}+P_{j+3/2}-h^2 Q_{j+1}}{R_{j+1}}\right) \tag{4.12}$$

for $i, j = 1, ..., n_\theta - 2$ and the boundary conditions

$$\xi_1 = \xi_{n_\theta} = 0. \tag{4.13}$$

This reduces the problem down to finding the most unstable eigenvalue of **A**, as well as the corresponding eigenvector. The matrix **A** is tridiagonal with non-negative off-diagonal components, which allows for efficient computation of the most unstable eigenvalue, which is done using standard PYTHON tools.

4.3.2 Geometry Module

In order to accurately calculate the various 3D geometric quantities that arise in ballooning theory, it is advantageous to work in terms of the equilibrium metric, as well as the covariant and contravarient components of the magnetic field. Using VMEC as a starting point, PyBalloon makes use of the metric converting between the cylindrical coordinate system (R, ϕ, Z) and toroidal coordinate system (ψ, θ, ζ) given by

$$\mathbf{x}(\theta, \zeta) = R(\theta, \zeta)\hat{R} + Z(\theta, \zeta)\hat{Z} \tag{4.14}$$

as the basis for the geometry calculations. Using this, the magnetic field vector can be defined as

$$\mathbf{B} = B^\theta \mathbf{x}_\theta + B^\zeta \mathbf{x}_\zeta = B_\psi \nabla\psi + B_\theta \nabla\theta + B_\zeta \nabla\zeta \tag{4.15}$$

where $\mathbf{x}_i = \frac{\partial \mathbf{x}}{\partial u_i}$, $B^i = \mathbf{B} \cdot \nabla u_i$ are the contravariant components of the magnetic field, and $B_i = \mathbf{B} \cdot \mathbf{x}_i$ are covariant components of the magnetic field. Additionally, it is convenient to

define

$$\mathbf{N} = \mathcal{J}\ \nabla\psi = \mathbf{x}_\zeta \times \mathbf{x}_\theta \tag{4.16}$$

as an alternative to the normal vector, since the Jacobian term will cancel regardless with normalization. Using these expressions above, the orthonormal magnetic field coordinate system $\left(\hat{b}, \hat{n}, \hat{b}\times\hat{n}\right)$ can be defined as

$$\hat{b} = \frac{B^\zeta \mathbf{x}_\zeta + B^\theta \mathbf{x}_\theta}{B} \qquad \hat{n} = \frac{\mathbf{x}_\zeta \times \mathbf{x}_\theta}{N} \qquad \hat{b}\times\hat{n} = \frac{B_\theta \mathbf{x}_\zeta - B_\zeta \mathbf{x}_\theta}{BN} \tag{4.17}$$

where $B = |\mathbf{B}|$ and $N = |\mathbf{N}|$ are normalization constants. In this coordinate system, derivatives along the magnetic field lines can be defined as

$$\hat{b}\cdot\nabla = \frac{1}{B}\left[B^\theta \frac{\partial}{\partial\theta} + B^\zeta \frac{\partial}{\partial\zeta}\right] \tag{4.18}$$

with which we can determine the geometric quantities defined in section 3.2.3. To begin with, the expression for the curvature and torsion vectors are found to be

$$\begin{aligned}\bar{\kappa} &= \left(\hat{b}\cdot\nabla\right)\hat{b} = \left[b^\zeta\frac{\partial}{\partial\zeta} + b^\theta\frac{\partial}{\partial\theta}\right]\left[b^\zeta\mathbf{x}_\zeta + b^\theta\mathbf{x}_\theta\right] \\ &= b^\phi b^\phi \mathbf{x}_{\zeta\zeta} + b^\theta b^\theta \mathbf{x}_{\theta\theta} + 2b^\phi b^\theta \mathbf{x}_{\zeta\theta} + \left[\left(\hat{b}\cdot\nabla\right)b^\zeta\right]\mathbf{x}_\zeta + \left[\left(\hat{b}\cdot\nabla\right)b^\theta\right]\mathbf{x}_\theta\end{aligned} \tag{4.19}$$

and

$$\begin{aligned}\bar{\tau} &= -\left(\hat{b}\cdot\nabla\right)\hat{b}\times\hat{n} = -\left[b^\zeta\frac{\partial}{\partial\zeta} + b^\theta\frac{\partial}{\partial\theta}\right]\left[b_\theta\mathbf{x}_\zeta - b_\zeta\mathbf{x}_\theta\right] \\ &= b^\theta b_\zeta \mathbf{x}_{\theta\theta} - b^\zeta b_\theta \mathbf{x}_{\zeta\zeta} + \left(b^\zeta b_\zeta - b^\theta b_\theta\right)\mathbf{x}_{\theta\phi} - \left[\left(\hat{b}\cdot\nabla\right)b_\theta\right]\mathbf{x}_\zeta + \left[\left(\hat{b}\cdot\nabla\right)b_\zeta\right]\mathbf{x}_\theta\end{aligned} \tag{4.20}$$

where

$$b^i = \frac{B^i}{B} \qquad b_i = \frac{B_i}{BN} \tag{4.21}$$

are new field variables chosen for simplicity.

Before calculating the final geometric quantities, it is necessary to first transform the orthonormal magnetic coordinates $\left(\hat{b}, \hat{n}, \hat{b} \times \hat{n}\right)$ into an orthonormal cylindrical system $\left(\hat{R}(\zeta), \hat{\phi}(\zeta), \hat{Z}\right)$, where it is noted that the unit vectors $\hat{R}$ and $\hat{\phi}$ are dependent on the toroidal coordinate ζ such that

$$\hat{R}_\zeta = \hat{\phi} \qquad \hat{\phi}_\zeta = -\hat{R}, \tag{4.22}$$

resulting in the metric derivatives

$$\begin{aligned}
\mathbf{x}_\theta &= R_\theta \hat{R} + Z_\theta \hat{Z}, \\
\mathbf{x}_\zeta &= R_\zeta \hat{R} + Z_\zeta \hat{Z} + R\hat{\phi}, \\
\mathbf{x}_{\theta\theta} &= R_{\theta\theta} \hat{R} + Z_{\theta\theta} \hat{Z}, \\
\mathbf{x}_{\zeta\theta} &= R_{\zeta\theta} \hat{R} + Z_{\zeta\theta} \hat{Z} + R_\theta \hat{\phi}, \\
\mathbf{x}_{\zeta\zeta} &= \left(R_{\zeta\zeta} - R\right) \hat{R} + Z_{\zeta\zeta} \hat{Z} + 2R_\zeta \hat{\phi}.
\end{aligned} \tag{4.23}$$

Additionally, the magnetic vectors can be defined in terms of the cylindrical metric as

$$\mathbf{B} = \left(B^\zeta R_\zeta + B^\theta R_\theta\right) \hat{R} + \left(B^\zeta Z_\zeta + B^\theta Z_\theta\right) \hat{Z} + RB^\zeta \hat{\phi} \tag{4.24}$$

$$\mathbf{N} = RZ_\theta \hat{R} - RR_\theta \hat{Z} + \left(R_\theta Z_\zeta - Z_\theta R_\zeta\right) \hat{\phi} \tag{4.25}$$

$$\mathbf{B} \times \mathbf{N} = \left(B_\theta R_\zeta - B_\phi R_\theta\right) \hat{R} + \left(B_\theta Z_\zeta - B_\phi Z_\theta\right) \hat{Z} + RB^\theta \hat{\phi} \tag{4.26}$$

with normalization coefficients

$$B^2 = \left(RB^\zeta\right)^2 + \left(B^\zeta R_\zeta + B^\theta R_\theta\right)^2 + \left(B^\zeta Z_\zeta + B^\theta Z_\theta\right)^2, \tag{4.27}$$

$$N^2 = R^2 \left(R_\theta^2 + Z_\theta^2\right) + \left(R_\theta Z_\zeta - Z_\theta R_\zeta\right)^2. \tag{4.28}$$

Using the expressions above, the final analytic expressions for the various magnetic geometry

terms can be calculated, as seen below. PyBalloon's geometry module evaluates these expressions using the metric and magnetic field information provided by the VMEC equilibrium input, resulting in fast and accurate calculations of the various 3D magnetic geometry terms.

Normal Components:

$$\begin{aligned}
\mathbf{N}\cdot\mathbf{x}_{\zeta\zeta} &= RZ_\theta R_{\zeta\zeta} - RR_\theta Z_{\zeta\zeta} - 2R_\zeta R_\zeta Z_\theta + 2R_\zeta R_\theta Z_\zeta - R^2 Z_\theta \\
\mathbf{N}\cdot\mathbf{x}_{\zeta\theta} &= RZ_\theta R_{\zeta\theta} - RR_\theta Z_{\zeta\theta} + R_\theta R_\theta Z_\zeta - R_\theta R_\zeta Z_\theta \\
\mathbf{N}\cdot\mathbf{x}_{\theta\theta} &= RZ_\theta R_{\theta\theta} - RR_\theta Z_{\theta\theta} \\
\mathbf{N}\cdot\mathbf{x}_{\phi} &= 0 \\
\mathbf{N}\cdot\mathbf{x}_{\theta} &= 0
\end{aligned} \tag{4.29}$$

Geodesic Components:

$$\begin{aligned}
\mathbf{B}\times\mathbf{N}\cdot\mathbf{x}_{\zeta\zeta} &= R_{\zeta\zeta}B_\theta R_\zeta - R_{\zeta\zeta}B_\zeta R_\theta + Z_{\zeta\zeta}B_\theta Z_\zeta - Z_{\zeta\zeta}B_\zeta Z_\theta + RR_\zeta B_\theta + RR_\theta B_\zeta \\
\mathbf{B}\times\mathbf{N}\cdot\mathbf{x}_{\zeta\theta} &= R_{\zeta\theta}B_\theta R_\zeta - R_{\zeta\theta}B_\zeta R_\theta + Z_{\zeta\theta}B_\theta Z_\zeta - Z_{\zeta\theta}B_\zeta Z_\theta + RR_\theta B_\theta \\
\mathbf{B}\times\mathbf{N}\cdot\mathbf{x}_{\theta\theta} &= R_{\theta\theta}B_\theta R_\zeta - R_{\theta\theta}B_\zeta R_\theta + Z_{\theta\theta}B_\theta Z_\zeta - Z_{\theta\theta}B_\zeta Z_\theta \\
\mathbf{B}\times\mathbf{N}\cdot\mathbf{x}_{\zeta} &= R_{\phi}B_\theta R_\zeta - R_{\phi}B_\zeta R_\theta + Z_{\phi}B_\theta Z_\zeta - Z_{\phi}B_\zeta Z_\theta + R^2 B_\theta \\
\mathbf{B}\times\mathbf{N}\cdot\mathbf{x}_{\theta} &= R_\theta B_\theta R_\zeta - R_\theta B_\zeta R_\theta + Z_\theta B_\theta Z_\zeta - Z_\theta B_\zeta Z_\theta
\end{aligned} \tag{4.30}$$

Normal Curvature:

$$\kappa_n = b^\zeta b^\zeta \left(\frac{\mathbf{N}\cdot\mathbf{x}_{\zeta\zeta}}{N}\right) + b^\theta b^\theta \left(\frac{\mathbf{N}\cdot\mathbf{x}_{\theta\theta}}{N}\right) + 2b^\zeta b^\theta \left(\frac{\mathbf{N}\cdot\mathbf{x}_{\zeta\theta}}{N}\right) \tag{4.31}$$

Geodesic Curvature:

$$\begin{aligned}
\kappa_g = {} & b^\zeta b^\zeta \left(\frac{\mathbf{B}\times\mathbf{N}\cdot\mathbf{x}_{\zeta\zeta}}{BN}\right) + b^\theta b^\theta \left(\frac{\mathbf{B}\times\mathbf{N}\cdot\mathbf{x}_{\theta\theta}}{BN}\right) + 2b^\zeta b^\theta \left(\frac{\mathbf{B}\times\mathbf{N}\cdot\mathbf{x}_{\zeta\theta}}{BN}\right) \\
& + \left[\left(\hat{b}\cdot\nabla\right) b^\zeta\right] \left(\frac{\mathbf{B}\times\mathbf{N}\cdot\mathbf{x}_{\phi}}{BN}\right) + \left[\left(\hat{b}\cdot\nabla\right) b^\theta\right] \left(\frac{\mathbf{B}\times\mathbf{N}\cdot\mathbf{x}_{\theta}}{BN}\right)
\end{aligned} \tag{4.32}$$

Normal Torsion:

$$\tau_n = b^\theta b_\zeta \left(\frac{\mathbf{N}\cdot\mathbf{x}_{\theta\theta}}{N}\right) - b^\zeta b_\theta \left(\frac{\mathbf{N}\cdot\mathbf{x}_{\zeta\zeta}}{N}\right) + \left(b^\zeta b_\zeta - b^\theta b_\theta\right)\left(\frac{\mathbf{N}\cdot\mathbf{x}_{\theta\zeta}}{N}\right) \tag{4.33}$$

4.3.3 Additional Details

The final modules included in PyBalloon are the data visualizer and the post-processing unit. The post-processing is useful for making comparisons between results from different equilibria as well as relating the ballooning stability to the 3D geometry. The data visualizer is a useful tool for viewing data from the input equilibrium, as well as the outputs from the geometry and ballooning modules. While these two modules have a standard setup, there is a lot of room for customization based on what the user is wanting to study.

4.4 The PB3D Code

The PB3D (Peeling-Ballooning in 3D) code[32] is a finite-n peeling-ballooning solver in active development for studying peeling-ballooning stability of both 2D and 3D equilibria. The code is meant to be complimentary to other peeling-ballooning solvers, such as the ELITE code [18], which focus on the stability of 2D equilibria. Similarly to ELITE, PB3D makes use of the edge-localized 3D peeling-ballooning model discussed in section 3.5, which takes the second order expansion of the ideal MHD energy principle with respect to the inverse toroidal mode number n^{-1}[33]. This model provides information on the growth rates and mode structures for ballooning and/or peeling driven instabilities.

A full overview of the PB3D code is given in references [32–34], with updates on the active development available from https://github.com/ToonWeyens/PB3D.

4.4.1 Model Summary

The PB3D model uses Euler minimization of the extended energy principle in the straight field line coordinate system to construct a set of second order ODEs for the normal mode functions $X_m(\psi)$ as defined in section 3.5. The code then looks to solve the set of equations given by

$$\sum_m \left\{ \bar{L}^0_{k,m} X_m - \left(\bar{L}^{1*}_{m,k} X_m \right)' + \bar{L}^1_{k,m} X'_m - \left(\bar{L}^2_{k,m} X'_m \right)' \right\} = 0 \tag{4.34}$$

and the surface contribution

$$\sum_m \left\{ \left(\delta^{vac}_{k,m} + \bar{L}^{1*}_{m,k} \right) X_m + \bar{L}^2_{k,m} X'_m \right\} = 0 \tag{4.35}$$

with the primes denoting normal derivatives, and $k, m = 1 \cdots M$, leading to M equations for the M functions X_m. Here, the operators $\bar{L}_{k,m}$ are given by the field line average values

$$\bar{L}_{k,m} = \int_\alpha \mathcal{J} e^{i(k-m)\theta} L_{k,m} \mathrm{d}\theta \tag{4.36}$$

along a given field line with label α, with the quantities $L_{k,m} = P_{k,m} - \omega^2 K_{k,m}$ given by

$$\begin{aligned}
P^0_{k,m} =& \frac{1}{\mu_0} \frac{|\nabla\psi|^2}{\mathcal{J}^2 B^2} \left(DU^{0*}_k - \mathcal{J} - \mu_0 \sigma \frac{\mathcal{J} B^2}{|\nabla\psi|^2} \right) \left(DU^0_k - \mathcal{J} - \mu_0 \sigma \frac{\mathcal{J} B^2}{|\nabla\psi|^2} \right) \\
& - \frac{\sigma}{\mathcal{J}} \left(\mathcal{J} S + \mu_o \sigma \frac{\mathcal{J} B^2}{|\nabla\psi|^2} \right) + \frac{(nq - mk(nq - m)}{\mu_0 \mathcal{J}^2 |\nabla\psi|^2} - 2p' \kappa_n \\
P^1_{k,m} =& \frac{1}{\mu_0} \frac{|\nabla\psi|^2}{\mathcal{J}^2 B^2} \left(DU^{0*}_k - \mathcal{J} - \mu_0 \sigma \frac{\mathcal{J} B^2}{|\nabla\psi|^2} \right) DU^1_m \\
P^2_{k,m} =& \frac{1}{\mu_0} \frac{|\nabla\psi|^2}{\mathcal{J}^2 B^2} DU^1_m DU^{1*}_k
\end{aligned} \tag{4.37}$$

and

$$\begin{aligned} K^0_{k,m} =& \frac{\rho}{|\nabla\psi|^2} + \frac{|\nabla\psi|^2}{B^2} U^{0*}_k U^0_k \rho \\ K^1_{k,m} =& \frac{|\nabla\psi|^2}{B^2} U^{0*}_k U^1_k \rho \\ K^2_{k,m} =& \frac{|\nabla\psi|^2}{B^2} U^{1*}_k U^1_k \rho \end{aligned} \tag{4.38}$$

where S is the magnetic shear, σ is the parallel current, and κ_n and κ_g are the normal and geodesic components of the curvature

$$\begin{aligned} S &= -\frac{1}{\mathcal{J}} \frac{\partial \Theta^\alpha}{\partial \theta} \\ \sigma &= \frac{\epsilon_{ijk}}{\mu_0} \frac{1}{\mathcal{J} B^2} \frac{\partial B_j}{\partial u^i} B_k \\ \kappa_n &= \frac{\nabla\psi}{|\nabla\psi|^2 B^2} \cdot \nabla_\perp \left(\mu_0 p + \frac{B^2}{2} \right) \\ \kappa_g &= -\frac{1}{2p'} \frac{1}{\mathcal{J}} \frac{\partial \sigma}{\partial \theta} \\ \Theta^i &= \frac{\nabla\psi \cdot \nabla u^i}{\nabla\psi \cdot \nabla\psi} \end{aligned} \tag{4.39}$$

and the quantities U^i_m, DU^i_m correspond to the geodesic component of the plasma perturbation minimized as a function of the normal component such that

$$\begin{aligned} U_m &= \left[U^0_m + U^1_m \frac{\mathrm{d}}{\mathrm{d}\psi} \right] X_m \\ DU^i_m &= \frac{\partial U^i_m}{\partial \theta} + i(nq - m) U^i_m \end{aligned} \tag{4.40}$$

and

$$\begin{aligned} U_m^0 =& -\left(\Theta^\alpha + q'\theta\right) \\ &+ \frac{i}{n}\frac{1}{B_\theta}\left[B_\alpha q' + \mathcal{J}\mu_0 p' + i(nq-m)\left(B_\alpha q'\theta - B_\psi\right)\right] \\ &+ \frac{i}{n}\frac{1}{B_\theta}\frac{nq-m}{n}\mathcal{J}\mathbf{B}\cdot\nabla\psi\times\nabla\left(\Theta^\theta e^{i(nq-m)\theta}\right)e^{-i(nq-m)\theta} \\ U_m^1 =& \frac{i}{n}\left(1+\frac{nq-m}{n}\frac{B_\alpha}{B_\psi}\right) \end{aligned} \tag{4.41}$$

Finally, the surface contribution (4.35) serves as the plasma-vacuum interface boundary condition to the plasma potential equations (4.34), with the $\delta_{k,m}^{vac}$ term being the contribution of the vacuum potential energy (3.159).

4.4.2 Discretization

The functions $X_m(\psi)$ in equations 4.34 is discretized using finite differences at J positions ψ_j to arbitrary order. This results in the solution vector $\mathbf{X}$ of size $J \times M$ with components $X_{mj} = X_m(\psi_j)e^{-im\theta}$. Discretization of the differential operators in equations 4.34 results in a generalized eigenvalue problem of the form

$$\mathbf{AX} = \lambda\mathbf{BX} \tag{4.42}$$

where the $\mathbf{A}$ and $\mathbf{B}$ matrices represent the potential and kinetic energy and $\lambda = \omega^2$ is the eigenvalue. If the discretization is done judiciously, $\mathbf{A}$ and $\mathbf{B}$ are Hermitian, so λ is real. Alternatively, the discrete Lagrangian $\mathbf{L} = \mathbf{A} - \lambda\mathbf{B}$ can be defined such that the generalized eigenvalue equation becomes

$$\mathbf{LX} = 0. \tag{4.43}$$

The PB3D code is setup to run with central or left finite differences of arbitrary order. To illustrate how the discretization is carried out, we consider the first order central differences

$$f^{(1)} = \frac{f_{j+1} - f_{j-1}}{\Delta} - \frac{\Delta^2}{6} f^{(3)} + \mathcal{O}(\Delta^4) \approx \frac{f_{j+1} - f_{j-1}}{\Delta} \tag{4.44}$$

with constant step size $\Delta = \psi_{j+1} - \psi_j$. This results in the matrix $\mathbf{L}$ being composed of a Hermitian stencil consisting of nine $(M \times M)$ blocks of the form

$$\begin{matrix} \frac{1}{4\Delta^4}\mathbf{L}_j^2 & \frac{-1}{2\Delta^2}\mathbf{L}_j^{1\dagger} & \frac{-1}{4\Delta^4}\mathbf{L}_j^2 \\ \frac{-1}{2\Delta^2}\mathbf{L}_j^1 & \mathbf{L}_j^0 & \frac{1}{2\Delta^2}\mathbf{L}_j^1 \\ \frac{-1}{4\Delta^4}\mathbf{L}_j^2 & \frac{1}{2\Delta^2}\mathbf{L}_j^{1\dagger} & \frac{1}{4\Delta^4}\mathbf{L}_j^2 \end{matrix} \tag{4.45}$$

superimposed along the diagonal. The first and last positions ($j = 1$ and $j = J$) of the matrix $\mathbf{L}$ are modified to account for the boundary conditions. The core boundary condition at the initial position assumes the perturbation goes to zero by setting the first row and column of the matrices to

$$\mathbf{A}_{ij} = \begin{cases} \mathbb{1}\lambda_{BC}, & \text{if } i = j = 1 \\ 0, & \text{otherwise} \end{cases} \qquad \mathbf{B}_{ij} = \begin{cases} \mathbb{1}, & \text{if } i = j = 1 \\ 0, & \text{otherwise} \end{cases} \tag{4.46}$$

where the artificial eigenvalue λ_{BC} has been introduced. For the edge boundary condition, the stencil is modified using the surface Euler equations (4.35) giving

$$\begin{matrix} 0 & \frac{1}{2\Delta^2}\delta^{vac} & 0 \\ \frac{1}{2\Delta^2}\delta^{vac} & \mathbf{L}_J^{0,mod} & 0 \\ 0 & 0 & 0 \end{matrix} \tag{4.47}$$

where

$$\mathbf{L}_J^{0,mod} = \mathbf{L}_J^0 - \left(\mathbf{L}_J^1 + \delta^{vac}\right)\left(\mathbf{L}_J^2\right)^{-1}\left(\mathbf{L}_J^1 + \delta^{vac}\right)^{\dagger}. \tag{4.48}$$

While PB3D can handle finite differences of arbitrary order, standard operation makes use of a third order finite difference scheme to achieve sufficient numerical accuracy. Additionally, either a left or central finite difference scheme is used, though the left scheme has been found to provide better convergence at the plasma-vacuum boundary.

4.4.3 Code Design and Implementation

The PB3D code is designed in a modular way, creating a clean workflow and allowing for easy customization to specific problems. The general layout of the code is given in figure 4.2. The code makes use of four major components: the input driver, the equilibrium driver, the perturbation driver, and the solution driver. The drivers function independent from one another, making use of optimized HDF5 channels to efficiently manage the data between components.

The input driver is used to pre-process the input equilibrium along with other code inputs, constructing the basic data structures used throughout the code. Currently, PB3D can read both 2D HELENA and 3D VMEC equilibria, though additional equilibrium input sources could be easily added. From there, the equilibrium and perturbation calculations are performed separately on independent meshes, minimizing the overall computational resources needed. Finally, the solution driver handles the final matrix construction and utilizes the optimized numerical tools SLEPC[35] and STRUMPACK[36] to solve the matrix equation with appropriate boundary conditions.

In addition to these drivers, PB3D makes use of the Richardson extrapolation technique [37] to minimize memory usage while achieving good convergence. The technique makes use of explicit knowledge of the discretization scheme to get better approximations of the numerical integrals for the field line averages.

Finally, the PB3D code contains a standalone module POST which is used for post-processing the output. Most notable of the post-processing options it the energy reconstruction, which makes use of the calculated eigenvector to calculate the individual terms that contribute to

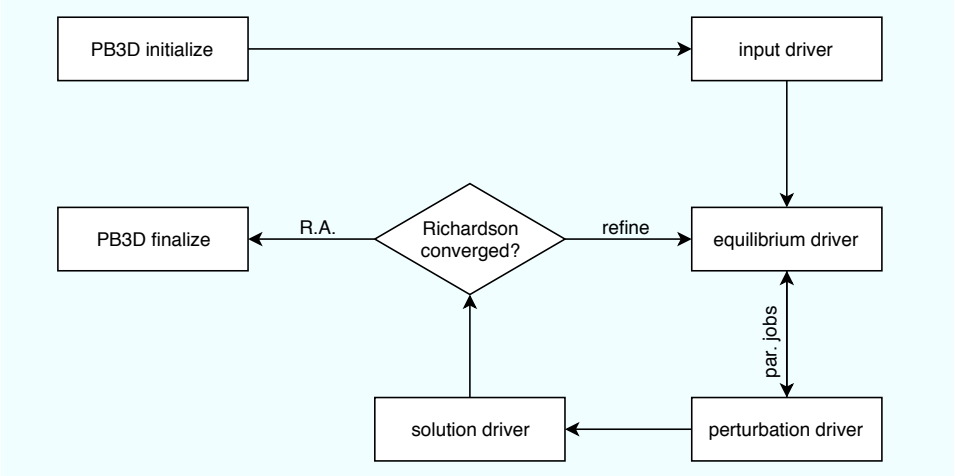

FIGURE 4.2: Workflow for PB3D

the plasma potential and kinetic energy. This allows for a check on consistency through comparison of the Rayleigh Quotient to the calculated eigenvalue, as well inspection of individual terms to gain insight into the instability itself, such as whether it is current or pressure driven.

4.5 PB3D Vacuum Boundary

The most recent addition to the PB3D code was the complete implementation of the perturbed vacuum potential energy as a part of the boundary condition at the plasma-vacuum interface. Prior to this, the boundary condition included only the surface contribution from the plasma potential energy minimization (see equation 3.166). However, the vacuum potential energy is critical for accurately modeling the edge peeling response, as the contribution from the vacuum can act to stabilize the peeling modes[38], With the addition of the vacuum response, PB3D should now be able to properly treat all high-n MHD instabilities, though testing with the new additions is still required.

The vacuum potential energy

$$\delta W_V(\mathbf{Q}_V) = \frac{1}{2}\int_V \mathrm{d}\mathbf{r}\left[\frac{|\mathbf{Q}_V|^2}{\mu_0}\right] \tag{4.49}$$

can be solved by representing the vacuum magnetic field perturbation $\mathbf{Q}_V$ in terms of the scalar potential ψ as

$$\mathbf{Q}_V = \nabla\phi \tag{4.50}$$

satisfying Laplace's equation

$$\nabla^2\phi = 0 \tag{4.51}$$

with boundary conditions at the plasma surface (s) and an imaginary wall infinitely far from the plasma (w) given by

$$\nabla\psi \cdot \nabla\phi = \begin{cases} \mathbf{B} \cdot \nabla X & \text{at } s \\ 0 & \text{at } w \end{cases} \tag{4.52}$$

where $X \equiv \nabla\psi \cdot \xi$ is the normal component of the perturbation ξ. Making use of the boundary conditions and vector identities, the entire vacuum potential energy can be expressed as

$$\delta W_v = -\frac{1}{2}\frac{1}{\mu_0}\int_s \mathcal{J}\left(\mathbf{B} \cdot \nabla X^*\right)\phi \mathrm{d}\theta \mathrm{d}\alpha \tag{4.53}$$

where the integration is only over the plasma surface, assuming the contribution from the infinite wall has vanished.

What remains is to relate the vacuum potential ϕ to its normal derivative $\nabla\psi \cdot \nabla\phi$. This is done using the boundary element method [39, 40], which allows calculation of the vacuum potential while considering only the boarder of the physical domain. While this acts to effectively reduce the dimensionality of the boundary calculations by one, it comes at the cost of introducing singular integrals that will require special treatment to be accurately and efficiently solved. The remainder of this section outlines the numerical model and implementation used to calculate the vacuum potential, including these singular integrals, as described by Weyens in [41], which was developed specifically for use in the PB3D code.

4.5.1 Boundary Element Method

The starting point for the boundary element method makes use of Green's second identity[42]

$$\int_v \left(a\nabla^2 b - b\nabla^2 a\right) \mathrm{d}V = \int_{\partial v} \left(a\nabla b - b\nabla a\right) \cdot \mathrm{d}\mathbf{S}. \tag{4.54}$$

The functions a and b are chosen, respectively, to be the unknown potential ψ to be solved and the Green's function for the Laplace operator ∇^2 centered at $\mathbf{r}_0$ given by $b = \frac{1}{|\mathbf{r}-\mathbf{r}_0|}$. Using this, the expression for the potential satisfying equation 4.51 becomes

$$-\beta\phi(\mathbf{r}_0) = \int \mathrm{d}\alpha \int \mathrm{d}\theta \frac{(-\mathcal{J}\nabla\psi)}{|\mathbf{r}-\mathbf{r}_0|} \cdot \left[\frac{\mathbf{r}-\mathbf{r}_0}{|\mathbf{r}-\mathbf{r}_0|^2}\phi + \nabla\phi\right] \tag{4.55}$$

where $-\mathcal{J}\nabla\psi$ is the outward normal vector, with the integration volume being complementary to the plasma volume, as indicated by the minus sign. The parameter β is the internal angle of the vacuum region between adjacent elements, allowing for a discontinuity in the direction of the normal on either side of the singular point. For a smooth boundary, the value of β is π, while a mesh covering toroidally shaped flux surfaces is more convex, resulting in $\beta > \pi$ on average[39, 43].

The integrals appearing in the boundary element method are solved by breaking them into small pieces and approximating the functions with polynomials on each of the subintervals. Specifically, the boundary is approximated by T linear pieces with the function values defined on the end points, resulting in T subintegrals collocated with the points $\mathbf{r}_i$ on the surface. The subintegrals can be evaluated using trapezoidal integration rules, with each of the collocation points getting a contribution from both adjacent subintegrals. This becomes more complicated for collocation points at or adjacent to singular values (i.e. $\mathbf{r}_i = \mathbf{r}_0$), which require special treatment.

The end result is a system of equation connecting the discrete function values $\phi_i \equiv \phi(\mathbf{r}_i)$ to their normal derivatives. The normal derivatives of ψ_i are related to the parallel derivative of the normal plasma potential as

$$\phi_i' = \mathcal{J}\nabla\psi \cdot \nabla\psi|_{\mathbf{r}_i} = \mathcal{J}\mathbf{B} \cdot \nabla X|_{\mathbf{r}_i} = \left.\frac{\partial X}{\partial\theta}\right|_{\mathbf{r}_i} \tag{4.56}$$

reducing equation 4.55 down to the system of equations[40]

$$\underline{H}\phi = \underline{G}\phi'. \tag{4.57}$$

In order to calculate the elements of the matrices $\underline{H}$ and $\underline{G}$, consider a subinterval j to $j+1$ for $j > i$ or $j+1 < i$. The function ϕ can be interpolated at every point θ with $\theta_j < \theta < \theta_{j+1}$ as

$$\phi = \phi_j \frac{\theta_{j+1} - \theta}{\theta_{j+1} - \theta_j} + \phi_{j+1} \frac{\theta - \theta_j}{\theta_{j+1} - \theta_j}. \tag{4.58}$$

The same is done for ϕ', as well as the factors $\tilde{G}_i$ and $\tilde{H}_i$, defined by

$$\begin{aligned} \tilde{G}_i(\theta) &= -\frac{1}{|\mathbf{r} - \mathbf{r}_i|} \\ \tilde{H}_i(\theta) &= \frac{\mathcal{J}\nabla\psi \cdot (\mathbf{r} - \mathbf{r}_i)}{|\mathbf{r} - \mathbf{r}_i|^3}, \end{aligned} \tag{4.59}$$

which then results in a formula for the subintegrals

$$\int_{\theta_j}^{\theta_{j+1}} \phi(\theta)\tilde{G}_i(\theta)\mathrm{d}\theta = \left[\phi_j \left(\frac{\tilde{G}_{i,j}}{3} + \frac{\tilde{G}_{i,j+1}}{6}\right) + \phi_{j+1}\left(\frac{\tilde{G}_{i,j}}{6} + \frac{\tilde{G}_{i,j+1}}{3}\right)\right]\Delta\theta \tag{4.60}$$

$$\int_{\theta_j}^{\theta_{j+1}} \phi(\theta)\tilde{H}_i(\theta)\mathrm{d}\theta = \left[\phi_j \left(\frac{\tilde{H}_{i,j}}{3} + \frac{\tilde{H}_{i,j+1}}{6}\right) + \phi_{j+1}\left(\frac{\tilde{H}_{i,j}}{6} + \frac{\tilde{H}_{i,j+1}}{3}\right)\right]\Delta\theta \tag{4.61}$$

where $\tilde{G}_{i,j} = \tilde{G}_i(\theta_j)$, $\tilde{H}_{i,j} = \tilde{H}_i(\theta_j)$. and $\Delta\theta = \theta_{j+1} - \theta_j$.

Using this results, the off-diagonal elements for the matrices $\underline{H}$ and $\underline{G}$ for $j = 1 \cdots i-1$ and $j = i+1 \cdots T$ are defined by

$$\begin{aligned} G_{i,j} &= \frac{1}{6}\tilde{G}_{i,j-1} + \frac{2}{3}\tilde{G}_{i,j} + \frac{1}{6}\tilde{G}_{i,j+1} \\ H_{i,j} &= \frac{1}{6}\tilde{H}_{i,j-1} + \frac{2}{3}\tilde{H}_{i,j} + \frac{1}{6}\tilde{H}_{i,j+1} \end{aligned} \tag{4.62}$$

where a constant of $\Delta\theta$ has been excluded for clarity. For the $j = i \pm 1$ terms, there is half the contribution from the above expression and half from the value of the singular element.

The diagonal elements G_{ii} and H_{ii}, as well as $G_{i,i\pm1}$ and $H_{i,i\pm1}$, require special treatment as they deal with the singular value. This is typically done using direct analytical integration at the singular point[39], but can also be treated with indirect methods[39, 40], which apply a known solution ϕ to the problem in order to get relations between the matrix elements. PB3D primarily utilizes the direct methods in calculating the diagonal matrix elements, though the indirect method is available for testing purposes. The complete calculation for the direct and indirect methods specifically used in PB3D (in both 2D and 3D) are excluded here for sake of brevity, as they are discussed at length in reference [41].

4.5.2 Numerical Implementation

Starting from equation 4.53 and making use of the boundary element formulation, the vacuum potential energy can be presented in a discrete matrix form as

$$\begin{aligned}\delta W_V &= -\frac{1}{2\mu_0}\sum_i I_i \frac{\partial X^*}{\partial \theta_i}\phi(\theta_i) \\ &= -\frac{1}{2\mu_0}\sum_{i,j} \frac{\partial X^*}{\partial \theta_i}\left[\underline{I}\underline{\underline{H}}^{-1}\underline{\underline{G}}\right]_{i,j}\frac{\partial X}{\partial \theta_j}\end{aligned} \tag{4.63}$$

using 4.56 and 4.57, with $\underline{I}$ being the diagonal matrix with elements $[\underline{I}]_{ii} = I_i$ coming from the trapezoidal integration rule

$$I_i = \begin{cases} \frac{\theta_{i+1}-\theta_{i-1}}{2} & for \quad i = 2\cdots T-1 \\ \frac{\theta_2-\theta_1}{2} & for \quad i = 1 \\ \frac{\theta_T-\theta_{T-1}}{2} & for \quad i = T \end{cases} \tag{4.64}$$

where T is the number of points in the θ grid.

The θ-dependence of X introduces a factor $(nq-m)(nq-k)$ for every (k,m) mode number pair, as well as an exponential

$$e^{i[(nq-m)\theta_j-(nq-m)\theta_i]} \tag{4.65}$$

for every pair of points (θ_i, θ_j). Excluding the leading factor $\frac{-1}{2\mu_0}$, the vacuum potential yields the scalar value

$$X_k^*(nq-k)\left(\sum_{i,j} e^{-i(nq-k)\theta_i}\left[\underline{I}\underline{H}^{-1}\underline{G}\right]_{ij} e^{i(nq-m)\theta_j}\right)(nq-m)X_m \tag{4.66}$$

for the combination of mode numbers (k,m), which can be written in matrix notation as

$$X_k^*(nq-k)\underline{E}_k^*\underline{I}\underline{H}^{-1}\underline{G}\underline{E}_m(nq-m)X_m \tag{4.67}$$

with $\underline{E}_m$ being a diagonal matrix with elements $[\underline{E}_m]_{jj} = e^{i(nq-m)\theta_j}$.

In order to solve this problem, first consider the solution vector $\mathbf{C}$ to the linear system of equations

$$\underline{H}\mathbf{C} = \underline{G}\underline{E}_m \tag{4.68}$$

which is then left-multiplied by $\underline{E}_k^*$ and a factor $(nq-k)(nq-m)$. This can be extended to all combinations of mode numbers (k,m) by forming the column vector $\mathbf{E}_m$ from the diagonal matrix. Columns are then added for each mode number m (including factors of $nq-m$), resulting in the system

$$\underline{E}\underline{P} \tag{4.69}$$

with $\underline{\underline{P}}$ being the diagonal matrix with elements $P_{jj} = nq - m_j$ and $\underline{\underline{E}}$ being the generally non-square matrix

$$\underline{\underline{E}} = \begin{bmatrix} e^{i(nq-m_1)\theta_1} & e^{i(nq-m_2)\theta_1} & \dots & e^{i(nq-m_M)\theta_1} \\ e^{i(nq-m_1)\theta_2} & e^{i(nq-m_2)\theta_2} & \dots & e^{i(nq-m_M)\theta_2} \\ \dots & \dots & \ddots & \dots \\ e^{i(nq-m_1)\theta_T} & e^{i(nq-m_2)\theta_T} & \dots & e^{i(nq-m_M)\theta_T} \end{bmatrix} \tag{4.70}$$

with M being the number of modes.

The final solution can then be obtained by first solving for $\underline{C}$ in the linear system of equations

$$\underline{\underline{H}}\,\underline{C} = \underline{\underline{G}}\,\underline{\underline{E}}\,\underline{\underline{P}} \tag{4.71}$$

followed by left-multiplication of $\underline{C}$ by $\underline{\underline{P}}\,\underline{\underline{E}}^*\,\underline{\underline{I}}$.

Alternatively, as $\underline{\underline{G}}$ and $\underline{\underline{H}}$ are real square matrices of size $T \times T$ and independant of the mode numbers, it is possible to calculate the solution $\underline{C}$ of the linear system

$$\underline{\underline{H}}\,\underline{C} = \underline{\underline{G}} \tag{4.72}$$

before considering the mode numbers, and saving the results. Later, this is right-multiplied by the $T \times M$ matrix $\underline{\underline{E}}\,\underline{\underline{P}}$ and left-multiplied by the complex transpose of $\underline{\underline{I}}\,\underline{\underline{E}}\,\underline{\underline{P}}$.

References

[1]P. J. McCarthy, P. Martin, and W. Schneider, "The CLISTE Interpretive Equilibrium Code, IPP Report 5/85", IPP Rep. 5/85, 18 (1999).

[2]A. Mikhailovskii, G. Huysmans, W. Kerner, and S. Sharapov, "Optimization of computational mhd normal-mode analysis for tokamaks", Plasma Physics Reports **23**, 844–857 (1999).

[3]S. P. Hirshman and J. C. Whitson, "Steepest-descent moment method for three-dimensional magnetohydrodynamic equilibria", Phys. Fluids **26**, 3553–3568 (1983).

[4]L. L. Lao, H. S. John, R. D. Stambaugh, A. G. Kellman, and W. Pfeiffer, "Reconstruction of current profile parameters and plasma shapes in tokamaks", Nucl. Fusion **25**, 1611–1622 (1985).

[5]L. L. Lao, H. E. S. John, Q. Peng, J. R. Ferron, E. J. Strait, T. S. Taylor, W. H. Meyer, C. Zhang, and K. I. You, "Mhd equilibrium reconstruction in the diii-d tokamak", Fusion Science and Technology **48**, 968–977 (2017).

[6]J. Ferron, M. Walker, L. Lao, H. S. John, D. Humphreys, and J. Leuer, "Real time equilibrium reconstruction for tokamak discharge control", Nuclear Fusion **38**, 1055–1066 (1998).

[7]K. Lackner, "Computation of ideal med equilibria", Comput. Phys. Commun. **12** (1976).

[8]S. P. Hirshman and D. K. Lee, "MOMCON: A spectral code for obtaining three-dimensional magnetohydrodynamic equilibria", Comput. Phys. Commun. **39**, 161–172 (1986).

[9]S. K. Seal, S. P. Hirshman, A. Wingen, R. S. Wilcox, M. R. Cianciosa, and E. A. Unterberg, "Parvmec: an efficient, scalable implementation of the variational moments equilibrium code", in (2016), pp. 618–627.

[10]S. A. Lazerson, J. Loizu, S. Hirshman, and S. R. Hudson, "Verification of the ideal magneto-hydrodynamic response at rational surfaces in the VMEC code", Phys. Plasmas **23**, 012507 (2016).

[11]R. S. Wilcox, A. Wingen, M. R. Cianciosa, N. M. Ferraro, S. P. Hirshman, C. Paz-Soldan, S. K. Seal, M. W. Shafer, and E. A. Unterberg, "Modeling of 3D magnetic equilibrium effects on edge turbulence stability during RMP ELM suppression in tokamaks", Nucl. Fusion **57**, 10.1088/1741-4326/aa7bad (2017).

[12]A. Wingen et al., "Connection between plasma response and resonant magnetic perturbation (RMP) edge localized mode (ELM) suppression in DIII-D", Plasma Phys. Control. Fusion **57**, 104006 (2015).

[13]C. R. Sovinec, T. A. Gianakon, E. D. Held, S. E. Kruger, and D. D. Schnack, "NIMROD: A computational laboratory for studying nonlinear fusion magnetohydrodynamics", Phys. Plasmas **10**, 1727–1732 (2003).

[14]PPPL, *M3d-c1* ((accessed October 2020)).

[15]R. Hazeltine and J. Meiss, *Plasma confinement* (Dover Publications, Inc., 2003).

[16]R. Sanchez, S. Hirshman, J. Whitson, and A. Ware, "Cobra: an optimized code for fast analysis of ideal ballooning stability of three-dimensional magnetic equilibria", Journal of Computational Physics **161**, 576–588 (2000).

[17]C. Ham, I. Chapman, A. Kirk, and S. Sarrelma, "Modelling of three dimensional equilibrium and stability of mast plasmas with magnetic perturbations using vmec and cobra", Physics of Plasmas **21**, 102501 (2014).

[18]H. R. Wilson, P. B. Snyder, G. T. A. Huysmans, and R. L. Miller, "Numerical studies of edge localized instabilities in tokamaks", Physics of Plasmas **9**, 1277–1286 (2002).

[19]A. Mikhailovskii, "Generalized mhd for numerical stability analysis of high-performance plasmas in tokamaks", Plasma Phys. Control. Fusion **40**, 1907–1920 (1998).

[20]G. Huysmans, S. Sharapov, A. Mikhailovskii, and W. Kerner, "Modeling of diamagnetic stabilization of ideal magnetohydrodynamic instabilities associated with the transport barrier", Physics of Plasmas **8**, 4292–4305 (2001).

[21]I. Chapman, S. Sharapov, G. Huysmans, and A. Mikhailovskii, "Modeling the effect of toroidal plasma rotation on drift-magnetohydrodynamic modes in tokamaks", Physics of Plasmas **13**, 062511 (2006).

[22]P. B. Snyder, H. R. Wilson, and X. Xu, "Progress in the peeling-ballooning model of edge localized modes: numerical studies of nonlinear dynamics", Physics of Plasmas **12**, 56115 (2005).

[23]L. Bernard, F. Helton, and R. Moore, "Gato: an mhd stability code for axisymmetric plasmas with internal separatrices", Computer Physics Communications **24**, 377 –380 (1981).

[24]A. Lunniss, H. Wilson, P. Snyder, T. Osborne, R. Groebner, K. Burrell, and X. Chen, "Enhancements to the ELITE code and application to QH-mode in DIII-D", 43rd EPS Conf. Plasma Physics, EPS 2016 (2016).

[25]M. Anastopoulos-Tzanis, B. Dudson, C. Ham, C. Hegna, P. Snyder, and H. Wilson, "Non-axisymmetric equilibrium and stability using the ELITE stability code", Nuclear Fusion **59**, 126028 (2019).

[26]G. Van Rossum and F. L. Drake, *Python 3 reference manual* (CreateSpace, Scotts Valley, CA, 2009).

[27]S. R. Hudson and C. C. Hegna, "Marginal stability boundaries for infinite-n ballooning modes in a quasiaxisymmetric stellarator", Phys. Plasmas **10**, 4716–4727 (2003).

[28]S. R. Hudson and C. C. Hegna, "Criteria for second stability for ballooning modes in stellarators", Phys. Plasmas **11**, L53–L56 (2004).

[29]S. R. Hudson, C. C. Hegna, and N. Nakajima, "Influence of pressure-gradient and shear on ballooning stability in stellarators", Nucl. Fusion **45**, 271–275 (2005).

[30]T. M. Bird and C. C. Hegna, "A model for microinstability destabilization and enhanced transport in the presence of shielded 3D magnetic perturbations", Nucl. Fusion **53**, 10.1088/0029-5515/53/1/013004 (2013).

[31]T. M. Bird and C. C. Hegna, "Controlling tokamak geometry with three-dimensional magnetic perturbations", Phys. Plasmas **21**, 10.1063/1.4898064 (2014).

[32]T. Weyens, R. Sánchez, G. Huijsmans, A. Loarte, and L. García, "PB3D: A new code for edge 3-D ideal linear peeling-ballooning stability", J. Comput. Phys. **330**, 997–1009 (2017).

[33]T. Weyens, R. Sánchez, L. García, A. Loarte, and G. Huijsmans, "Three-dimensional linear peeling-ballooning theory in magnetic fusion devices", Phys. Plasmas **21**, 10.1063/1.4871859 (2014).

[34]T. Weyens, J. M. Reynolds-Barredo, and A. Loarte, "Computationally advantageous expressions for 3-D MHD stability", Comput. Phys. Commun. **242**, 60–71 (2019).

[35]V. Hernandez, J. E. Roman, and V. Vidal, "Slepc: a scalable and flexible toolkit for the solution of eigenvalue problems", ACM Trans. Math. Software **31**, 351–362 (2005).

[36]*Strumpack – structured matrices package, version 00*, 2014.

[37]S. A. RICHARDS, "Completed richardson extrapolation in space and time", Communications in Numerical Methods in Engineering **13**, 573–582 (1997).

[38]G. T. A. Huysmans, "External kink (peeling) modes in x-point geometry", Plasma Physics and Controlled Fusion **47**, 2107–2121 (2005).

[39]J. Katsikadelis, *Boundary elements: theory and applications* (Elsevier Science, 2002).

[40]C. Brebbia and P. Skerget, *Diffusion-convection problems using boundary elements* (Springer, 1984).

[41]T. Weyens, "Expressions for perturbed vacuum potential energy for 3D linear MHD stability", Phys. Plasmas **26**, 10.1063/1.5086538 (2019).

[42]W. A. Strauss, *Partial differential equations: an introduction, 2nd edition* (Wiley, NJ, Hoboken, 2007).

[43]L. Gual, M. Kögl, and M. Wagner, *Boundary element methods for engineers and scientists* (Springer, Berlin, Heidelberg, 2003).

Chapter 5

3D Ballooning Stability

5.1 Experimental Observations of Helically Localized Instabilities

The work in this chapter was motivated by a set of experiments on ASDEX Upgrade [1, 2]. The primary goal of the experiments was to study the plasma response to external magnetic perturbations with various techniques. This was done using the 16 in-vessel MP-coils in an $n = 2$ configuration, with the two sets of coils rotating in the same direction (rigid rotation). This configuration results in a slowly ($\sim 1Hz$) rotating plasma such that plasma diagnostics create a complete 3D mapping of the discharge (see figure 5.1).

In order to get accurate measurements of the 3D edge displacement, a number of high resolution edge diagnostics are used, including charge exchange recombination spectroscopy (CXRS) [3], the lithium beam diagnostic (LIB) [4], ECE, and ECE-imaging (ECE-I), which measure the ion temperature, electron density, and electron temperature, respectively [1]. Additionally, a poloidal array of magnetic probes is used for equilibrium reconstruction, plasma position control, and measurements of magnetic perturbations near the plasma edge. A complete overview of diagnostics, their positioning, and their interpretation is given in Ref. [1].

Figure 5.2 illustrates a typical discharge from this experimental set [2]. Magnetic perturbations are applied in up to two configurations (resonant and non-resonant in this case), and slowly varied to rotate the plasma (5.2a). As the plasma rotates, the perturbation of the edge

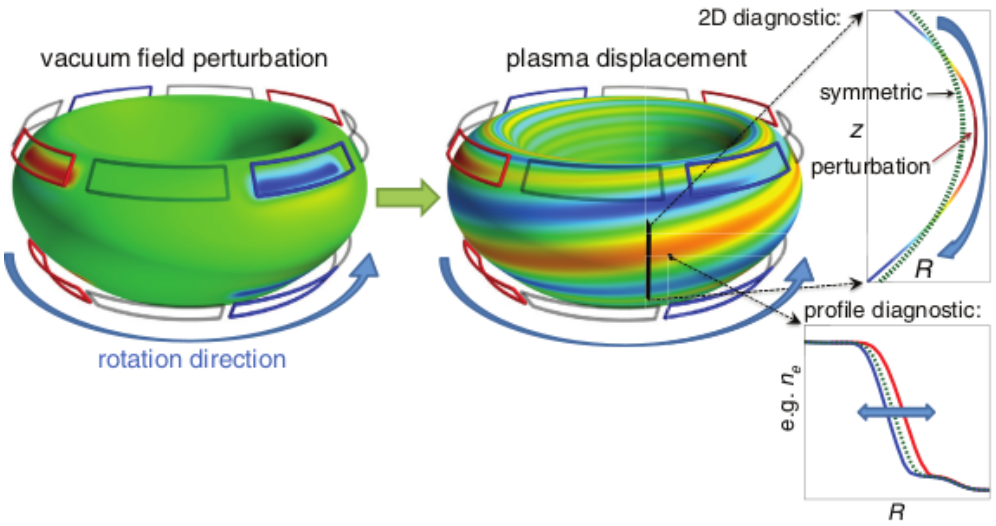

FIGURE 5.1: Cartoon of measuring the plasma displacement using a rigid rotating external MP-field. (left) external coils produce a MP of the vacuum field. (middle) this MP-field causes a perturbation of the flux surfaces. The color scaling of the surface plots indicates the magnetic perturbation B_r (left) and the surface perturbation ξ_r (middle). A rotation of the external MP-field results in a rotation of the displacement, which can be measured by an imaging system (top-right) or profile diagnostics (bottom-right). [1]

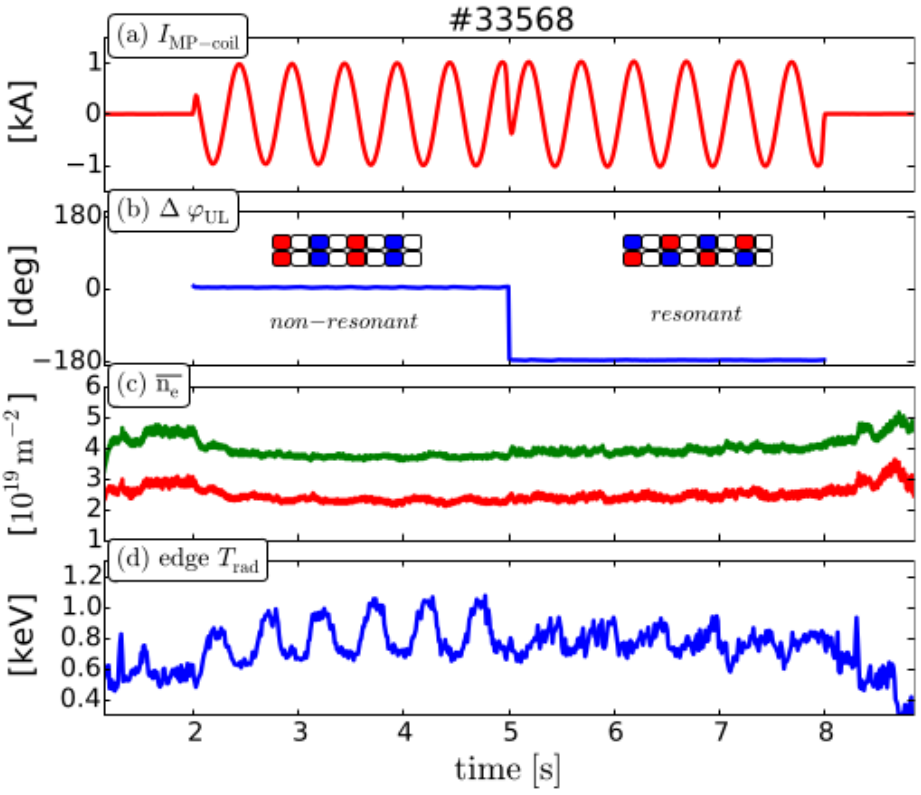

FIGURE 5.2: Overview of a typical discharge with rigid rotation: (a) Power supply current of one MP-coil illustrating the timing of the rigid rotation with 2 Hz , (b) the differential phase angle of two rotation phases employing vacuum non-resonant and resonant configuration, (c) line integrated density of a core (green) and edge chord (red) and (d) $T_{rad}(\approx T_e)$ from ECE in the pedestal around the LFS midplane. The modulation amplitude measured by ECE depends clearly on $\Delta\phi_{UL}$. [2]

density and temperature profiles are measured (5.2d) and the 3D plasma response is quantified. This process was repeated for a number of discharges, with the differential phase angle between the upper and lower coil sets ($\Delta\phi_{UL}$) varied.

The main goal of this project was to look at the plasma response as $\Delta\phi_{UL}$ was varied, and to compare these measurements of the boundary displacement to modeling using the VMEC code. Figure 5.3 shows the plasma response at the LFS-midplane measured with the various diagnostics, as well as calculated with the VMEC code, as $\Delta\phi_{UL}$ is varied [2]. The main results were that the peak plasma response is located near $\Delta\phi_{UL} = -90°$, which is between the resonant ($\Delta\phi_{UL} = -180°$) and non-resonant ($\Delta\phi_{UL} = 0°$). This has potential implications for current MP ELM studies, which tend to focus on the resonant response. Additionally, it was found that the VMEC modeling was sufficiently predicting the plasma response. A complete summary of these results can be found in Ref. [2].

Throughout these rigid rotation experiments, an instability was observed at certain toroidal phases. Figure 5.4 shows time traces of the measured relative amplitude $\delta T_{rad} / < T_{rad} >$, with $\delta T = T - < T >$, and $< T >$ being the mean temperature averaged over three periods [5]. In figure 5.4a, three rotational cycles are shown with the modulation from the rotating displacement emphasized by sinusoidal fits, with the locations of the ECE and ECE-I diagnostics resulting in a phases shift of approximately $\pi/2$ relative to the pitch of the field lines. Multiple ELM crashes are visible as sudden drops in the ECE signal.

When field lines with specific 3D geometry pass the diagnostics, high-frequency modes are observed. These modes develop at different times in the ECE and ECE-I diagnostics, but at the same toroidal phase with respect to the rigid rotation. Furthermore, the instabilities occur between ELM crashes, only when the modulation crosses zero from positive to negative values (see figure 5.4c-f). It is concluded from this that only a few toroidally localized field lines are unstable in the presence of the magnetic perturbation and subsequent plasma response [5]. However, the cause of this localization was unknown, as the MHD instability drives should be comparable at both zero crossings, resulting in instability at both points. As

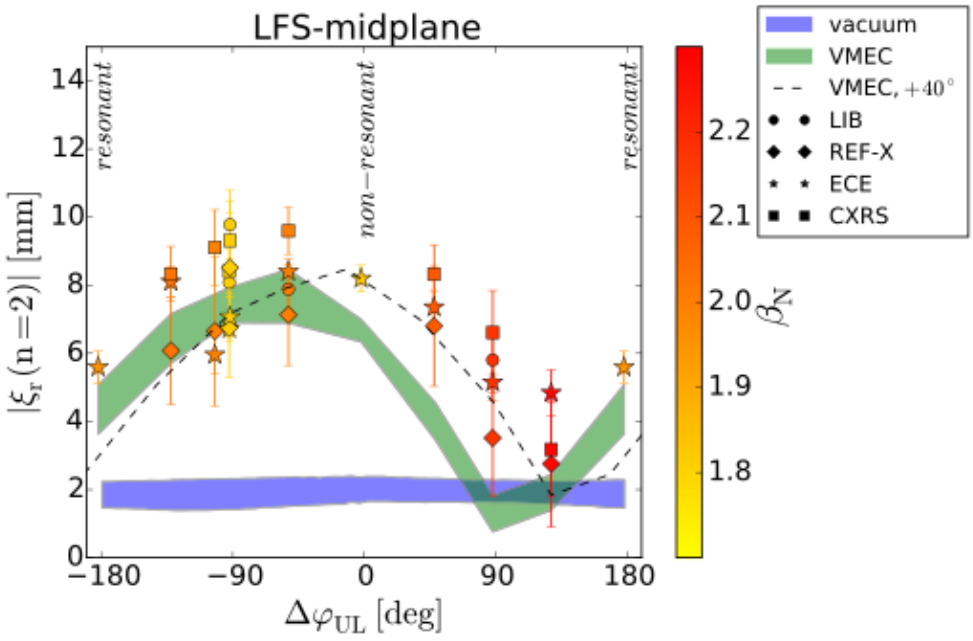

FIGURE 5.3: Amplitude of the $n = 2$ radial displacements versus $\Delta\phi_{UL}$. Each symbol is the measured displacement of one rigid rotation phase determined by one diagnostic. The color scaling indicates the measured β_N . The possible solutions using the vacuum field approximation and VMEC are indicated by blue and green shaded areas, respectively. The dashed line shows the maxima of the VMEC solutions shifted by 40°. Except for a shift of around 40°, VMEC and the measurements agree well. [2]

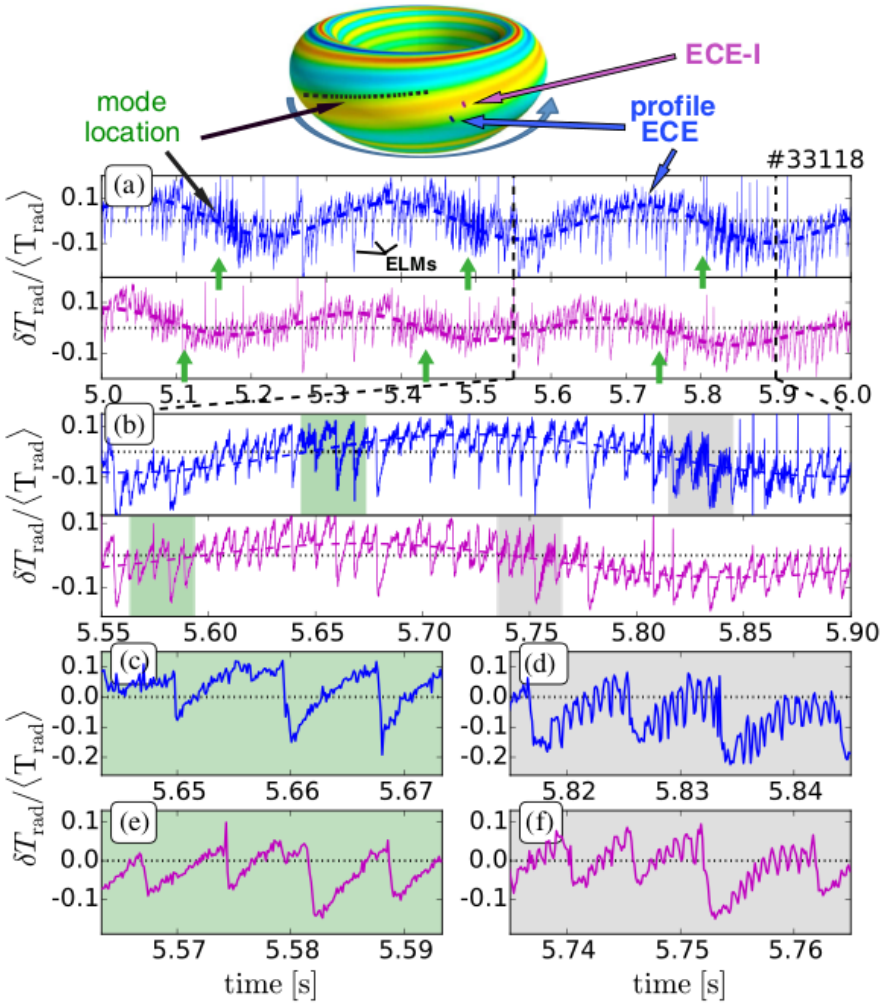

FIGURE 5.4: Time traces from profile ECE (blue) and ECE-I (purple) channels. Horizontal dotted lines indicate the zero line. Measuring principle and LOS positions are indicated at the top. (a) A 3 Hz modulation due to the rotating ξ_r ; (b) a MHD mode with $f \approx 1$ kHz is seen when one specific $\xi_r \approx 0$ — indicated by green arrows in (a) — passes the diagnostics. The mode appears in between ELM crashes and at only one $\xi_r \approx 0$ (d),(f), whereas at the other times not, e.g., (c),(e). Please note the different time ranges between (c)–(f) illustrated by shaded areas in (b). [5]

this is not the case, other factors must be considered in affecting the local stability, as will be the topic of the next section and Ref. [6].

Figure 5.5 provides more insight into the experimentally observed instabilities [7]. Magnetic measurements during rigid rotation also observe the localized instability discussed above. These measurements show the instabilities is poloidally localized to the LFS-midplane, with both radial and poloidal perturbations. Additionally, the mode propagates poloidally downwards, following the movements of the 3D geometry. Overall, the magnetic structure is useful for identifying the instability to be field line localized, saturated ideal ballooning modes [7]. This classification is important in developing the modeling performed in the next section.

Figure 5.5 also introduces a connection between the localized ballooning instability and the behavior of the mitigated ELMs. Looking at the magnetics on the LFS, ELMs are observed to be significantly stronger on field lines that are ballooning unstable[7]. This raises new questions into the relationship, if any, between the destabilizing of ballooning modes and ELM mitigation.

5.2 Modelling Helically Localized Ballooning Instabilities

Based on the results of the previous section, there was an unanswered question as to the cause of the toroidally localized ballooning instability that was observed. This motivated a theory based investigation into these types of discharges [6]. As these experiments were well diagnosed, with well tested 3D VMEC equilibrium having been created, they served as an excellent starting point for a theoretical exploration. The following section summarizes the results as presented in Reference [6].

Three sets of 2D CLISTE [8, 9] equilibrium reconstructions are generated based on the experimental discharges [1, 2]. The reconstructions have slightly varied q-profiles and pressure profiles to account for small variations between discharges. Figure 5.6 shows the pressure profile and q-profile for the three cases, which have β_N values of roughly 1.8 (red), 2.0 (blue),

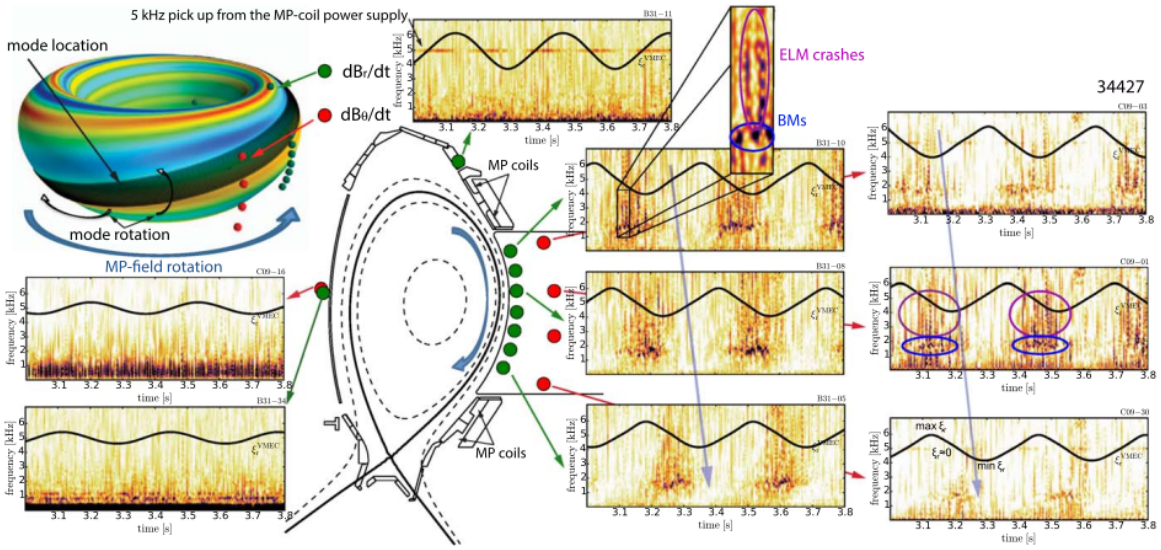

FIGURE 5.5: Spectrograms from magnetic measurements of radial (green balls/circles) and poloidal (red balls/circles) components during 3 Hz rigid rotation in the positive toroidal direction (blue arrows). The corresponding (closest) corrugations of the VMEC boundary are added as black solid lines in the spectrograms. Positions of the maximum and minimum ξ_r are exemplary marked in the right bottom corner. The color scaling is adjusted for the HFS and plasma top magnetic measurements to make weaker perturbations better visible. The corresponding positions are indicated in the poloidal cut and 3D plot. 2 kHz modes in the 3D geometry are primarily observed around the LFS midplane (ballooning modes (BMs), blue circles). Dark vertical stripes are magnetic perturbations from ELM crashes (magenta circles), which is indicated by the zoomed inset. The localisation of the modes is indicated by the black band in the 3D plot. The rotation direction of the BMs is indicated by black arrows. BMs and ELMs are strongest around the 'suspected' $\xi_r \approx 0$ at the LFS midplane. [7]

and 2.2 (green). All three of these equilibria have H-mode like pedestals, but different levels of bootstrap current which impacts the detailed shape of the q-profiles in the edge.

Using these 2D reconstructions as inputs, 3D equilibria were created with a free boundary version of VMEC [10, 11]. A total of 27 3D VMEC equilibria were generated from the three different input equilibria using nine values for the differential phase configurations ($\Delta\varphi_{UL}$). In these cases, the variation of $\Delta\varphi_{UL}$ acts as a proxy for the magnitude of 3D displacement of the plasma boundary and is used for more direct comparison to the experimental observations [2]. Figure 5.6 also shows the plasma displacement at the q_{95} surface for the $\beta_N \approx 2.2$, $\Delta\varphi_{UL} = -93^\circ$ equilibrium. The largest displacements occur when $\Delta\varphi_{UL} \approx -90^\circ$ for both the experiment and VMEC equilibria.

The various VMEC equilibria were studied using ideal MHD ballooning theory (section 3.3) using the PyBalloon code (section 4.3). Results from these studies are presented in the following sections.

5.2.1 Localization of the ballooning instability

Ballooning analysis — performed using the PyBalloon code in section 4.3 — show the ASDEX equilibria to have strong radial and toroidal localization of the ballooning instability. Figure 5.7 shows the ideal ballooning growth rates for 3D equilibrium of Shot 33345 with $\Delta\varphi_{UL} = -93^\circ$ throughout the (α, ψ, θ_k) phase-space. The most unstable point is observed at $\sqrt{\psi/\psi_a} = 0.945$ and $\theta_k = 0.22\pi$ for the $\alpha = 0.51\pi$ field line.

The axisymmetric equilibria is predicted to be stable throughout the pedestal region. This is due to the weak or negative magnetic shear allowing for access to the secondary stability region of ballooning theory [12]. With the application of magnetic perturbations, the instability appears radially localized at the top of the edge pedestal, as seen in figure 5.7a, matching the experimentally measured radial location of the instability. Figure 5.7b demonstrates how the radial wavenumber, θ_k, is localized for the 3D system, with the typical ballooning behavior of 3D MHD equilibria described in Ref. [13].

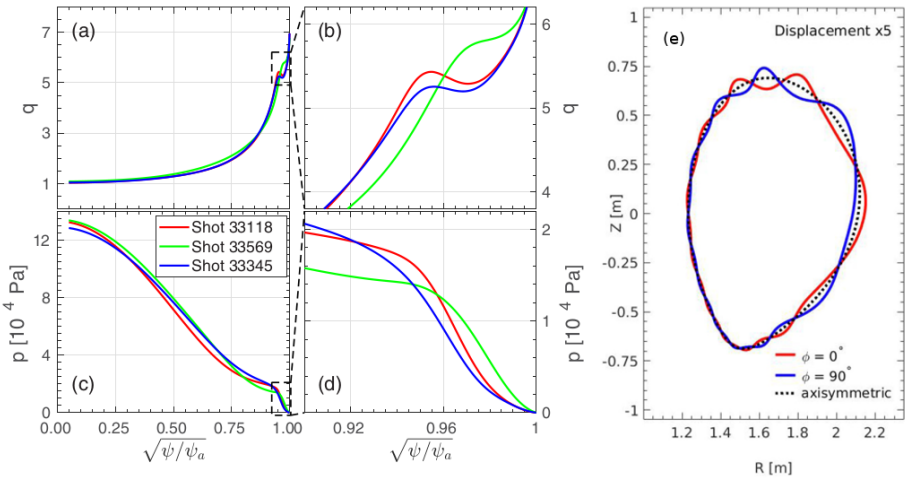

FIGURE 5.6: ASDEX Upgrade derived 2D H-mode profiles for ((a) and (b)) q and ((c) and (d)) the pressure from CLISTE. (b) and (d) Show the profiles in the edge pedestal region where the ballooning modes are located. (e) Edge displacement of the $\psi = 0.95$ flux surface for Shot 33345 equilibrium with $\Delta\phi_{UL} = -93°$. The displacement is largest on the low-field side of the discharge.

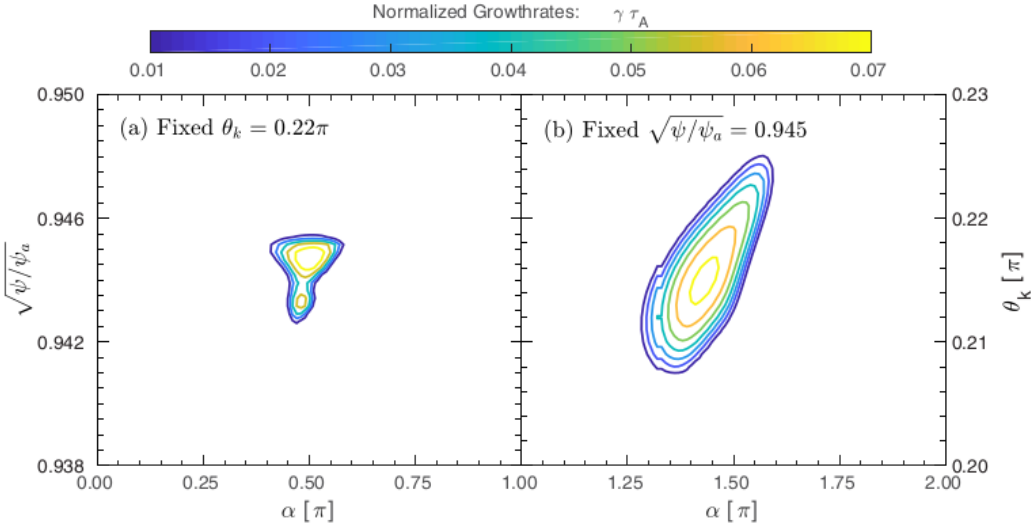

FIGURE 5.7: Ideal ballooning growth rates for Shot 33345 equilibrium with $\Delta\phi_{UL} = -93°$. (a) Varied ψ and α with fixed $\theta_k = 0.22\pi$ and (b) varied θ_k and α with fixed $\psi/\psi_a = 0.945$.

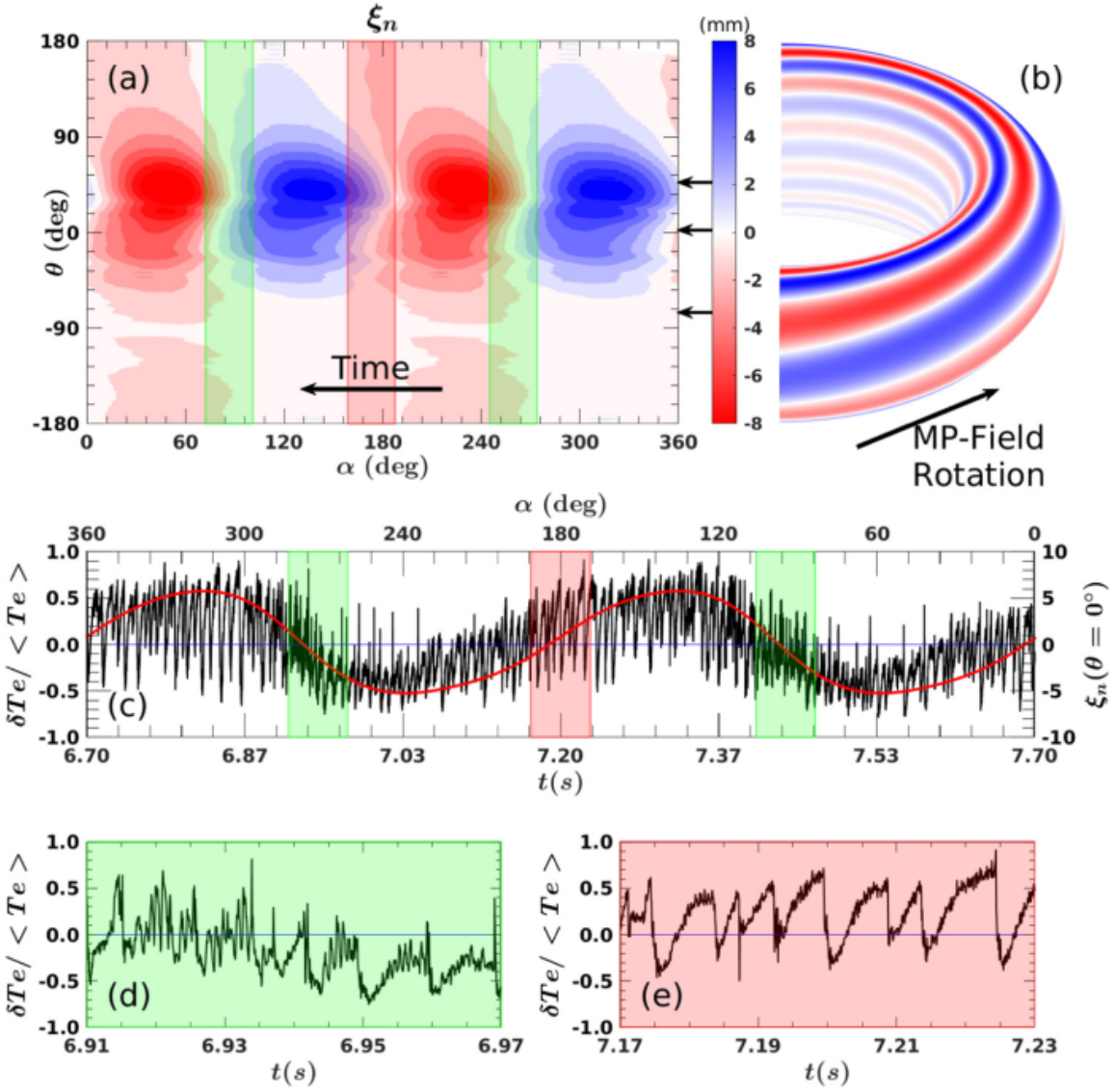

FIGURE 5.8: Normal plasma displacement on (a) the unfolded and (b) toroidal flux surface at $\psi/\psi_a = 0.945$. (c) Displacement (red) overlayed on the ECE data for Shot 33345. Green and red boxes denote the most unstable and most stable regions (respectively), all located at zero crossings of the displacement based on computational results with (d) and (e) showing close up of the ECE data for these regions. Figure (a) utilizes straight field line coordinates, with the X-point ($\theta = -75.4°$), outboard mid-plane ($R_{max}, \theta = 2.45°$), and plasma top ($Z_{max}, \theta = 46.6°$) identified by the arrows to the right of the top figure.

The toroidal localization of the mode under 3D magnetic perturbation is also observed in Figure 5.7. The ballooning growth rates are observed to have a significant dependence on the field line label, α. The instability is seen to be $N = 2$ periodic, matching the behavior of the 3D kink response. As the instability is enhanced at only a few toroidal angles, we can assert that the changes in 3D shaping have modified the local ballooning stability along specific bands of field lines, as seen in the experiment [5].

Calculations of the plasma displacement at the flux surface of interest are used to identify the position of the unstable field lines. Figure 5.8 shows the normal 3D plasma displacement from the MPs, ξ_n, on the unfolded axisymmetric flux surfaces in straight field line ballooning coordinates, as well as a mapping of the unstable field line for the given surface. The instability localizes to the same zero-crossing in ξ_n as observed in the experiment. This is seen in the 2D plots for figure 5.8, which show the localization of the eigenvalues, as well as the time trace of the ECE diagnostic from the experiment and the results of a synthetic ECE diagnostic for the computational data. The experimental data shows clear ballooning behavior with the same localization of the instability as we see in the computational results, all at the same location where the growth rates are toroidally localized [6].

Analysis has been carried out for all 27 equilibria provided. While details vary, the results of the case shown in Figure 5.7 are representative of all of the equilibria. The ballooning instability is localized in both radius and field line label indicating the effect of the 3D field is to locally distort the equilibrium so that only a few field lines are destabilized.

5.2.2 Growth rate dependence on differential phase of MP coils

The magnitude of 3D ballooning localization is seen to depend directly on the magnitude of the 3D corrugation at the unstable flux surface. Both the 3D displacement amplitude and the ballooning growth rate are found to increase with the differential phase of the perturbation coils, $\Delta\varphi_{UL}$. The relationship between the local growth rates and the displacement is best observed through direct comparison. Plotting the maximum growth rates against the maximum

local 3D displacement (Figure 5.9) shows a linear dependence of the growth rates on the 3D perturbation, as expected. However, we observe a minimum amount of 3D displacement (3 to 4 mm for these cases) is needed before the mode becomes unstable locally. This means the changes in the local 3D geometry need to be significant enough to modify the local stability properties of the plasma, the impact of which will be assessed in the following sections.

The growth rates for the highest-β case (Shot 33345) are seen to be greater than those of the lowest-β case (33118). However, the intermediate-β case (33569) shows a decrease in the ballooning growth rate beyond that expected from pressure gradient drive alone. This deviation can be attributed to the significantly decreased displacement when compared to the other two cases, further showing how closely the localization of the ballooning mode is tied to the 3D displacement amplitude and its associated changes to the geometry.

5.2.3 Energy dependence of the instability

Utilizing a δW-like formulation allows one to quantify the competition between the stabilizing and destabilizing contributions to the ballooning instability. The infinite-n ballooning equation is a simple 1D Sturm-Liouville equation, written as [13]

$$\frac{\partial}{\partial\theta}\left[P(\theta)\frac{\partial X}{\partial\theta}\right] + Q(\theta)X = -\lambda R(\theta)X \tag{5.1}$$

where the coefficient functions are defined as

$$P(\theta) = \frac{1}{\sqrt{g}}\frac{(1+\Lambda^2)}{|\nabla\psi|^2} \qquad Q(\theta) = \beta'\sqrt{g}\frac{(\kappa_n + \Lambda\kappa_g)}{|\nabla\psi|} \qquad R(\theta) = \sqrt{g}\frac{(1+\Lambda^2)}{|\nabla\psi|^2} \qquad \lambda = \omega^2 \tag{5.2}$$

The eigenvalue λ is related to the shape of the eigenfunction X through the equation

$$\lambda = \frac{\int_{-\infty}^{\infty} P(\theta)\left(\frac{\partial X}{\partial\theta}\right)^2 d\theta - \int_{-\infty}^{\infty} Q(\theta)X^2 d\theta}{-\int_{-\infty}^{\infty} R(\theta)X^2 d\theta}. \tag{5.3}$$

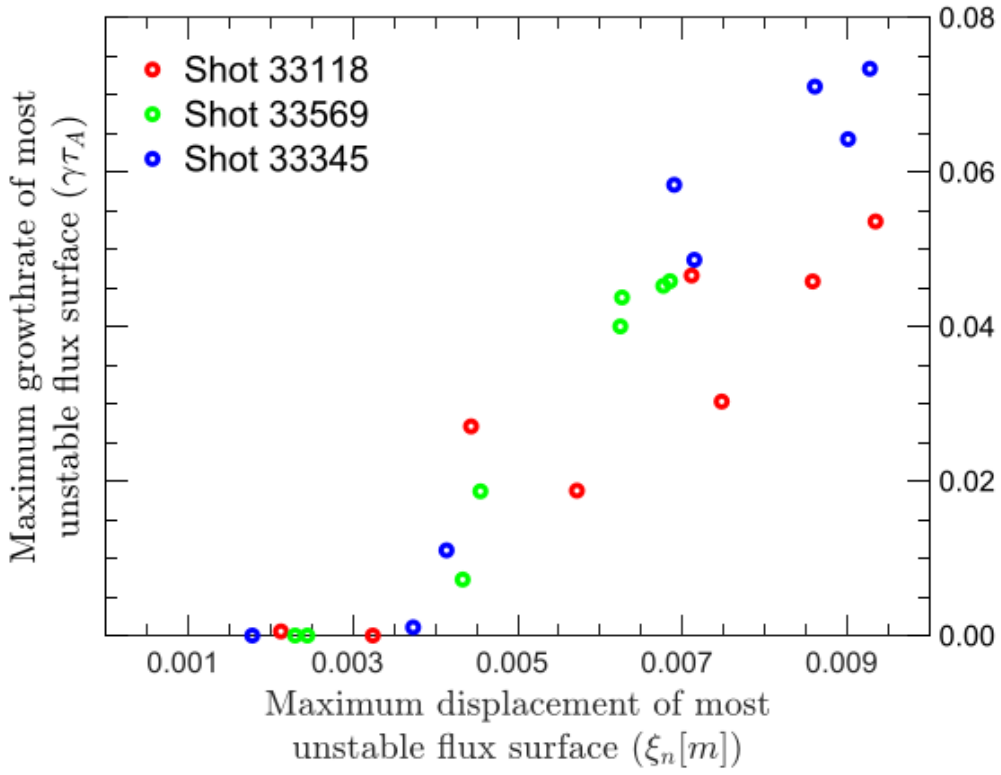

FIGURE 5.9: Dependence of the maximum ballooning growth rate on the maximum of the 3D displacement of the unstable flux surface.

Case	$\bar{W}_{LB}$	$\bar{W}_P$	$\bar{W}_{TOT}$
Axi	2.22	2.02	0.20
Stable	3.31	2.42	0.89
Unstable	1.70	1.71	-0.01

TABLE 5.1: Energy balance results

This shows that the growth rates are a balance between the stabilizing line-bending energy ($\bar{W}_{LB}$) and the destabilizing pressure-curvature potential ($\bar{W}_{PC}$)

$$\bar{W}_{LB} = \int_{-\infty}^{\infty} \delta W_{LB} d\theta = \int_{-\infty}^{\infty} P(\theta) \left(\frac{\partial X}{\partial \theta} \right)^2 d\theta \tag{5.4}$$

$$\bar{W}_{PC} = \int_{-\infty}^{\infty} \delta W_{PC} d\theta = \int_{-\infty}^{\infty} Q(\theta) X^2 d\theta \tag{5.5}$$

Evaluation of the energy terms, seen in table 5.1, shows how the 3D localization changes the available free energy leading to destabilization. The stabilizing line-bending energy is decreased along unstable field-lines, and increased for the stable field lines. The same behavior is seen in the driving energy, though the changes are significantly smaller, leading to a small number of field-lines having a surplus of free energy and thus go unstable.

The observed behavior in the mode energy provides us valuable insight into the mechanism behind the 3D destabilization of the ballooning instabilities. Both the drive and the stabilizing terms have a dependence on the integrated magnetic local shear (Λ), with the stabilizing term having a stronger (Λ^2) dependence, as seen in equation 5.2. We see that there is a large variation in the integrated local magnetic shear between the different field lines, clearly impacting the energy density terms. This demonstrates that the local magnetic shear is playing a key role in the localization of the ballooning instability.

5.2.4 Analysis of local 3D geometry on stability

The changes in the energy terms can be attributed to three terms (shown in figure 5.10): the normal curvature, the geodesic curvature, and the local magnetic shear. Here, the local magnetic shear and curvature are defined as

$$s_l = \hat{b} \times \hat{n} \cdot \nabla \times \left(\hat{b} \times \hat{n} \right), \tag{5.6}$$

and

$$\kappa = \hat{b} \cdot \nabla \hat{b} = \kappa_n \hat{n} + \kappa_g \hat{b} \times \hat{n}, \tag{5.7}$$

respectively [14]. Figures 5.10 (d-f) show the local 3D toroidal variation of the geometric quantities, calculated by taking the difference between each point and the toroidal mean, normalized by the difference in the maximum and minimum of the quantity in the poloidal direction. We see that the 3D shaping of the plasma boundary has the largest impact on the local magnetic shear on the low field side of the device, while the curvature terms see only small variation, mostly away from the low field side midplane. As we saw in figure 5.8, the instability is localized at $\alpha \approx 90°, 270°$. Figure 5.10f shows the local magnetic shear decreasing significantly on these field lines near $\theta \approx 30°$, while a significant increase in the local magnetic shear is observed on the $\alpha \approx 0°, 180°$ field lines, which are seen to have increased stability properties. Figure 5.10d shows changes in the normal curvature, but they are localized more to the top of the device. Figure 5.10e shows changes in the geodesic curvature on the low field side, but they are significantly smaller than the changes observed in the local magnetic shear.

This toroidal variation in the local magnetic shear drives the change in the destabilizing energy. Additionally, the stabilizing energy is entirely dependent on the square of the integrated local magnetic shear, explaining why the toroidal variation in the stabilizing term is more dramatic.

Having identified the changing local magnetic shear as the dominant mechanism in the localized destabilization of the mode, we look to analyze the physical quantities that contribute to these changes to better understand the underlying physical mechanism at work. To do this, we follow the work of [14], which breaks down the shear into two contributing factors as

$$s_l = \mu_0 \frac{\mathbf{J} \cdot \mathbf{B}}{B^2} - 2\tau_n, \tag{5.8}$$

where τ_n is the normal torsion, a purely geometric term, given by

$$\tau_n = -\hat{n} \cdot (\hat{b} \cdot \nabla)(\hat{b} \times \hat{n}). \tag{5.9}$$

and $\mathbf{J} \cdot \mathbf{B} / B^2$ is the local current density along the field line.

Examination of these terms (figure 5.11) shows that the dominate component to the local magnetic shear on the low field side is the normal torsion, while the contribution from the parallel current is smaller by comparison. This leads to the poloidal structure of the local magnetic shear to be determined predominantly by the normal torsion of the magnetic field.

Figure 5.11 also illustrates the toroidal variation of the components to the magnetic shear, where the local 3D variation the two shear terms are plotted. Here we see that the toroidal variation of both the parallel current and normal torsion are significant. The parallel current provides a moderate contribution to the shear, with a moderate decrease on the low-field side at the unstable field lines. However, this term is not aligned with the field lines, so its affect is reduced near the midplane. This is likely cause by the parallel current aligning to the field lines at the nearby dominant rational surface, which have a different shear than the most unstable flux surface shown. The normal torsion sees a large local increase on the unstable field lines near $\theta \approx 30^\circ$, which translates to the large decrease of the shear at that location.

While both components of the shear have toroidal variation, the contribution from the normal torsion is the more impactful on the localization of the instability. This is significant, as the normal torsion is dependent only on the local 3D magnetic geometry. This shows that the 3D shaping of the plasma itself is responsible for the changing stability properties along select field lines. This also helps explain why the instability is only observed at one of the zero-crossings of the 3D displacement: the direction of motion of the plasma boundary determines whether the normal torsion is increasing or decreasing locally, relative to the underlying local magnetic topology (seen in figure 5.11). In the stable case, the change cause the field lines to twist tighter, increasing the stored line-bending energy. In the unstable case, the field lines

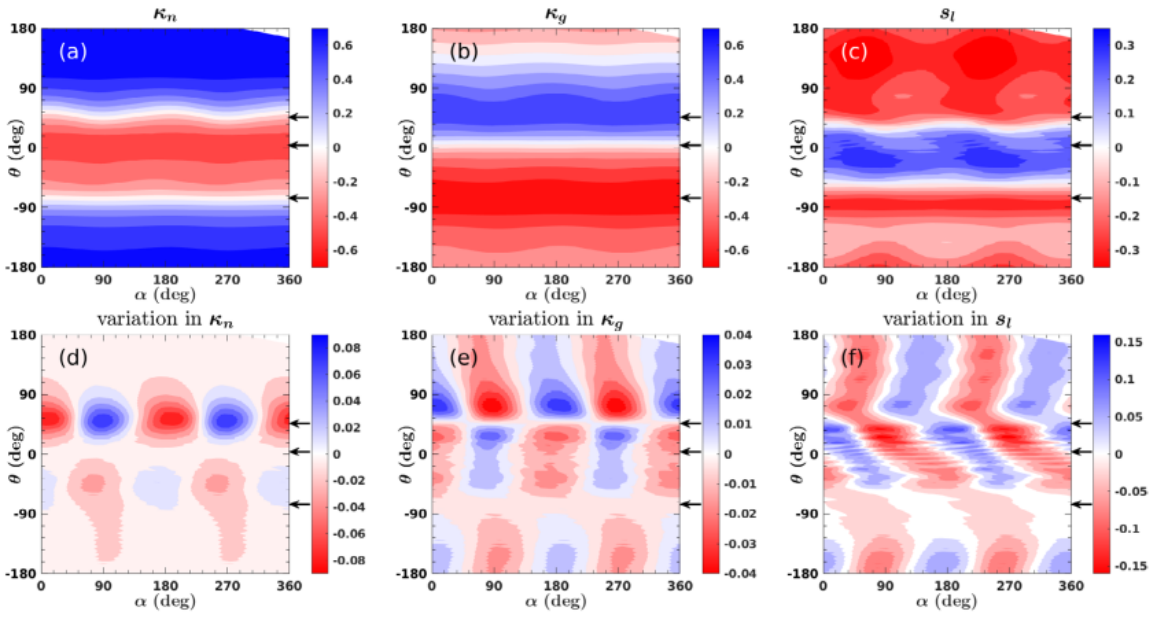

FIGURE 5.10: (a) Normal curvature, (b) geodesic curvature, and (c) local magnetic shear. (d)–(f) show the ratio of the toroidal to poloidal variation of the corresponding components in ((a)–(c)). All quantities are for Shot 33345 with $\Delta\phi_{UL} = -93^\circ$ plotted with the straight field line coordinates at $\psi/\psi_a = 0.945$. The arrows to the right of the figures show the X-point ($\theta = -75.4^\circ$), outboard mid-plane ($R_{max}, \theta = 2.45^\circ$), and plasma top ($Z_{max}, \theta = 46.6^\circ$).

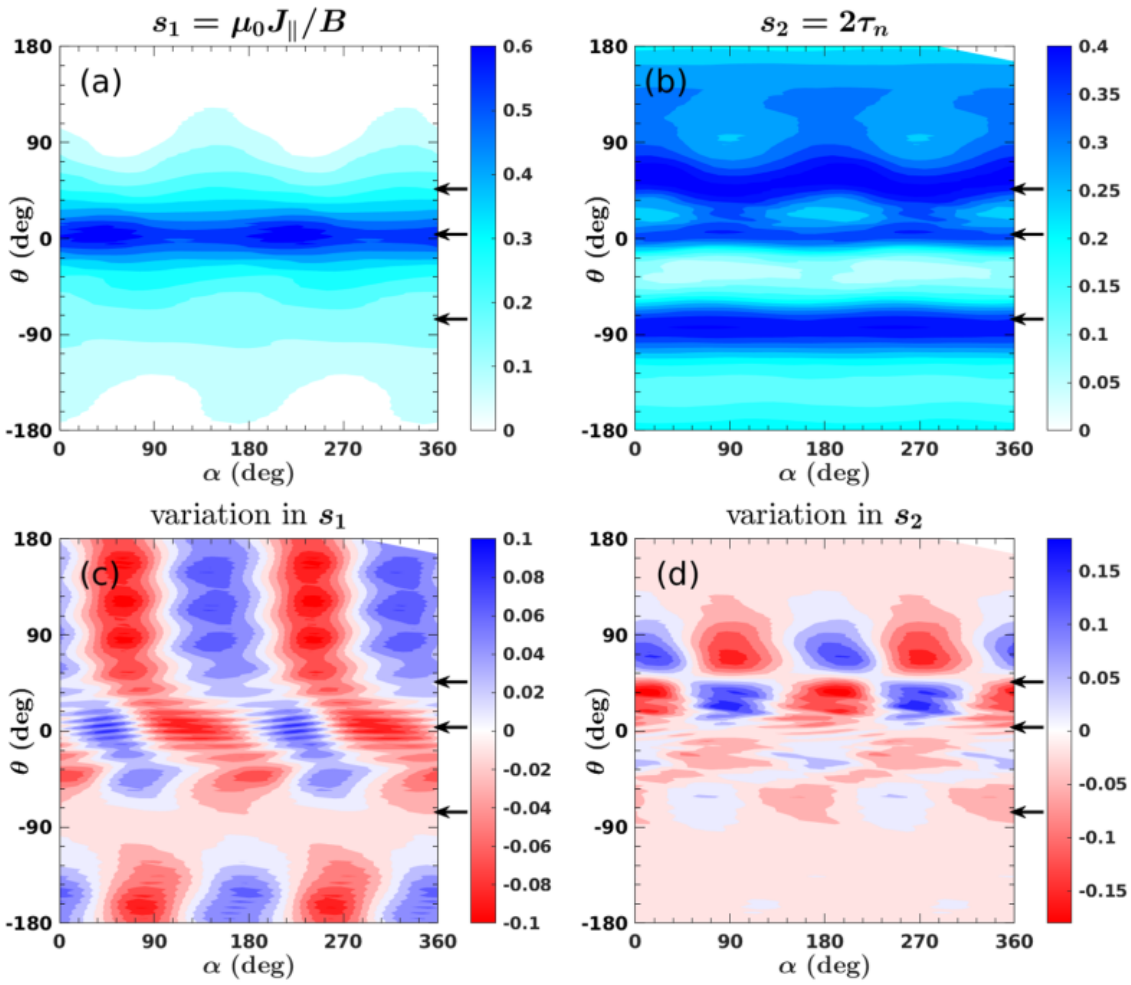

FIGURE 5.11: (a) Parallel current and (b) normal torsion contributions to the local magnetic shear ($s_l = s_1 - s_2$). ((c) and (d)) show the ratio of the toroidal to poloidal variation of the corresponding components in ((a) and (b)). All quantities are for Shot 33345 with $\Delta\phi_{UL} = -93^\circ$ plotted with the straight field line coordinates at $\psi/\psi_a = 0.945$. The arrows to the right of the figures show the X-point ($\theta = -75.4^\circ$), outboard mid-plane ($R_{max}, \theta = 2.45^\circ$), and plasma top ($Z_{max}, \theta = 46.6^\circ$).

unwind until there is a small region where they are locally viewed as non-bending, allowing the ballooning instability to occur. The amount of change require for the instability to arise is a matter of how close to the stability boundary the plasma is prior to application of the magnetic perturbations.

5.3 Summary

The presented experimental measurements in section 5.1 combined with the ideal MHD modeling of section 5.2 demonstrate the importance of the magnetic perturbation induced 3D magnetic geometry on the infinite-n ballooning stability in the tokamak pedestal region. It is found that the 3D magnetic perturbations destabilize ballooning modes localized to the zero-crossing in the plasma displacement (going from $\xi_{n,max}$ to $\xi_{n,min}$). While the modes localize near $|\xi_n| = 0$, the ballooning mode growthrates increase with absolute magnitude of the displacement, and a minimal amount of 3D perturbation is necessary to destabilize the equilibrium.

Analysis of the local 3D magnetic geometry shows that variation in the magnetic shear in response to the magnetic perturbations plays a critical role in the localized destabilization of the ballooning mode. More specifically, the edge kink response to the perturbations distorts the magnetic geometry near $\xi_n = 0$ such that the normal torsion τ_n (and subsequently the magnetic shear) changes. In the case of the unstable zero-crossing, the torsion is increased, reducing the magnetic shear and stabilizing line-bending energy below the point required to stabilize the ballooning mode. Conversely, the normal torsion decreases near the stable zero-crossing, moving farther away from the stability boundary, explaining why the ballooning modes are only observed for the $\xi_n = 0$ going from $\xi_{n,max}$ to $\xi_{n,min}$.

This same destabilizing mechanism could also deliver reasonable explanations for the increase in ELM frequency and the accompanied enhanced transport, the density 'pump-out', since the local magnetic shear can also influence additional curvature driven instabilities like

peeling-ballooning modes, kinetic ballooning modes and drift-waves[15–17]. Nevertheless, dedicated studies using 3D stability calculations are needed to pin down their role and the role of the 3D equilibrium, if any, in the mitigation/suppression.

References

[1]M. Willensdorfer et al., "Plasma response measurements of external magnetic perturbations using electron cyclotron emission and comparisons to 3D ideal MHD equilibrium", Plasma Phys. Control. Fusion **58**, 10.1088/0741-3335/58/11/114004 (2016).

[2]M. Willensdorfer et al., "Three dimensional boundary displacement due to stable ideal kink modes excited by external n = 2 magnetic perturbations", Nucl. Fusion **57**, 10.1088/1741-4326/aa7f4c (2017).

[3]E. Viezzer, T. Pütterich, R. Dux, and R. M. McDermott, "High-resolution charge exchange measurements at ASDEX Upgrade", Rev. Sci. Instrum. **83**, 103501 (2012).

[4]M. Willensdorfer, E. Wolfrum, R. Fischer, J. Schweinzer, M. Sertoli, B. Sieglin, G. Veres, and F. Aumayr, "Improved chopping of a lithium beam for plasma edge diagnostic at ASDEX Upgrade", Rev. Sci. Instrum. **83**, 023501 (2012).

[5]M. Willensdorfer et al., "Field-Line Localized Destabilization of Ballooning Modes in Three-Dimensional Tokamaks", Phys. Rev. Lett. **119**, 10.1103/PhysRevLett.119.085002 (2017).

[6]T. B. Cote, C. C. Hegna, M. Willensdorfer, E. Strumberger, W. Suttrop, and H. Zohm, "Helically localized ballooning instabilities in three-dimensional tokamak pedestals", Nucl. Fusion **59**, 10.1088/1741-4326/aaf01d (2019).

[7]M Willensdorfer et al., "Dynamics of ideal modes and subsequent ELM crashes in 3d tokamak geometry from external magnetic perturbations", Plasma Physics and Controlled Fusion **61**, 014019 (2018).

[8]P. J. McCarthy, P. Martin, and W. Schneider, "The CLISTE Interpretive Equilibrium Code, IPP Report 5/85", IPP Rep. 5/85, 18 (1999).

[9]P. J. Mc Carthy, "Identification of edge-localized moments of the current density profile in a tokamak equilibrium from external magnetic measurements", Plasma Phys. Control. Fusion **54**, 10.1088/0741-3335/54/1/015010 (2012).

[10]S. P. Hirshman and J. C. Whitson, "Steepest-descent moment method for three-dimensional magnetohydrodynamic equilibria", Phys. Fluids **26**, 3553–3568 (1983).

[11]E. Strumberger, S. Günter, and C. Tichmann, "MHD instabilities in 3D tokamaks", Nucl. Fusion **54**, 064019 (2014).

[12]J. Greene and M. Chance, "The second region of stability against ballooning modes", Nuclear Fusion **21**, 453–464 (1981).

[13]R. L. Dewar and A. H. Glasser, "Ballooning mode spectrum in general toroidal systems", The Physics of Fluids **26**, 3038–3052 (1983).

[14]C. C. Hegna, "Local three-dimensional magnetostatic equilibria", Phys. Plasmas **7**, 3921–3928 (2000).

[15]T. M. Bird and C. C. Hegna, "Controlling tokamak geometry with three-dimensional magnetic perturbations", Phys. Plasmas **21**, 10.1063/1.4898064 (2014).

[16]A. Kendl and H. Wobig, "Geometric effects on drift wave stability in advanced stellarators", Physics of Plasmas **6**, 4714–4721 (1999).

[17]G. Birkenmeier, M. Ramisch, B. Schmid, and U. Stroth, "Experimental evidence of turbulent transport regulation by zonal flows", Phys. Rev. Lett. **110**, 145004 (2013).

Chapter 6

The PB3D Code

6.1 Introduction

Building on the work from Chapter 5, the logical next-steps are to investigate the effects of 3D equilibria on peeling-ballooning stability and its resultant impact on ELM dynamics. Recent experiments have shown that 3D geometry does not only result in localized ballooning modes, but also influences the dynamics of the following ELM crash[1]. It is observed that the ELM filaments localize to the same 'bad' field lines as the preceding ballooning modes, meaning the 3D geometry may also play a key role in the ELM stability.

In order to investigate this, numerical tools that include a complete peeling-ballooning model for 3D equilibria are needed. However, current analysis tools are not well suited for handling the 3D equilibria necessary for studying this problem. The leading peeling-ballooning code, ELITE[2], has traditionally been limited to 2D axisymmetric equilibria — though work to expand ELITE to include 3D equilibria is underway[3]. Additionally, certain MHD codes like CAS3D[4] and M3D-C1[5] that can utilize 3D equilibria contain physics beyond the scope of the peeling-ballooning model. This adds a level of complexity in identifying the specific physical mechanisms at work, making them challenging tools to use for this problem.

A new numerical code PB3D — Peeling-Ballooning in 3D — has been developed specifically for this purpose [6]. PB3D makes use of high-n 3D edge peeling-ballooning theory similar to ELITE, but does not assume axisymmetry in the plasma equilibria being investigated. Instead, PB3D uses an updated formulation of the peeling-ballooning theory relying on tensorial calculus in curvilinear coordinates, as opposed to the pseudo-Cartesian treatment used with axisymmetric equilibria. Making use of a modified flux coordinate system and exploiting the fluted nature of the modes, the dimensionality of the problem is reduced, and the final model has the same mathematical complexity as the axisymmetric problem[7]. A full derivation and discussion of this 3D edge peeling-ballooning model is covered in Section 3.5.

However, development of PB3D is ongoing, with the code being largely untested. Previous benchmarking exercises focusing primarily on the ballooning stability problem with simple plasma geometries [6, 7]. For these studies, the pressure-curvature free energy source is the dominant drive for ideal MHD instabilities with global mode structures (as opposed to the local mode structure described in infinite-n ballooning theory) and hence is referred to as the "ballooning" case in the context of PB3D benchmarking activities. While these early proof of principle tests showed promising results, further testing using 2D and 3D equilibria with edge currents for peeling drive and more experimentally realistic geometries are needed. Additionally, the previous benchmarking did not account for the newly implemented vacuum perturbation boundary condition, so additional tests with the recent code additions are required.

The remainder of this chapter focuses on benchmarking of the PB3D code, now that the implementation of the vacuum perturbation boundary condition has been completed. Initial tests make use of the well studied CBM18 equilibrium, which has been successfully used in previous PB3D benchmarks[8]. The goal of this test is to identify unexpected changes, if any, from implementing the new boundary condition.

A second benchmarking exercise using equilibria based on ASDEX Upgrade Shot 34424 (A34424) is performed and is the first test of PB3D with experimentally relevant equilibrium.

This test introduces a number of complexities relative to the CBM18 case, including the edge bootstrap current necessary to drive peeling instabilities, as well as a diverted plasma geometry. This evaluates aspects of the PB3D code — such as the peeling response and updated boundary condition — that have not previously been studied.

This work is a direct collaboration with Toon Weyens, the original developer for PB3D, and builds directly on work done by Toon during his graduate and post-graduate studies[6–10].

6.2 Case Study CBM18

The first step following the vacuum update is to insure the updated code still performs well in the classic ballooning benchmark using the CBM18 equilibrium. This benchmark has been previously performed on a number of other codes, including ELITE[2, 11] and NIMROD[12], as well as PB3D without the vacuum boundary[8].

The CBM18 test equilibrium created by P. Snyder is designed specifically for studying the ballooning response in MHD codes, with the pressure drive being optimized for destabilizing ballooning modes as the dominant instability. Thanks to its simplicity and reliability, the CBM18 equilibrium has become the standard benchmarking case for the ballooning response of a range of MHD codes. The equilibrium consists of Shanfranov-shifted circular cross-section flux surfaces with a density gradient large enough to drive ballooning instabilities in the edge. CBM18 does not include any pedestal bootstrap current and is therefore peeling stable. This makes it an ideal equilibrium for studying the infinite-n ballooning limit for different numerical tools.

Figure 6.1 shows the pressure and safety factor profiles for the CBM18 equilibrium. With the pressure profile located far from the vacuum boundary ($\psi_{ped} \sim 0.6$ versus $\psi_{edge} = 1.0$), there should be minimal influence from vacuum boundary condition. Between the absence of

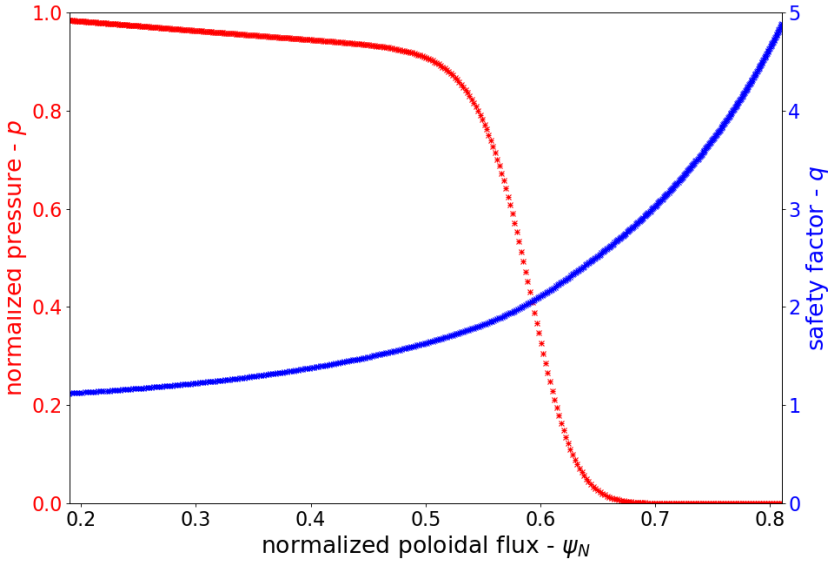

FIGURE 6.1: Equilibrium profiles for the CBM18 benchmarking equilibrium.

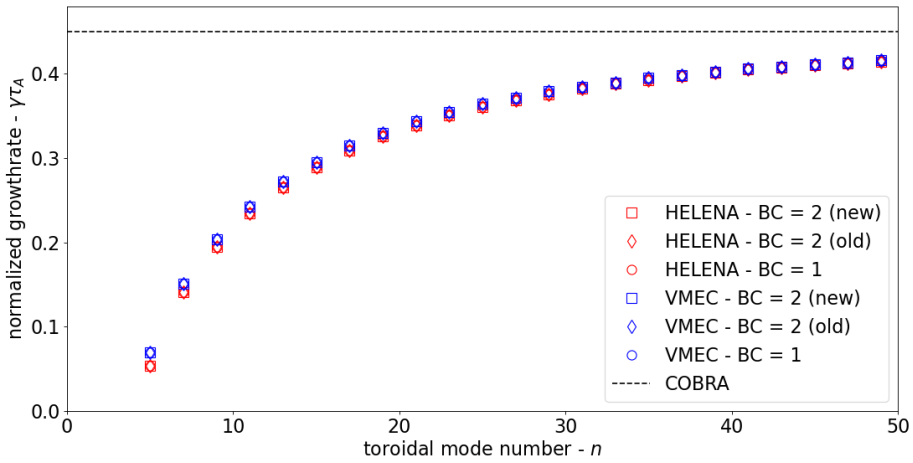

FIGURE 6.2: PB3D growthrates for the CBM18 benchmark using both VMEC and HELENA equilibria using both the original and updated versions of the PB3D vacuum boundary condition (BC = 2), as well as the fixed boundary condition (BC = 1).

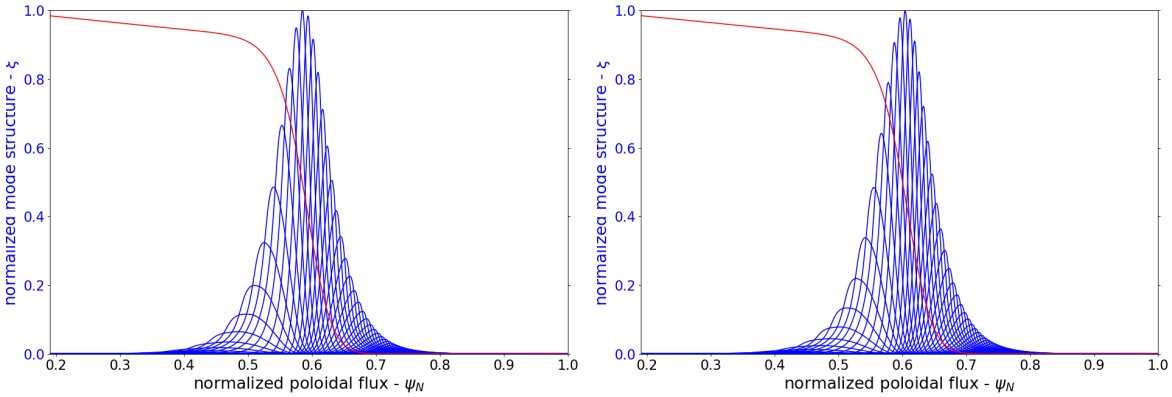

FIGURE 6.3: Modes X_m with $n = 15$ at low-field side midplane using the updated PB3D vacuum boundary condition for the (left) HELENA and (right) VMEC versions of the CBM18 equilibrium.

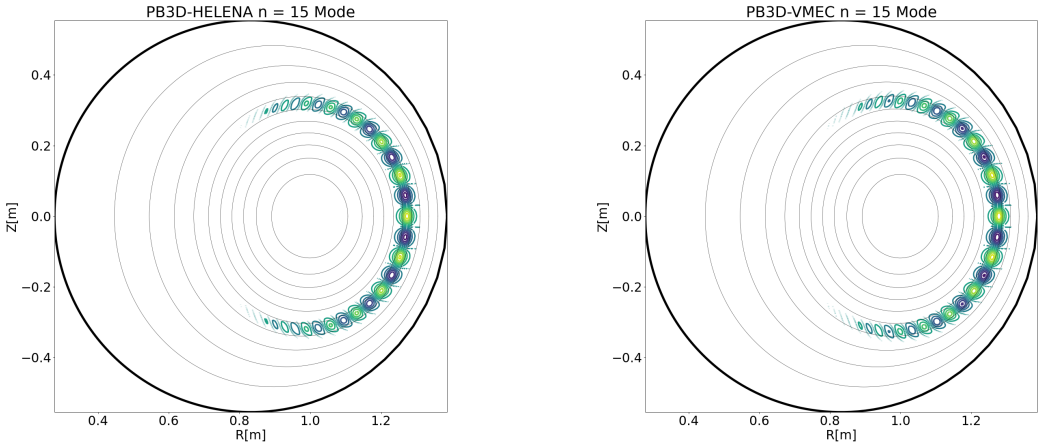

FIGURE 6.4: $n = 15$ mode structure cross section using the updated PB3D vacuum boundary condition for the (left) HELENA and (right) VMEC versions of the CBM18 equilibrium. Includes flux surfaces (gray) and last closed flux surface (black) for the equilibrium.

peeling drive and the pedestal location, both the original and updated versions of PB3D are expected to give basically the same result.

For this study, PB3D was used with 1000 radial grid points and 40 poloidal modes. The parallel integration grid consists of 50 grid points for the initial Richardson iteration with each of the 5 iterations doubling the number of points until convergence is achieved. These conditions were found sufficient for achieving well converged solutions for toroidal mode numbers 5-50. The results are compared to the infinite-n ballooning limit calculated using the COBRA code[13].

The results for the benchmark are given in figure 6.2. The study includes PB3D calculations using both a HELENA and VMEC versions of the CBM18 equilibrium, as well as three separate $\psi_n = 1$ boundary conditions. Boundary style 1 is for fixed boundary, in which it is assumed that $\xi(\psi_n = 1) \to 0$, which is often used in ballooning-only calculations. Boundary style 2 is for free boundary calculations using the peeling-ballooning vacuum boundary condition discussed in section 4.4, looking at both the case with the full vacuum perturbation (new) and without (old). Note that the old version still has the boundary contributions from the surface terms of the plasma potential.

It is found that PB3D gives near identical results for the CBM18 benchmark case, regardless of the boundary configuration. This results is expected, as the unstable region is located away from the plasma-vacuum interface, and the edge current is not sufficient to destabilize peeling instabilities. This is illustrated in figure 6.3, which shows the $n = 15$ mode structure at the LFS midplane. It is clearly seen that the mode structure peaks in the pedestal region, and has fully decayed away before the boundary effects becomes important.

There is good agreement between the PB3D calculations and those from previous CBM18 benchmarking exercises. Figure 6.2 shows the PB3D results asymptotically approaching the infinite-n growthrate calculated using the COBRA ballooning code[8, 13]. Additionally, the modes are seen to localize within the region of large pressure gradient (figure 6.3) in the bad curvature region (figure 6.4) as predicted by infinite-n ballooning theory[14]. These results

are in good agreement with the previous PB3D and MISHKA benchmark[8], as well as the ELITE calculations for CBM18[15].

It is worth noting that there is a small variation between the PB3D results using the HELENA equilibrium compared to VMEC, particularly at low toroidal mode number. This is likely the result of minor differences in the equilibria themselves (as they are calculated using different mechanisms), and not differences with PB3D itself. Specifically, the peak pressure gradient is marginally larger in the VMEC equilibrium, resulting in a slightly more unstable configuration. Regardless of these differences, the PB3D results share the same qualitative behavior with the mode structures (figure 6.4) being indistinguishable form one another.

6.3 Case Study A34424

In order to test a broader scope of PB3D functionality, it is necessary to consider equilibria with features more relevant to experimental systems. For this study, equilibria based on ASDEX Upgrade shot 34424 are considered. This discharge was a part of a campaign for studying the effects of 3D magnetic perturbations on ELM stability and localization[1], similar to the experiments discussed in chapter 5.

These discharges are recreations of the plasma configuration presented in [16, 17], which focused on the plasma response to 3D magnetic perturbations in MAST and ASDEX Upgrade. The toroidal magnetic field (B_T) is 1.8T, edge safety factor is $q_{95} \approx 3.9$, and the upper triangularity is relatively low ($\delta_u \approx 0.12$). For comparison, the experiments referenced in chapter 5[18] had $B_T \approx 2.55T$ and $q_{95} \approx 5.3$. The lower toroidal field in this experiment allows for a larger relative field strength of the externally rotating MP field. During the flattop in the plasma current and heating power, a rotation frequency of 3Hz was applied to the perturbation field.

Figures 6.5 and 6.6 presents a quick summary of the experimental results[1]. The ECE spectrogram (figure 6.5a) shows the same localized ballooning instabilities in the pedestal

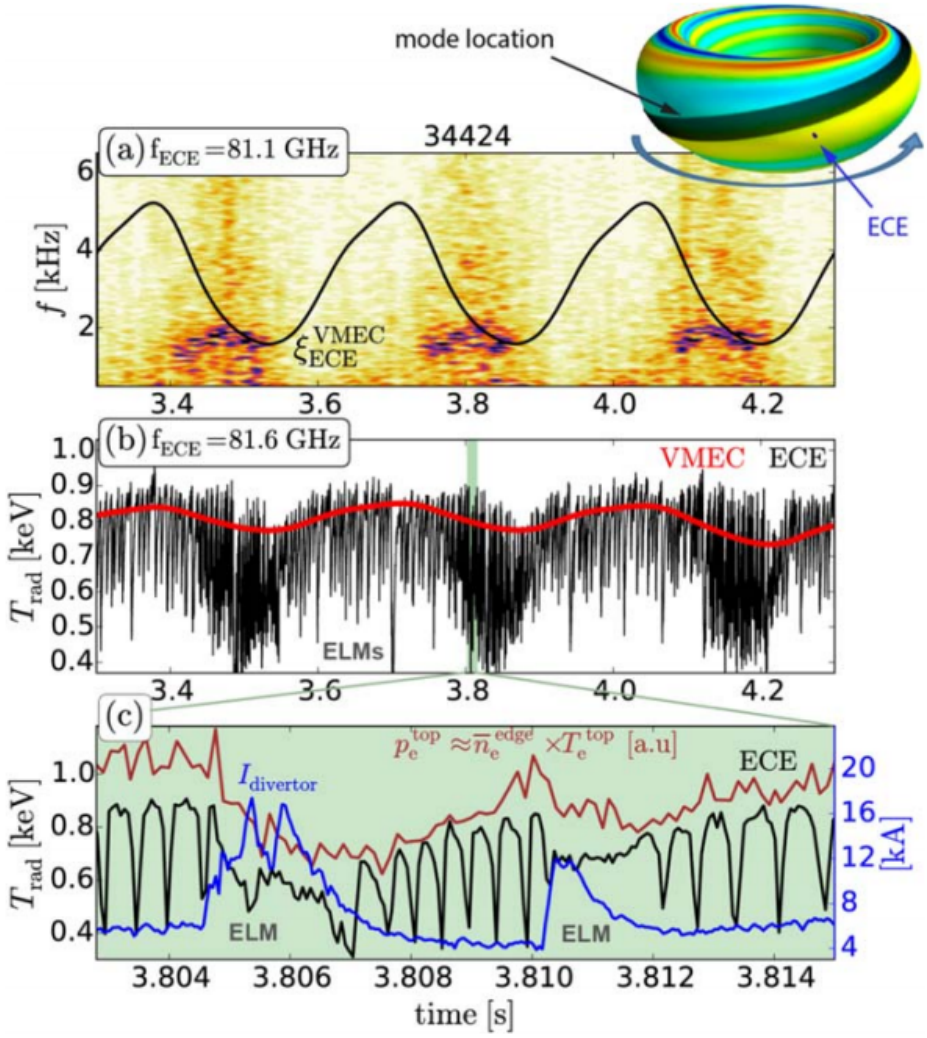

FIGURE 6.5: Inset at the top shows ECE measurements in the pedestal region during rigid rotation. (a) Spectrogram from ECE channel within the plasma boundary and corresponding ξ_r along the ECE LOS. (b) Synthetic T_e from VMEC (red) and T_{rad} from ECE (black). (c) Zoom of (b) showing ECE (black), divertor current to indicate ELM timing (blue) and approximation for the pedestal top pressure (brown). [1]

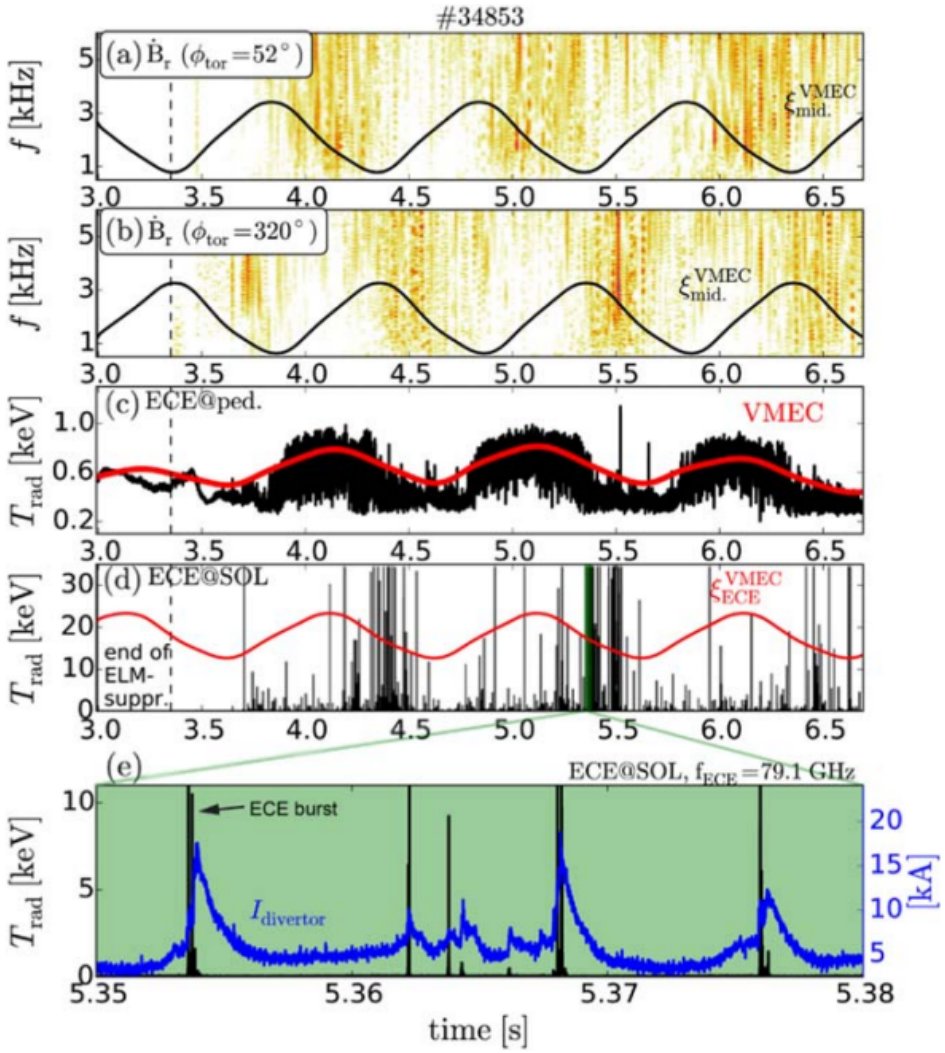

FIGURE 6.6: Measurements of a preferential position of ELM crashes in the 3D geometry. (a) Magnetic perturbations on $\dot{B}_r$ around LFS midplane and corresponding VMEC corrugation. (b) Same as (a) but on a toroidal position shifted by 90° and hence, the signatures from the ELM crashes (darken vertical stripes) are in anti-phase ($n = 2$) to (a). (c) Synthetic T_e from VMEC (red) and T_{rad} in the pedestal. (d) T_{rad} from the ECE diagnostic in the SOL measuring radiation from energetic electrons (up to 35 keV) seen as bursts in the ECE. (e) Zoom of (d) with divertor current to show that the ECE bursts are only at the onset of an ELM suggesting local energetic electrons. [1]

during rigid rotation as discussed previously. The ballooning modes occur during the density build-up phase preceding ELM crashes (figure 6.5 b and c) when the plasma displacement as the zero crossing (going from max to min).

In addition to the localized ballooning, these experiments investigated how the 3D perturbations influenced the ELM behavior, which can be summarized by figure 6.6. Panel (a) and (b) present magnetic probe measurements from the LFS midplane, taken from toroidal locations 90° apart. The dark vertical stripes are indicative of ELM crashes, which are in anti-phase due to the the rigidly rotating $n = 2$ MP field, show the ELM crashes localizing near $\xi_r \approx 0$. Additionally, the ECE channels probing the near-SOL (figure 6.6d) also show signatures of a local ELM crash. Interestingly, the observed bursts in the ECE occur during the initial phase of the ELM crash (figure 6.6e), and are strongest and the most frequent when the 'bad' zero crossing of ξ_r crosses the LOS of the ECE.

With these experiments showing a large amount of evidence of the 3D MPs resulting in localization of both ballooning instabilities and ELMs, they provide an ideal case study for testing PB3D and studying peeling-ballooning stability with 3D equilibria. The numerical tests performed here focus on the stability of 2D equilibria based on experimental reconstructions, with future work addressing the effects of the 3D perturbations.

6.3.1 A34424 Results with PB3D

For this study, three variations on the 34424 CLISTE reconstruction are used. Each case is then processed using the HELENA equilibrium code to create axisymmetric equilibria capable of being used by PB3D, MISHKA, and ELITE. The same basic plasma shaping and pressure profile were used in each case, with the main difference coming in the edge current and safety factor profiles. Figure 6.7 shows pressure, safety factor, and parallel current profiles in the pedestal region for the three cases. The notation $a_5 j_i$ refers to the amount of equilibrium pressure gradient (a) and current (j) relative to the initial reconstruction (e.g. $a_5 j_0$ has the least plasma current, while $a_5 j_4$ has the most). Increasing the bootstrap current has the added

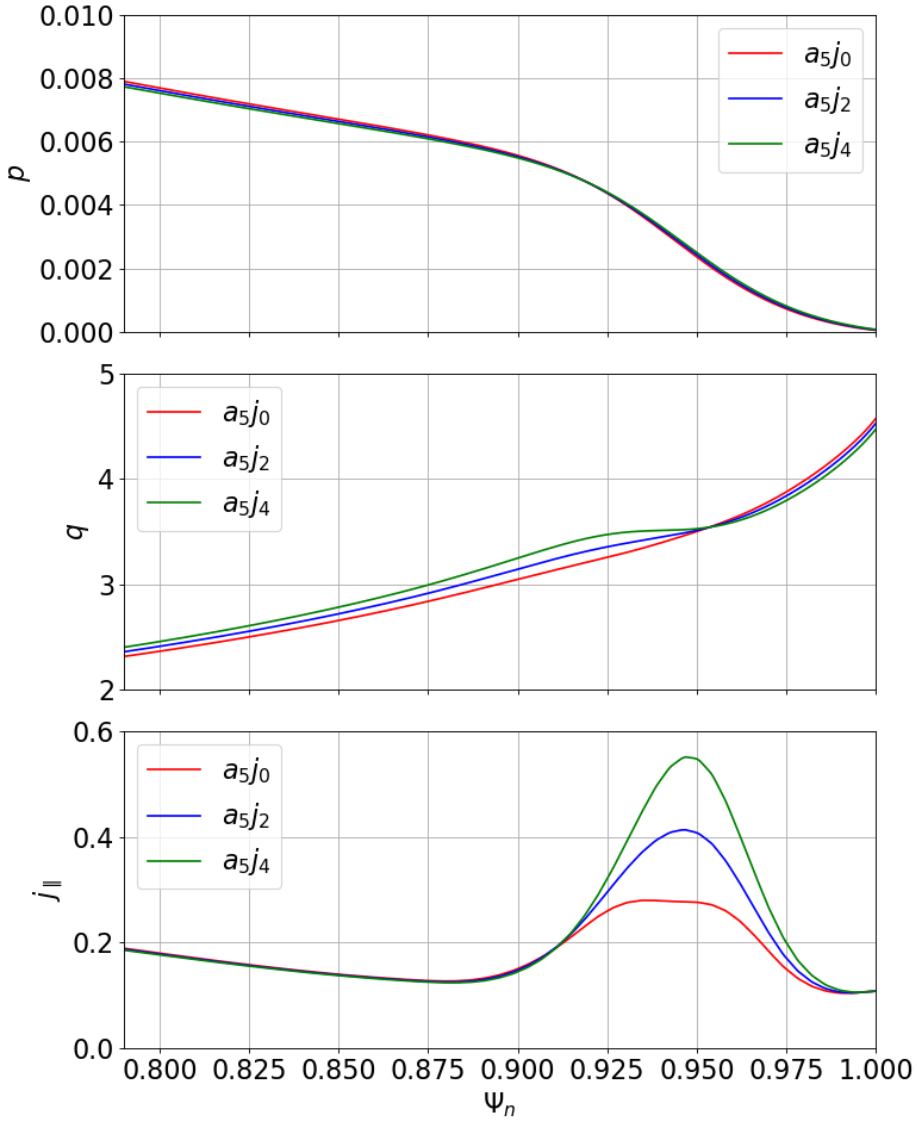

FIGURE 6.7: Equilibrium profiles for the three A34424 cases.

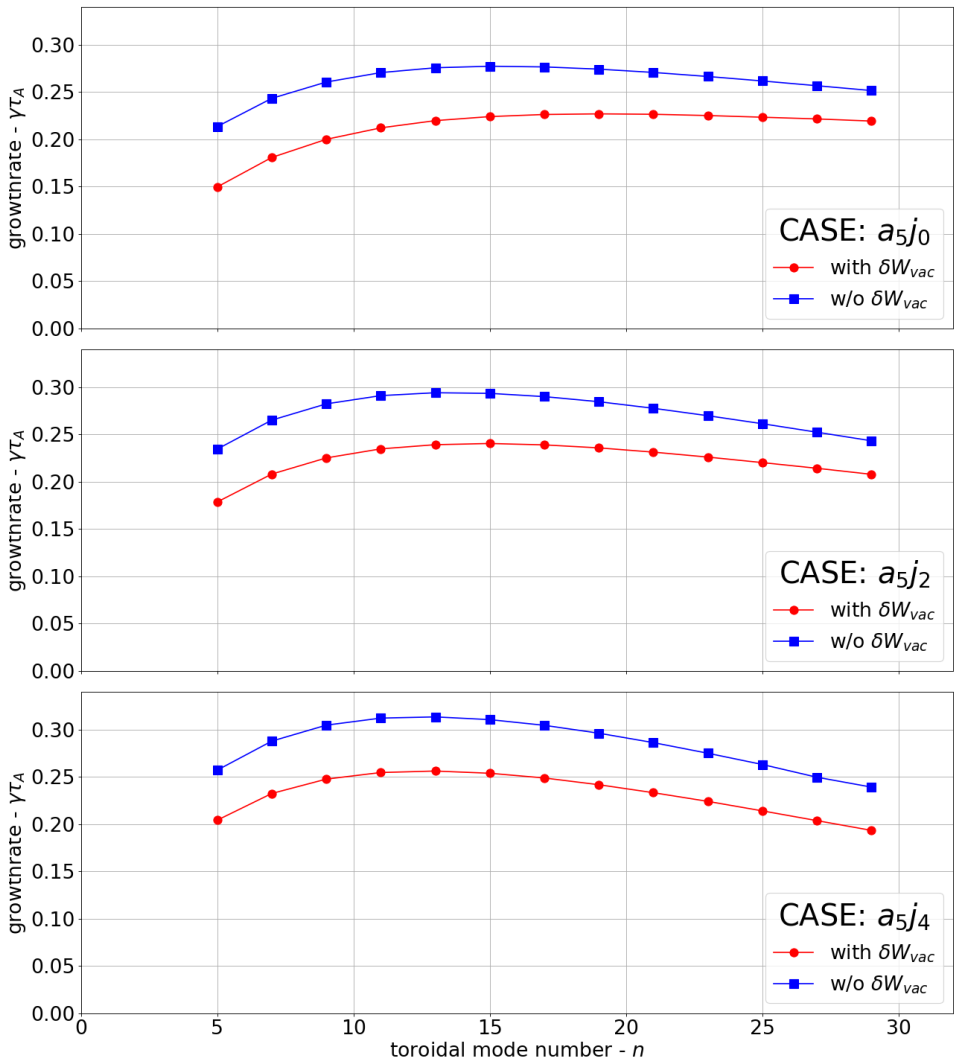

FIGURE 6.8: Growthrates for the three A34424 equilibria cases calculated using PB3D.

consequence of reducing the magnetic shear (q') in the pedestal, which can play a role in plasma stability.

Typical PB3D calculations utilized 2000 radial grid points and 50 poloidal modes. The parallel integration grid consists of 70 grid points for the initial Richardson iteration with each of the 5 iterations doubling the number of points until convergence is achieved. These conditions were found sufficient for achieving well converged solutions for toroidal mode numbers 5-30. It is worth noting that PB3D is limited to studying instabilities with toroidal mode number $n \geq 5$.

Results for the three equilibria with PB3D are shown in figure 6.8. For all three cases, PB3D predicts unstable peeling-ballooning modes with peak mode numbers $n = 12 - 18$ with no marginal stability point observed for $n = 5 - 30$. The absence of a low-n marginal stability point is concerning, and may indicate an error in the PB3D calculations. This is investigated further in the next section.

Comparisons between the three equilibria show the effects of the peeling instability becoming more prominent with increased bootstrap current, as expected. Case $a_5 j_0$ is the most ballooning-like, with the smallest low-n growthrates, the peak growthrate occurring at the the highest mode number ($n = 18$), and the high-n modes remaining relatively constant. As the current drive increases in cases $a_5 j_2$ and $a_5 j_4$, the peeling instability becomes more prominent, increasing the low-n growthrates and shifting the peak growthrate to lower toroidal mode numbers. Additionally, the increased edge current reduces the magnetic shear in the pedestal (as seen in figure 6.7, which has a stabilizing effect on the high-n ballooning modes[19],

The effects of the adding the perturbed vacuum response into the boundary condition can also be seen in figures 6.8 and 6.9. Contributions from the vacuum are expected to be universally stabilizing[20], which is exactly the result seen here. For all three equilibria cases, there is around $15 - 20\%$ reduction in the growthrates when the vacuum response is included. This can be seen more clearly in figure 6.9, which shows the mode structure for the $a_5 j_2$ equilibrium with and without the vacuum contribution. It is seen that the vacuum response reduces

the mode amplitude near the plasma-vacuum boundary, resulting in a smaller growthrate. It is also worth noting that the effects of the vacuum response are radially localized near the boundary, with the mode structure being unaffected for $\psi_N \lesssim 0.98$.

6.3.2 Benchmark with MISHKA and ELITE

In order to better assess the validity of the PB3D calculations, stability calculations for the A34424 equilibria were performed using the MISHKA[21] and ELITE[2] for comparison. For the purposes of this benchmark, the HELENA versions of the equilibria were used, as all three codes can work from the same HELENA input (as opposed to only PB3D being able to use VMEC). Figure 6.11 shows the calculated growthrates for ELITE, MISHKA, and PB3D (with the complete perturbed vacuum boundary condition) for each of the A34424 cases. It is seen that the MISHKA and ELITE results agree well with one another, while PB3D significantly overestimates the growthrates of the instability. The source of this inconsistency is not yet known, but these benchmark results can be used to help identify potential causes.

As PB3D behaved well in the CBM18 — which does not have bootstrap current in the pedestal — it can be reasoned that the current response term may be at fault. This is further emphasised by the difference between each of the three cases: as the bootstrap current is increased, the relative error between PB3D and the other codes also increases. Properly identifying and correcting the exact source of this error is essential before future studies with PB3D are performed.

However, there are still promising elements of the PB3D results compared to ELITE and MISHKA. PB3D does capture some of the qualitative behavior seen in the results from the other codes. MISHKA and ELITE have the low-n marginal stability point and the most unstable mode shifts to smaller toroidal mode numbers with increased current. While PB3D does not capture the marginal stability points, the general behavior of decreased low-n stability is observed. Similarly, all three codes show high-n stabilization with decreased magnetic shear associated with the increase in bootstrap current.

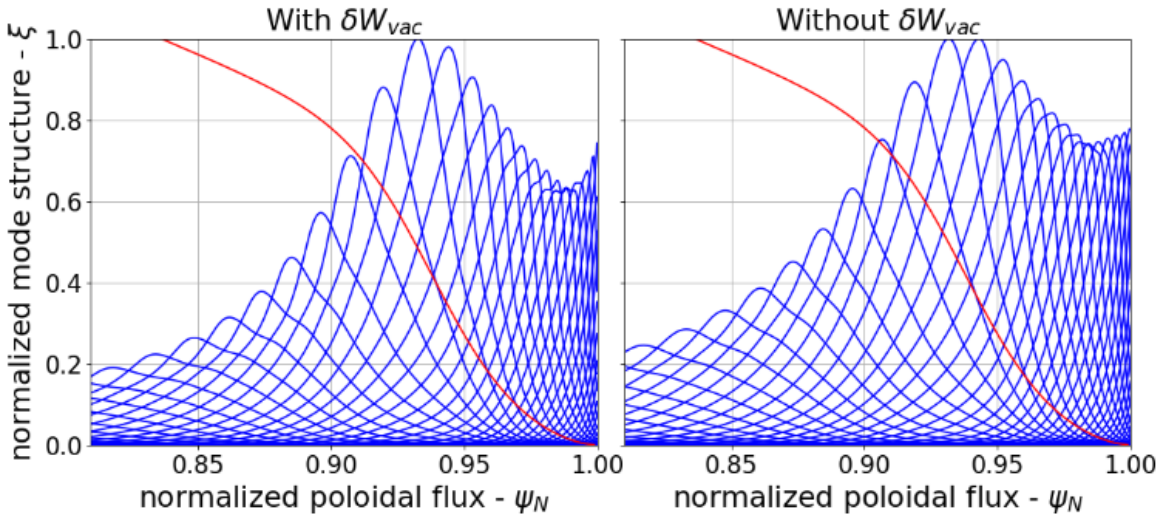

FIGURE 6.9: Mode structure for the $n = 10$ mode for case $a_5 j_0$ using the updated vacuum boundary condition (left) compared to the original boundary condition (right).

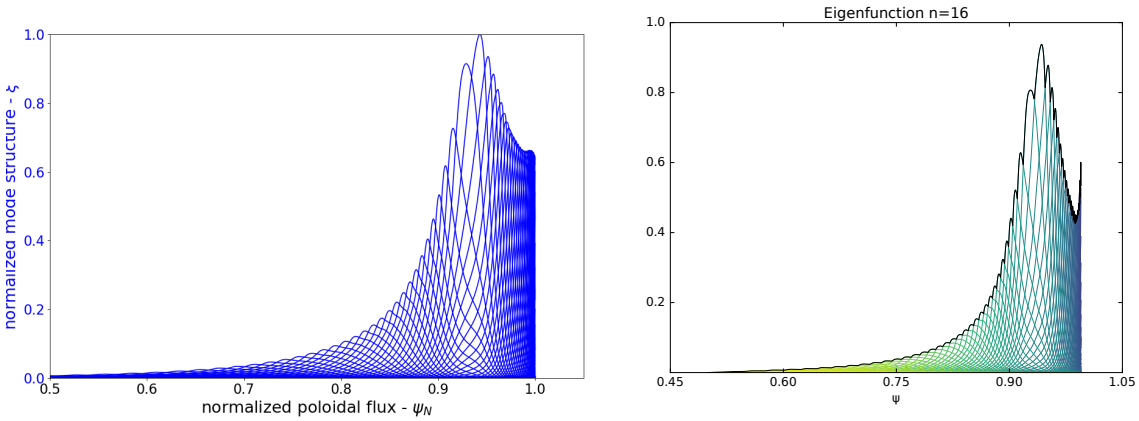

FIGURE 6.10: Mode structure of the $n = 16$ for the $a_5 j_4$ equilibrium using PB3D (left) and ELITE (right).

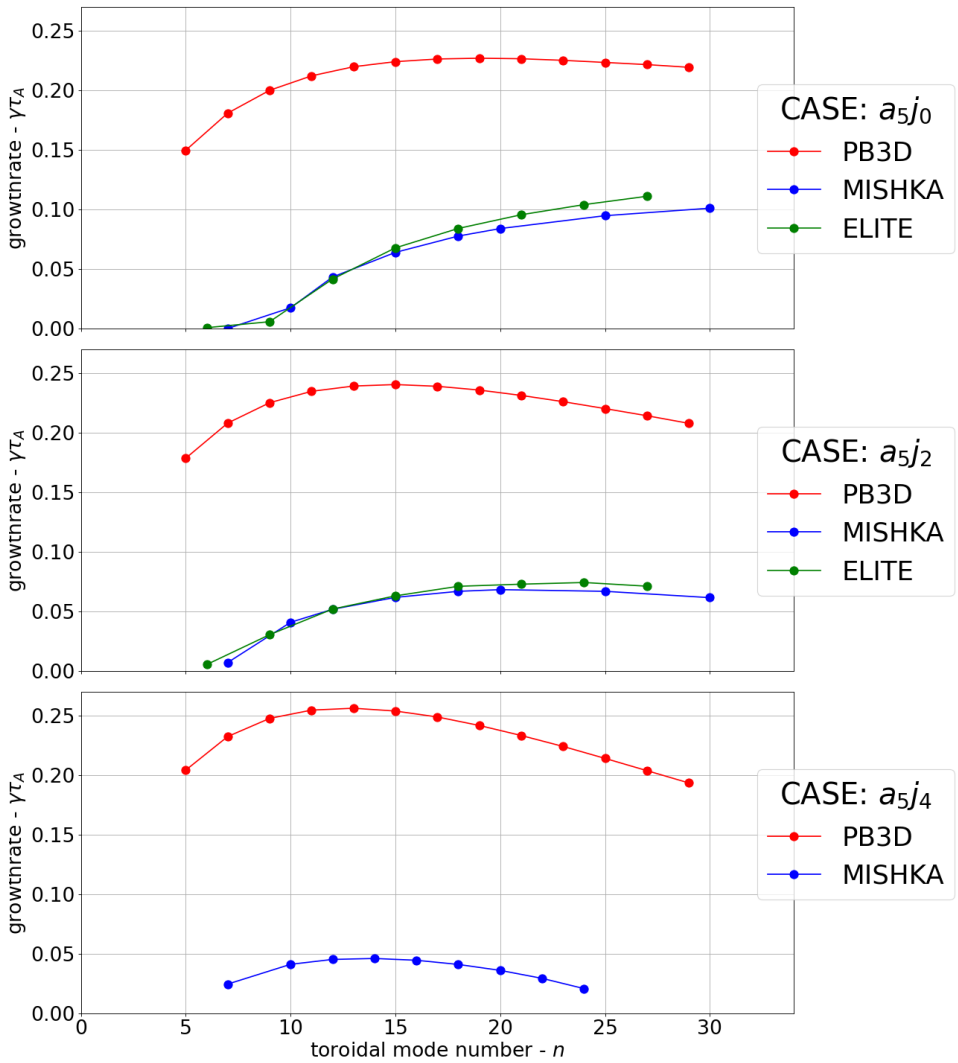

FIGURE 6.11: Benchmark results for PB3D, MISHKA, and ELITE for the three 34424 equilibria cases.

The mode structures for PB3D are similar to those of ELITE, as seen in figure 6.10, with the same general envelope structure. However, looking at the mode structure for the $n = 16$ with the $a_5 j_4$ equilibrium (which has the largest current drive), it is clearly seen that the peeling response in PB3D is significantly larger than that of ELITE. While both codes give the mode amplitude at the edge ($\psi_n = 1$) to be roughly the same, the amplitude for PB3D for $0.98 \lesssim \psi_n \lesssim 1$ greatly exceeds that of ELITE in the same region. This behavior implies that the current drive contribution in PB3D is larger than it should be, giving further insight into possible errors within the code.

6.3.3 HELENA vs VMEC

Up to this point, we have only considered the 2D HELENA equilibria to maintain consistency between PB3D, MISHKA, and ELITE. However, as one of the key features of PB3D is the ability to run using 2D and 3D VMEC equilibria, it is worth comparing how PB3D processes equivalent VMEC and HELENA equilibria. For the sake of comparison, the three A34424 cases were recreated using fixed-boundary VMEC in 2D.

Figure 6.12 shows the growthrates calculated using PB3D for each of the three cases using both HELENA and VMEC as inputs. Similar to the HELENA results, PB3D-VMEC significantly over-predicts the magnitude of the growthrate in comparison to other codes, while maintaining some of the most basic features of the solution. However, there is still a fairly large difference between the VMEC and HELENA results.

To better investigate this, figures 6.13 and 6.14 compare the mode structure for the $n = 10$ mode of $a_5 j_2$ for the two equilibrium sources. As before, the PB3D-HELENA mode structures have the more standard peeling-ballooning mode behavior, but this does not hold for PB3D-VMEC. Figure 6.14 shows a poloidal cross section of the global mode structure for both cases. While the large scale structure of the mode is similar between the two cases, it is seen that the VMEC solution has small scale numerical oscillations near the boundary. This is seen

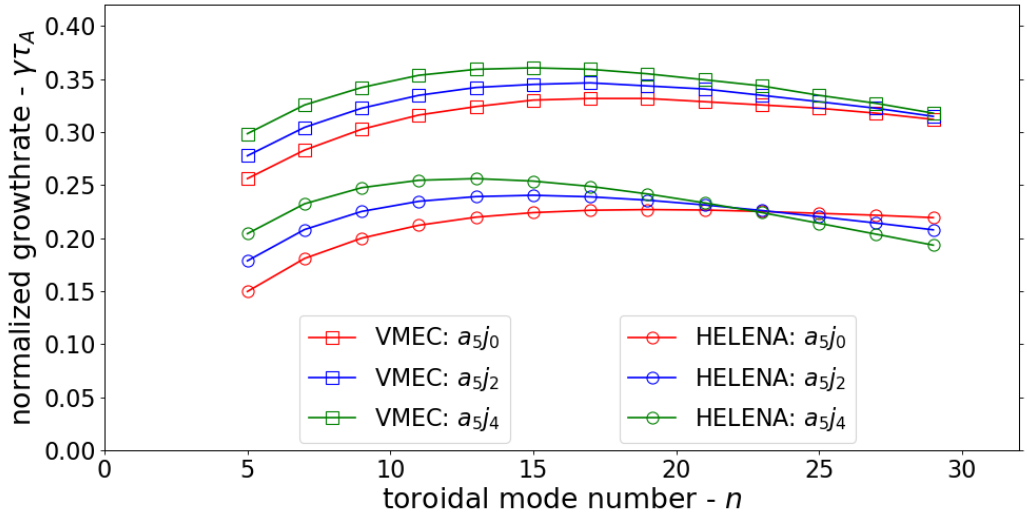

FIGURE 6.12: PB3D growthrates for the three A34424 cases using both VMEC and HELENA equilibria.

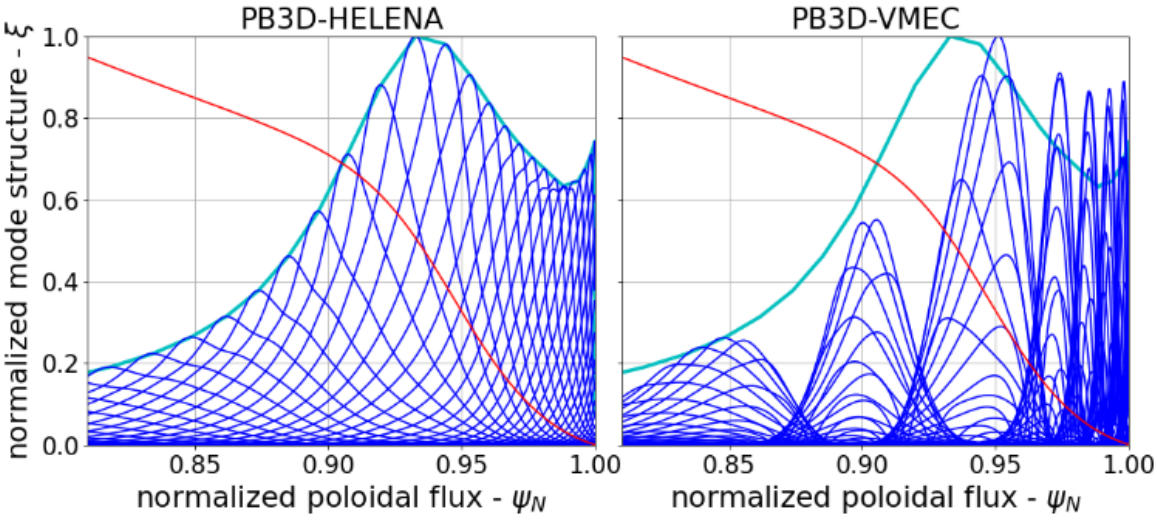

FIGURE 6.13: PB3D $n = 10$ mode structure at LFS midplane for (left) HELENA and (right) VMEC equilibrium 34424-a5j2. The cyan line shows the mode envelope for the HELENA results.

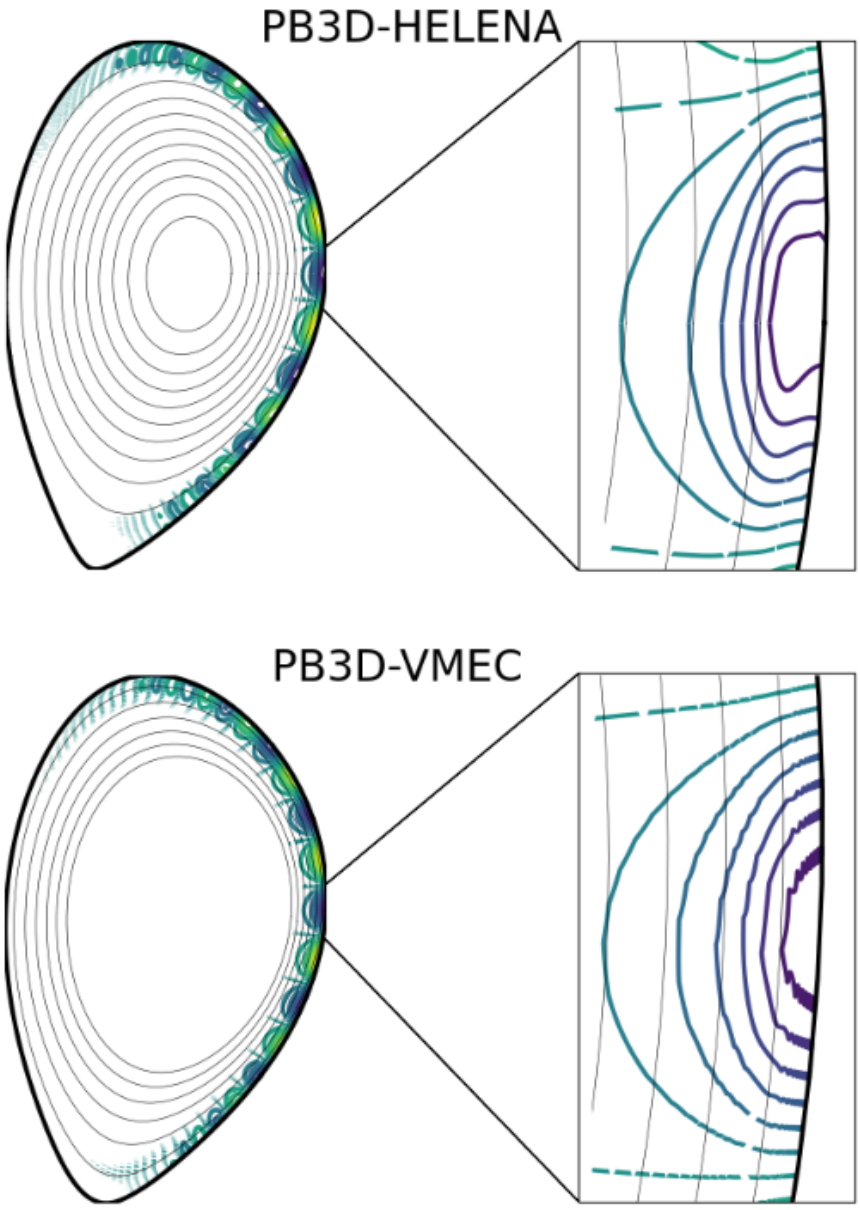

FIGURE 6.14: Poloidal cross section of the $n = 10$ mode for (top) HELENA and (bottom) VMEC $a_5 j_2$ equilibrium. Both cases include a cutout of the mode structure at the LFS Midplane.

more clearing in figure 6.13, which shows the mode structure in the pedestal region at the LFS midplane.

This work has helped to identify a number of possible causes for the "bad" PB3D solutions when using VMEC equilibrium. One possible issue is that the VMEC for ASDEX Upgrade experiments are calculated using a left-handed coordinate system, while PB3D is formulated using a right-handed system. For comparison, the CBM18 VMEC equilibrium uses right-handed definitions, which may be why no error is seen there. Investigation into this has found errors in the code that only occur with the left-handed ASDEX equilibria, which are actively being address. That said, it is not clear if this is the cause of this observed behavior, and more testing will be required once these bugs are addressed.

Another potential source of error is discrepancies between the equilibrium themselves. Similar to the CBM18 case, there are subtle differences in between the VMEC and HELENA versions of these ASDEX equilibria. While the pressure and q profiles are almost identical, it is worth noting that the parallel current calculated by VMEC does vary a reasonable amount from the HELENA results. Since PB3D may be over-predicting the effects of the bootstrap current (as discussed in the previous section), it is possible that these small discrepancies could results in a significant change in growthrate.

6.4 Summary

New numerical tools are currently being developed in order to properly study the effects of 3D magnetic perturbations on MHD stability. Among these tools is the new 3D peeling-ballooning code, PB3D[8], which uses high-n 3D edge peeling-ballooning theory to study fully 3D plasma equilibria. While early results for PB3D are promising[7], the code is still actively being developed and requires a significant amount of testing, especially with the completion of the vacuum boundary condition.

Starting with the ballooning benchmark CBM18, PB3D successfully reproduces the expected results compared to other codes like COBRA and ELITE. PB3D was achieved the same results regardless of the boundary condition used, showing that the update to the vacuum boundary did not negatively impact the elements of the code that had been previously working. Additionally, there was little difference between the VMEC and HELENA equilibria cases, with any inconsistencies being attributed to the equilibria themselves opposed to PB3D's calculations.

While the CBM18 results were generally positive, this does not hold for more complicated systems like the A34424 equilibria. It is seen that adding complexity to the source equilibrium leads to PB3D results that are not consistent with other codes. While the updates to the vacuum boundary condition did improve the results, the difference between other codes is still substantial, hinting to larger unresolved issues in the code. These results, though discouraging, are not entirely unexpected, as this is the first major test of the PB3D code with more complex equilibria. It is important that these results are used to help identify potential issues with the code and provide guidance for code development. Two major differences between the A34424 cases and the CBM18 case is the addition of realistic plasma shaping and edge bootstrap current, both of which introduce new complexities and potential sources of error, and should be investigated more closely.

References

[1]M Willensdorfer et al., "Dynamics of ideal modes and subsequent ELM crashes in 3d tokamak geometry from external magnetic perturbations", Plasma Physics and Controlled Fusion **61**, 014019 (2018).

[2]H. R. Wilson, P. B. Snyder, G. T. A. Huysmans, and R. L. Miller, "Numerical studies of edge localized instabilities in tokamaks", Physics of Plasmas **9**, 1277–1286 (2002).

[3]M. Anastopoulos-Tzanis, B. Dudson, C. Ham, C. Hegna, P. Snyder, and H. Wilson, "Non-axisymmetric equilibrium and stability using the ELITE stability code", Nuclear Fusion **59**, 126028 (2019).

[4]C. Schwab, "Ideal magnetohydrodynamics: global mode analysis of three-dimensional plasma configurations", Physics of Fluids B: Plasma Physics **5**, 3195–3206 (1993).

[5]PPPL, *M3d-c1* ((accessed October 2020)).

[6]T. Weyens, R. Sánchez, G. Huijsmans, A. Loarte, and L. García, "PB3D: A new code for edge 3-D ideal linear peeling-ballooning stability", J. Comput. Phys. **330**, 997–1009 (2017).

[7]T. Weyens, "3d ideal linear peeling ballooning theory in magnetic fusion devices", PhD thesis (2016).

[8]T. Weyens, R. Sánchez, L. García, A. Loarte, and G. Huijsmans, "Three-dimensional linear peeling-ballooning theory in magnetic fusion devices", Phys. Plasmas **21**, 10.1063/1.4871859 (2014).

[9]T. Weyens, J. M. Reynolds-Barredo, and A. Loarte, "Computationally advantageous expressions for 3-D MHD stability", Comput. Phys. Commun. **242**, 60–71 (2019).

[10]T. Weyens, "Expressions for perturbed vacuum potential energy for 3D linear MHD stability", Phys. Plasmas **26**, 10.1063/1.5086538 (2019).

[11]P. B. Snyder et al., "Edge localized modes and the pedestal: A model based on coupled peeling-ballooning modes", Phys. Plasmas **9**, 2037–2043 (2002).

[12]B. J. Burke, S. E. Kruger, C. C. Hegna, P. Zhu, P. B. Snyder, C. R. Sovinec, and E. C. Howell, "Edge localized linear ideal magnetohydrodynamic instability studies in an extended-magnetohydrodynamic code", Physics of Plasmas **17**, 032103 (2010).

[13]R. Sanchez, S. Hirshman, J. Whitson, and A. Ware, "Cobra: an optimized code for fast analysis of ideal ballooning stability of three-dimensional magnetic equilibria", Journal of Computational Physics **161**, 576–588 (2000).

[14]J. W. Connor, R. J. Hastie, and J. B. Taylor, "High Mode Number Stability of an Axisymmetric Toroidal Plasma.", Proc R Soc London Ser A **365**, 1–17 (1979).

[15]N. M. Ferraro, S. C. Jardin, and P. B. Snyder, "Ideal and resistive edge stability calculations with m3d-c1", Physics of Plasmas **17**, 102508 (2010).

[16]A. Kirk et al., "Effect of resonant magnetic perturbations on low collisionality discharges in MAST and a comparison with ASDEX Upgrade", Nucl. Fusion **55**, 043011 (2015).

[17]W Suttrop et al., "Experimental studies of high-confinement mode plasma response to non-axisymmetric magnetic perturbations in ASDEX upgrade", Plasma Physics and Controlled Fusion **59**, 014049 (2016).

[18]M. Willensdorfer et al., "Three dimensional boundary displacement due to stable ideal kink modes excited by external n = 2 magnetic perturbations", Nucl. Fusion **57**, 10.1088/1741-4326/aa7f4c (2017).

[19]D. Lortz, "The general "peeling" instability", Nuclear Fusion **15**, 49–54 (1975).

[20]G. T. A. Huysmans, "External kink (peeling) modes in x-point geometry", Plasma Physics and Controlled Fusion **47**, 2107–2121 (2005).

[21]A. Mikhailovskii, G. Huysmans, W. Kerner, and S. Sharapov, "Optimization of computational mhd normal-mode analysis for tokamaks", Plasma Physics Reports **23**, 844–857 (1999).

Chapter 7

Discussion and Future Work

7.1 Discussion of Results

Toroidal localization of MHD instabilities has been observed in ASDEX-Upgrade experiments [1]. Application of infinite-n ballooning theory to 3D VMEC equilibria based on these experiments has predicted the existence and basic behavior of these ballooning instabilities. Experimentally, the instability localized to field lines where the edge plasma displacement is zero, but only when the pedestal is moving inward towards the plasma core (when rotating the MPs in the positive toroidal direction). The second zero in the displacement (when the pedestal is moving outward with the same MP rotation) is observably stable, despite the same pressure gradient being present in both cases. This results is substantiated by ideal MHD analysis, which is found sufficient for studying the basic behavior of the localized instability.

A key feature to the 3D ballooning instability is its dependence on the strength of the applied magnetic perturbations for both the experimental and numerical observations. Most notable is the requirement of a minimum amount of 3D displacement to observe the localized instability. This behavior is seen in other aspects of these low collisionality 3D perturbation experiments, namely the ELM mitigation [2, 3]. These phenomena tend to scale linearly with the magnetic perturbation strength after the initial onset occurs [2]. It has been seen that ELM-mitigation is at its peak for $\Delta\varphi_{UL} \approx -90^\circ$ [4], as is the ballooning growth rate. These

correlations raise new questions on the relationship, if any, between the localization of the ballooning instabilities and the ELM mitigation observed in these experiments.

Focusing on the ballooning instability, we use a δW-like approach to gain insight into the mechanism of the instability. It was seen that the localization of the instability is the results of the line-bending energy decreasing until it is no longer sufficiently balancing the pressure-curvature drive when the 3D magnetic perturbation is increased. This can be used to explain the threshold behavior mentioned above. Until a sufficient amount of 3D displacement is present, the stabilizing term remains large enough to balance the drive. Beyond this point, the difference between the drive and stabilizing terms grows linearly with the magnitude of the 3D displacement, leading to the linear growth of the localized instability.

Analysis of the local magnetic geometry provides further insight into the underlying physical mechanism behind the localization of the ballooning instability. It is observed that the curvature terms have negligible 3D variation, while the integrated magnetic shear, governed by the local magnetic shear, has strong variation with changing field lines, namely the effect of the shear is significantly reduced on field lines that are ballooning unstable. This results is expected, as it has previously been shown that 3D magnetic perturbations can significantly impact local geometry [5], which can subsequently impact edge stability and transport [6]. However, our result deviates from the above in that we consider non-resonant magnetic perturbations in which the stable kink response is optimized, allowing for different components of the local geometry to govern edge stability. Specifically, previous results focused on changes in the local magnetic shear driven by Pfirsch-Schlüter currents at dominant rational surfaces [6]. The increased kink response studied here leads to the normal torsion dominating the local 3D variation of the magnetic shear throughout the pedestal region, even in the absences of dominate rational surfaces. It is worth noting that VMEC equilibria do not properly handle localized sheet currents at rational surfaces, however, sufficient radial resolution has been shown to lead to well converged values for key local geometry terms [7, 8], which was accounted for in this work.

Three-dimensional equilibria modifying the ballooning stability along field lines is not unique to magnetically perturbed tokamak equilibria. In stellarator equilibria, incommensurate helicities present in key geometric quantities break the symmetry of the local magnetic geometry and produce localized ballooning instabilities that can significantly alter the ballooning stability boundaries [9, 10], as well as impact the underlying turbulence and microstability [11]. The axisymmetric equilibria studied here are stable to ballooning modes due to the weak shear in the pedestal providing access to the secondary stability region [12]. However, the 3D magnetic perturbations lead to the large kink response at the top of the pedestal, which in turn causes symmetry breaking changes to the local magnetic geometry, locally modifying the stability boundary along the lines of Ref. [10].

There are still a number of open questions with regards to the toroidal localization of ballooning modes in the tokamak pedestal region. This localized ballooning behavior has been observed in a number of shots on ASDEX Upgrade [13]. However, it has been noticeably absent from DIII-D discharges with similar parameters [8]. Key differences between these cases are the amplitude of the kink response (3 mm on DIII-D versus 12 mm on AUG, despite similar size and MP) and the upper triangularity of the discharge, both of which could effect the 3D local geometry. Additionally, the DIII-D cases were operating in an ELM-suppressed regime, while the others were in mitigated regimes. More recent AUG ELM-suppressed discharges did not see the localized ballooning [13, 14]. This further motivates the need for investigating the effects of 3D shaping on local edge stability.

Another open question is the relationship between the observed localization of mitigated ELMs and the 3D destabilization of ballooning modes[15]. As ELMs are thought to be coupled peeling-ballooning instabilities, it is possible that the underlying mechanism changing the ballooning stability also plays a role in the ELM stability. This could give valuable insight into the physical mechanism behind ELM mitigation. In order to properly investigate this, we can make use of a full 3D peeling-ballooning physics model, along with a similar procedure as used in the ballooning study above, to systematically study the effects of 3D geometry on

ELM stability.

To better address the questions posed above, new numerical tools are required for studying peeling-ballooning stability with non-axisymmetric equilibria. To this end, the PB3D code[16] currently being developed has been specifically designed to address the issue of peeling-ballooning stability of 3D equilibria. With the recent addition of the vacuum perturbation for free-boundary calculations, PB3D should contain all the necessary physics for these studies, though testing shows significant work is still required before peeling-ballooning studies can be performed.

First steps in benchmarking PB3D involve comparing the results to the MHD tools like ELITE[17] and MISHKA[18], which are restricted to studying axisymmetric equilibria. Using 2D HELENA[18] equilibria, PB3D does well in benchmarks focusing on stability of pressure-curvature driven ballooning modes in simple geometries. However, the addition of edge current and realistic tokamak shaping to the equilibria results in a large divergence of the PB3D results from the other codes, implying that there are errors in the implementation of the peeling drive. Identification and correction of these errors, followed by repeated 2D benchmarking, are essential before additional PB3D studies are performed. Regardless of these issues, PB3D remains a leading candidate for future peeling-ballooning studies with 3D equilibria, and further development and testing of the code should be pursued.

7.2 Future Work

There are a number of avenues for work extending on the results of this thesis. As previously discussed, there are a number of open questions with regards to the effects of 3D magnetic perturbations and geometry on the stability of the pedestal. Up to this point, the localized ballooning instabilities have been studied primarily on the ASDEX Upgrade device[13, 15]. Other experiments, including MAST[19] and JET[20], have studied the effects of the magnetic perturbations on ballooning stability with similar results, but did not include formal analysis

of the 3D magnetic geometry in relation to the stability observations. Conversely, analysis experiments on DIII-D found no evidence of the localized ballooning instabilities[8], though the amplitude of the perturbations were much smaller and the ELMs were actively suppressed.

Based on this, a comprehensive study more directly comparing the results of various experimental devices should be considered. This would consist of comparing experimental discharges from various machines where operational parameters (perturbation amplitude, plasma shape, collisionality, etc.) and measurement techniques (such as the perturbation rotation) should be as constant as possible. This can be challenging, as machine size, magnetic coil configuration, and diagnostic availability vary between system. To assist in these experiments, numerical studies using the analysis discussed in this thesis can be applied to predict operating conditions for each device favorable to localized ballooning instabilities.

Another open question is the role of the 3D magnetic geometry in peeling-ballooning stability in relation to ELM mitigation and suppression. As discussed, there is experimental evidence that the 3D destabilization of ballooning modes correlates with mitigated ELM amplitude and frequency, and that the ELM filaments show similar localization behavior to the ballooning instabilities[15]. Based on this, it is possible that the underlying mechanism changing the ballooning stability also plays a role in the ELM stability. In order to properly investigate this, a peeling-ballooning code capable of studying 3D equilibria is needed. Using this tool, along with a similar procedure as used in the ballooning study discussed here, the effects of 3D geometry on peeling-ballooning stability can be systematically studied.

However, before these studies can be performed, development of new peeling-ballooning stability tools, such as PB3D, is required. There is currently ongoing work to expand ELITE to allow 3D equilibria to be studied[21], which provides one option for future work. In addition to this, development of the PB3D code should be continued, so that multiple tools are available and proper validation of the 3D studies can be performed.

Based on these results presented in chapter 6, future studies with PB3D should focus on determining the effects of the edge current and plasma shaping on the calculated stability,

helping to identify any code errors associated with them. Using the CBM18 equilibrium as a starting point, new equilibrium can be developed gradually introducing bootstrap current, plasma shaping, edge boundary effects, etc. independent of one another to better targets sources of error in the PB3D code. These types of studies have been performed previously with other codes including ELITE[21], M3D-C1[22], and BOUT++[23], which can be used for benchmarking of these future results.

Once the issues with PB3D have been resolved, there is still a large amount of testing that should been done to test the accuracy and robustness of PB3D. This is particularly important for studying 3D VMEC equilibria, as this aspect of the code remains largely untested. Future benchmarking efforts with other MHD codes capable of studying 3D equilibria, such as CAS-3D[24] and the recently updated ELITE[21], are necessary before physics studies can be performed using PB3D. While there is still a significant amount of work required before PB3D is ready for extensive use in physics studies, it does show promise to fill a much needed gap in the currently available numerical MHD tools.

Finally, non-axisymmetric boundary deformations are important to understand as changes in 3D geometry can play a key role in micro-instabilities and subsequent edge turbulent transport [6]. The same 3D geometric quantities discussed in this work enter into descriptions of micro-instabilities as described by gyrokinetic tools[25, 26]. A possible avenue for future work would be to systematically investigate the impact of 3D equilibrium changes on micro-instabilities and the resulting turbulent transport, which has been observed to increase during ELM suppression[27].

References

[1]M. Willensdorfer et al., "Plasma response measurements of external magnetic perturbations using electron cyclotron emission and comparisons to 3D ideal MHD equilibrium", Plasma Phys. Control. Fusion **58**, 10.1088/0741-3335/58/11/114004 (2016).

[2]A. Kirk et al., "Understanding edge-localized mode mitigation by resonant magnetic perturbations on MAST", Nucl. Fusion **53**, 10.1088/0029-5515/53/4/043007 (2013).

[3]A. Kirk et al., "Effect of resonant magnetic perturbations on low collisionality discharges in MAST and a comparison with ASDEX Upgrade", Nucl. Fusion **55**, 043011 (2015).

[4]M. Willensdorfer et al., "Three dimensional boundary displacement due to stable ideal kink modes excited by external n = 2 magnetic perturbations", Nucl. Fusion **57**, 10.1088/1741-4326/aa7f4c (2017).

[5]T. M. Bird and C. C. Hegna, "Controlling tokamak geometry with three-dimensional magnetic perturbations", Phys. Plasmas **21**, 10.1063/1.4898064 (2014).

[6]T. M. Bird and C. C. Hegna, "A model for microinstability destabilization and enhanced transport in the presence of shielded 3D magnetic perturbations", Nucl. Fusion **53**, 10.1088/0029-5515/53/1/013004 (2013).

[7]S. A. Lazerson, "Three-dimensional equilibrium reconstruction on the DIII-D device", Nucl. Fusion **55**, 10.1088/0029-5515/55/2/023009 (2015).

[8]R. S. Wilcox, A. Wingen, M. R. Cianciosa, N. M. Ferraro, S. P. Hirshman, C. Paz-Soldan, S. K. Seal, M. W. Shafer, and E. A. Unterberg, "Modeling of 3D magnetic equilibrium effects

on edge turbulence stability during RMP ELM suppression in tokamaks", Nucl. Fusion **57**, 10.1088/1741-4326/aa7bad (2017).

[9]P. Cuthbert and R. L. Dewar, "Anderson-localized ballooning modes in general toroidal plasmas", Phys. Plasmas **7**, 2302–2305 (2000).

[10]S. R. Hudson and C. C. Hegna, "Marginal stability boundaries for infinite-n ballooning modes in a quasiaxisymmetric stellarator", Phys. Plasmas **10**, 4716–4727 (2003).

[11]B. Faber, M. Pueschel, P. Terry, C. Hegna, and J. Roman, "Stellarator microinstabilities and turbulence at low magnetic shear", J. Plasma Phys. **84**, 10.1017/s0022377818001022 (2018).

[12]J. Greene and M. Chance, "The second region of stability against ballooning modes", Nuclear Fusion **21**, 453–464 (1981).

[13]M. Willensdorfer et al., "Field-Line Localized Destabilization of Ballooning Modes in Three-Dimensional Tokamaks", Phys. Rev. Lett. **119**, 10.1103/PhysRevLett.119.085002 (2017).

[14]N. Leuthold et al., *On the relation between magnetic perturbations induced toroidal asymmetries and the pump-out effect in ASDEX Upgrade*, tech. rep. (2018), pp. 497–500.

[15]M Willensdorfer et al., "Dynamics of ideal modes and subsequent ELM crashes in 3d tokamak geometry from external magnetic perturbations", Plasma Physics and Controlled Fusion **61**, 014019 (2018).

[16]T. Weyens, R. Sánchez, G. Huijsmans, A. Loarte, and L. García, "PB3D: A new code for edge 3-D ideal linear peeling-ballooning stability", J. Comput. Phys. **330**, 997–1009 (2017).

[17]H. R. Wilson, J. W. Connor, A. R. Field, S. J. Fielding, R. L. Miller, L. L. Lao, J. R. Ferron, and A. D. Turnbull, "Ideal magnetohydrodynamic stability of the tokamak high-confinement-mode edge region", Phys. Plasmas **6**, 1925–1934 (1999).

[18]A. Mikhailovskii, G. Huysmans, W. Kerner, and S. Sharapov, "Optimization of computational mhd normal-mode analysis for tokamaks", Plasma Physics Reports **23**, 844–857 (1999).

[19]C. Ham, I. Chapman, A. Kirk, and S. Sarrelma, "Modelling of three dimensional equilibrium and stability of mast plasmas with magnetic perturbations using vmec and cobra", Physics of Plasmas **21**, 102501 (2014).

[20]I. Chapman et al., "Three-dimensional distortions of the tokamak plasma boundary: boundary displacements in the presence of saturated MHD instabilities", Nuclear Fusion **54**, 083007 (2014).

[21]M. Anastopoulos-Tzanis, B. Dudson, C. Ham, C. Hegna, P. Snyder, and H. Wilson, "Non-axisymmetric equilibrium and stability using the ELITE stability code", Nuclear Fusion **59**, 126028 (2019).

[22]N. M. Ferraro, S. C. Jardin, and P. B. Snyder, "Ideal and resistive edge stability calculations with m3d-c1", Physics of Plasmas **17**, 102508 (2010).

[23]G. Q. Li, X. Q. Xu, P. B. Snyder, A. D. Turnbull, T. Y. Xia, C. H. Ma, and P. W. Xi, "Linear calculations of edge current driven kink modes with bout++ code", Physics of Plasmas **21**, 102511 (2014).

[24]C. Nührenberg, "Compressional ideal magnetohydrodynamics: unstable global modes, stable spectra, and alfvén eigenmodes in wendelstein 7–x-type equilibria", Physics of Plasmas **6**, 137–147 (1999).

[25]T. S. Hahm, "Nonlinear gyrokinetic equations for tokamak microturbulence", The Physics of Fluids **31**, 2670–2673 (1988).

[26]F. Jenko, W. Dorland, M. Kotschenreuther, and B. N. Rogers, "Electron temperature gradient driven turbulence", Physics of Plasmas **7**, 1904–1910 (2000).

[27]G. R. McKee et al., "Increase of turbulence and transport with resonant magnetic perturbations in ELM-suppressed plasmas on DIII-D", Nucl. Fusion **53**, 113011 (2013).